Analysing Battolyser Electrodes in Operation with X-ray and Neutron Powder Diffraction

MASTER THESIS SUSTAINABLE ENERGY TECHNOLOGY

Paul Bruinen

Analysing Battolyser Electrodes in Operation with X-ray and Neutron Powder Diffraction

Master Thesis Sustainable Energy Technology

By

Paul Bruinen

in partial fulfilment of the requirements for the degree of

Master of Science
in Sustainable Energy Technology

at the Delft University of Technology,
to be defended publicly on Wednesday August 29, 2018 at 10:30 AM.

Supervisor:	Prof. dr. F.M. Mulder	
Thesis committee:	Prof. dr. F.M. Mulder,	MECS, TU Delft
	Dr. ir. L. v. Eijck,	RST, TU Delft
	Dr. ir. M. Wagemaker,	RST, TU Delft

ABSTRACT

The battolyser concept is based on an old fashioned nickel iron battery, consisting of a positive nickel(oxy) hydroxide electrode and negative iron (hydroxide) electrode. Research has been performed on the structural changes of the nickel and iron electrode upon charge and discharge. A lot of research can be found for the nickel electrode, but crystal structure studies are few. Much less research is performed on the iron electrode. Therefore the structural changes of the nickel(oxy) hydroxide and iron (hydroxide) electrodes during operation are further researched. $Ni(OH)_2$ exists in the form of an α- or β-modification and NiOOH in a β- or γ-modification. The structure of the nickel(oxy)hydroxide phases has layers of edge-sharing NiO_2 octahedra, where in between guest atoms can situate. Conventional nickel electrodes operate mainly between β-$Ni(OH)_2$ and β-NiOOH, so most research focussed on this area. Upon overcharge the γ-NiOOH is formed and when discharging a direct reduction of β-NiOOH and γ-NiOOH into β-$Ni(OH)_2$ occurs. The research on the nickel electrode published in this thesis is compared with a previous discharge study performed by Morishita et al. In their Rietveld refinement of the β-phases an ideal and fault phase model are assumed and the weight fraction of all phases present in the samples at 0, 50, 100 and 150% of state of charge (SOC) are determined. For the iron electrode four phases can be distinguished. The pure Fe in the electrode upon discharge becomes $Fe(OH)_2$, under deep discharge this transforms even further towards FeOOH. For the deactivation process the reaction moves towards magnetite (Fe_3O_4). First the battery electrodes from the shelf are analysed by SEM-edx , X-ray diffraction and neutron diffraction. Then neutron powder and X-ray diffraction analysis have been performed to study the structural changes of the electrodes during charge and discharge. The nickel electrodes are measured at various states of charge from 0 to 100% and iron electrodes 0 to 90%. Preliminary experiments for the in-situ neutron diffraction test setup are performed. Different thicknesses of quartz glass, several sizes of nickel foam current collectors are tested for the amount of their background noise. In the nickel electrode are next to the carbon, 3 phases present. In the comparison with Morishita et al. significant differences are found. The transition towards β-NiOOH and subsequently γ-NiOOH occurs faster. Already at 50% of SOC the weight fraction of β-NiOOH is 58 $_{wt}$% and at 100% of SOC the γ-NiOOH is 57 $_{wt}$%. The c-parameter of γ-NiOOH is in agreement with Morishita et al. with a lattice distance of 20.8 Å. Morishita et al. did not specify how they determined the state of charge, so maybe they calculated the SOC in a different way. In the iron electrode three phases are identified, namely iron (Fe), goethite (FeOOH) and magnetite (Fe_3O_4). This is a strange result, because where $Fe(OH)_2$ is expected, FeOOH is found. Probably discharged too far, moving the reaction into the second discharge plateau. The weight fraction of Fe increases and FeOOH decreases with increasing state of charge. The hydrogen content is decreasing with increasing SOC proportional to the background function for both the nickel and iron electrode.

ACKNOWLEDGEMENTS

First I would like to thank my weekly and daily supervisors Fokko Mulder and Bernhard Weninger for their patience and good feedback. I would like to thank Lambert van Eijck and Kees Goubitz for their consistent help on the neutron diffraction experiments. For the practical questions Joost Middelkoop and Herman Schreuders were always available. I also would like to acknowledge Ben Norder en Duco Bosma for their guidance on the X-ray diffraction and SEM measurements. At last a thank you to my girlfriend Ilse Koopmans for her continued support.

CONTENTS

1 INTRODUCTION

The United Nations Climate Change Conference held in Paris 2015 set up an agreement with the aim to limit global warming well below 2°C. To achieve this goal more renewable energy needs to be implemented. The fluctuating nature of the renewable energy supply and the electricity demand, results in a mismatch of electricity and asks for a method to match supply and demand. Nowadays the mismatch from supply and demand is levelled out by turning on or off fossil fuel plants and when necessary turn off wind or solar energy. In the ideal case you want to be able to store the excess energy produced by renewables and supply the energy when the demand is larger than the energy produced. [1]

The battery/electrolyser concept devised by F.M. Mulder, also called a battolyser, can be a solution to the energy storage problem.[1] The concept is based on an old fashioned nickel iron battery integrated in an alkaline electrolyser. The biggest limitation of the nickel-iron battery used to be its hydrogen evolution. This disadvantage can be used in its advantage by utilizing the hydrogen evolution. The hydrogen gas produced can be extracted from the electrolyte and stored separately. Later on this hydrogen gas can be used to run a fuel cell or turned into other valuable products, such as ammonia, via the Haber-Bosch process. In this way, the battery and electrolysis concept are combined in one single device. On the short term/daily energy is stored chemically with the battery function and for the long term/seasonal the hydrogen production is utilised with the electrolyser functionality. In Figure 1 a schematic illustration of the battolyser concept can be found. Consisting of a positive Ni electrode and negative Fe electrode submerged in electrolyte, an ion conducting membrane and O_2 / H_2 retrievers.

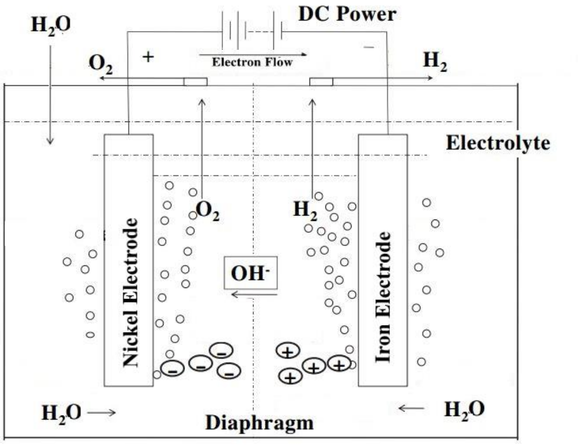

Figure 1. Schematic illustration of the battolyser concept

The structure of the nickel electrode and the iron electrode are changing upon charge and discharge. A lot of research has been done on the nickel electrode, but crystal structure studies are few. Much less research is performed on the iron electrode. Next to that, is the battolyser operating in a different region then the battery, it would be interesting to further investigate the deep discharge and overcharge region.

The composition of phases, morphology of the material and crystallinity of the structure influence the behaviour of the nickel and iron electrodes in operation significantly. Volumetric and structural changes have effect on the porosity, electrical and ionic conductivity and mechanical strength of the electrodes. A better understanding of the structural changes of the electrodes is necessary to predict the behaviour of the material upon charge and discharge and utilize the material to its fullest potential. [2]

That's why the main research question becomes:

- How does the structure of the nickel(oxy) hydroxide and iron (hydroxide) electrodes change during operation?

For the battolyser several operations can be distinguished, namely charge, overcharge, discharge and deep discharge. In this research the focus is on the charge mode and thus the sub questions can be formulated:

- Which materials are used in the industrially manufactured batteries?
- What are the fractions of the compounds in the electrodes?

- How does the structure of both electrodes change during charge?
- How do the material properties change during charge?
- Which method can be developed to investigate the nickel and iron electrodes?
- How to perform Rietveld refinement on the XRD and ND analysis?
- Can neutron diffraction be used to observe the H in the different compounds?

Literature research is performed to get a deeper understanding of the Ni-Fe battery. The experiments are performed with a neutron diffractometer, so a better understanding of neutron diffraction is required as well. The literature questions are:

- What is the working principle of the Ni-Fe battery?
- What is known about the structure change of the nickel(oxy)hydroxide and iron (hydroxide) electrodes?
- How do X-ray and neutron diffraction work?

To give an answer to the research questions first a literature study is performed. After the theory, the experiment specifics are outlined. In the third chapter the results of neutron diffraction experiments are shown. In the discussion, the relevance of the results in relation to literature and the research question is discussed. Finally, in the conclusion the research questions are answered and follow up research recommendations are given.

2 THEORY AND EXPERIMENTAL

In this chapter are firstly the working principles of the Ni-Fe battery explained, then a short course on electrolysis and a section on the different types of membranes. In the third part, cyclic voltammetry is studied and finally the experimental setup is presented.

2.1 NICKEL-IRON BATTERY

The battery was developed in 1901 by Jüngner in Sweden and Edison in the US. It consists of a nickel oxyhydroxide as a positive electrode and iron as a negative electrode. The first industrial applications for the battery was as a traction battery in forklift trucks and mine/railway locomotives. The interest decreased in the 1960s, while in 1975 there was a short revival of the battery in electric vehicle applications. The battery had quite some advantages but the limitations prevented it from completely breaking through. The advantages and limitations are outlined here below and are subsequently discussed in more detail.

Advantages
- Electrically and mechanically robust, withstands deep discharge and overcharge
- Long cycle and calendar life
- Good specific energy (double of a lead acid battery)
- No negative temperature effects on specific energy or cycle life
- Simple maintenance
- Simple manufacturing
- Abundant materials
- Low cost
- Environmentally safe
- Recyclable

Limitations
- Energy efficiency 50%
- Hydrogen boil off
- Heavy weight

A big advantage is that the negative electrode is made from iron, which is relatively abundant compared to other electrode materials such as cadmium, lead and zinc. For such an abundant material it has a good specific energy, with more than 1.5-2 times the energy density of lead-acid batteries. Besides that, iron electrodes are electrically and mechanically robust. They can withstand mechanical shock and vibration, short-circuiting, over(dis)charge and have no memory effect. Therefore nickel-iron batteries are well known for their long cycle life even when abused. [3] The battery is easy to maintain, needs topping up of electrolyte by water addition or replacement of the electrolyte. The limitation of the battery is a low energy efficiency of around 50%, here it is outperformed by other battery types. The main reason of the low efficiency is its high self-discharge. This is because hydrogen evolution does not only occur when the battery is charging, but also when it's not in use. Sluggish discharge behaviour is one of the main disadvantages of Ni-Fe batteries. The battery kinetics are temperature dependant. Hence, poor performance at temperatures below zero degrees, because of the low conductivity of the electrolyte, the passivation of the iron electrode and a low solubility of iron ions. This low solubility is mentioned in relation to a solution precipitation process when charging and discharging. The battery has a good performance at ambient temperatures. [4]

The positive electrode of the battery consists of nickel oxyhydroxide (NiOOH) and the negative electode of iron, when the battery is charged. The battery has the following charge-discharge reaction.

$$2NiOOH + Fe + 2H_2O \leftrightarrow 2Ni(OH)_2 + Fe(OH)_2$$
$$E_{cell} = 1{,}37\ V$$

When discharging the reaction moves to the right and for charging the reaction moves to the left. Under deep-discharge a second discharge reaction follows at a lower potential.

$$NiOOH + Fe(OH)_2 \leftrightarrow Ni(OH)_2 + FeOOH$$
$$E_{cell} = 1{,}05\ V \text{ vs SHE}$$

2.2 NICKEL STRUCTURE

2.2.1 PHASE TRANSFORMATIONS

There are four types of modifications of nickel electrode, see Figure 2. $Ni(OH)_2$ exists in the form of an α- and β-modification and NiOOH in a β- or γ-modification. β-$Ni(OH)_2$ is preferred as active material, because it has a high stability in strong alkaline electrolytes. This phase shows a good reversibility upon charge towards β-NiOOH. Both NiOOH and $Ni(OH)_2$ are build up out of layers of edge-sharing NiO_2 octahedra. In between those layers, called galleries, guest atoms can situate. For both the β-phases the galleries contain only protons and no water. In the α-$Ni(OH)_2$ and γ-NiOOH water and other particles from the electrolyte can be found.[5] The nickel electrode of a battery has relatively fast kinetics and good cycling behavior. This is related to its (dis)charge mechanism, which is a solid-state insertion reaction from NiOOH to $Ni(OH)_2$ upon discharge. The reaction moves to the left when charging.

$$NiOOH + H_2O + e^- \leftrightarrow Ni(OH)_2 + OH^-$$
$$E^o = -0{,}49\ V\ vs\ SHE$$

On charge the Ni electrode is oxidized and reduced upon discharge. The reversible electrode potential can be calculated with the help of the Nernst equation. [3]

$$E_{rev} = 0{,}49 - 0{,}059\log\left(\frac{a[Ni(OH)_2]a[OH^-]}{a[NiOOH]a[H_2O]}\right)$$

For batteries overcharging is prevented, but the battolyser also operates in this overcharge regime. When overcharging the electrode γ-NiOOH is formed and it is also formed under high charge rates. Upon discharge, γ-NiOOH can transform directly into β-$Ni(OH)_2$ or α-$Ni(OH)_2$ depending on the material properties (such as distribution, percentage, conductive additives and nature of the binder). α-$Ni(OH)_2$ is not stable and moves over time to the stable β-$Ni(OH)_2$. Initially the electrode is prepared with α-$Ni(OH)_2$, but due to instability this transforms to β-$Ni(OH)_2$.

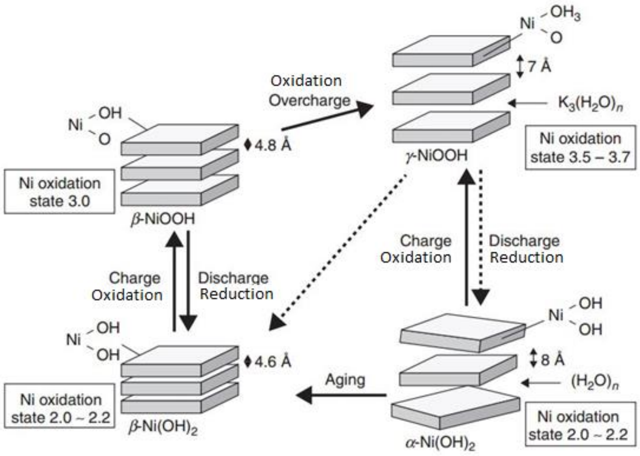

Figure 2. Bode diagram of the nickel(oxy)hydroxide phases [3]

Conventional nickel electrodes operate mainly between β-$Ni(OH)_2$ and β-NiOOH. The γ-NiOOH phase is unwanted in conventional batteries, due to the large volume expansion and drying of the electrolyte under the overcharge conditions when it is produced. As a consequence, the entire battery can be damaged in a conventional battery upon volume expansion.[6] Next to that, a study has been performed on nickel–cadmium and nickel–hydrogen batteries where the formation of γ-NiOOH is accountable for the memory effect. The memory effect is a reduction in capacity, to a fixed cut off voltage, due to highly repetitive cycles. [7] The formation of γ-NiOOH can be suppressed by additives. Simultaneous cadmium and cobalt addition are most effective for suppressing the γ phase. Partially substituting the nickel for zinc is another method with similar effects. Zinc has a larger ionic radius than nickel, resulting in a distortion in the crystal lattice.[3]

2.2.2 MEMORY EFFECT, SECOND LOW VOLTAGE PLATEAU AND STABILIZING ALPHA-NI(OH)$_2$

In batteries which use a positive nickel electrode the memory effect is observed (Figure 3). It occurs after the electrode is repeatedly partially discharged and subsequently fully charged or overcharged. There is not yet a definitive explanation about the working principle of this phenomenon. The most reasonable is that these cycles place the battery in an overcharged state, resulting in the formation of γ-NiOOH. The γ-NiOOH can degrade cell performance and thereby causes the memory effect. The lattice volume increases with around 30% with the transformation from β-NiOOH towards γ-NiOOH. The rapid expansion leads to microcracks in the active material, which lowers the electrode conductivity. It is also causing the dry-out of the separator, by extracting the electrolyte towards the electrode. In this way, the lower capacity and the high discharge rate can be explained with the formation of γ-NiOOH. The battery can be regenerated by repeated deep discharges and recharges.

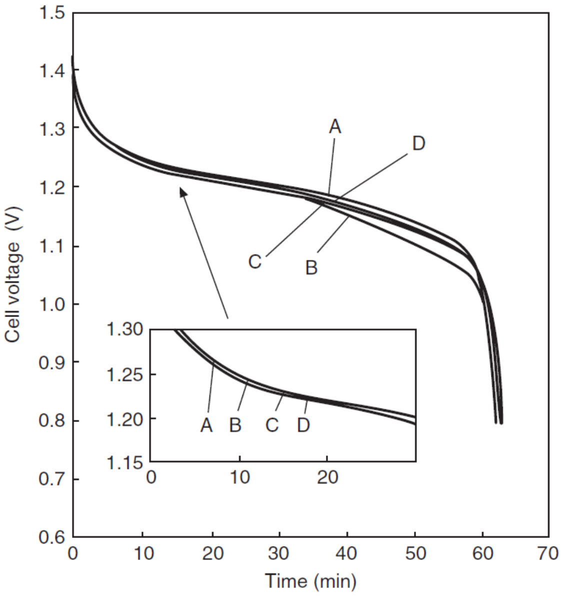

Figure 3. Discharge curve of AAA Ni-Cd battery at 250 mA, 30°C . A) normal-state cell; B) first discharge curve after 50 swallow discharge and full charge cycles; C) second discharge curve; D) third discharge curve[7]

The second low voltage plateau, not to be confused with the memory effect, is sometimes observed in nickel electrodes. A typical discharge curve is shown in Figure 4. The first plateau can be ascribed to the reduction of β-NiOOH to β-Ni(OH)$_2$. The second plateau is usually 0.03-0.4 lower than the first plateau and is ascribed to the presence of graphite. The K$^+$ ions coincide with nickel-oxyhydroxide, but during discharge K$^+$ ions intercalate into the neighboring graphite, this lowers the potential of the electrode. When there is no graphite in the electrode the presence or absence of the second plateau is not understood and more research is needed to clarify this phenomena.[8]

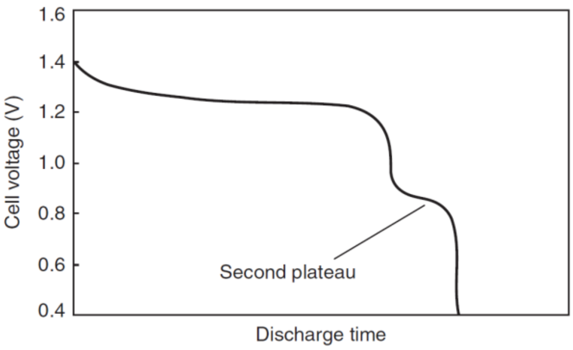

Figure 4. Typical example of a second low-voltage plateau [8]

Recent efforts in stabilizing α-$Ni(OH)_2$ are made. The transformation between α-$Ni(OH)_2$ to γ-NiOOH occurs without mechanical deformation and has a higher storage capacity than with the β-NiOOH/β-$Ni(OH)_2$ couple can be achieved. This is very attractive for storage purposes, but α-$Ni(OH)_2$ is unstable and falls back to β-$Ni(OH)_2$. Therefore research is performed to stabilize the α-$Ni(OH)_2$. Partial substitution of nickel by cobalt, zinc aluminium or iron manganese and the addition of organic materials have been investigated. In march 2018 a paper is pubished which successfully combines cobalt and ethylene glycol as neutral stabilizer. [9] The Polyethylene glycol is placed into the interlayer spacing to build a network structure and by doping the nickel hydroxide with cobalt the electrostatic attraction between layers is increased. The electrode has a good specific capacity of 334 mAh/g and is stable for 20 days.

2.2.3 ADDITIVES

The effect of cations on the performance of the electrode has been tested, such as cobalt, lithium, cadmium, zinc, arsenic and bismuth. To enhance cycle life caesium hydroxide and rubidium oxide can be added. In Table 1 varied tested additives for nickel electrodes are summarized. The most used additive is cobalt hydroxide as a spacing agent. Unfortunately cobalt is scarce and very expensive. So a method is to combine it with Zn and loose some in electrode utilization, but make a very stable triprecipitate of Ni-Co-Zn. A common composition is 94 wt% Ni, 3 wt% Co and 3 wt% Zn. Calcium additives in the form of calcium hydroxide, calcium fluoride, calcium sulfide, calcium oxide suppress oxygen evolution at 65°C upon charge (yttrium oxide can also be used). But they can cause a loss in power and cycle life. Cobalt additives are also used to for storage purposes to prevent cracking-up of the conductive network and losing the conductivity. To increase conductivity, especially for high power applications, metallic nickel fibers are added. The commercially mostly used additive for conductivity purposes is carbon.[10]

Table 1 additives for nickel electrode [10]

Effect of additives	Co	Cd	Zn	Li	As	Bi	$Cs(OH)_2$	$Rb(OH)_2$
Inhibit self-discharge (H)	x				x			
Prevent formation of γ-NiOOH	x	x	x					
Increase overpotential for oxygen evolution	x							
Prevent electrode swelling	x	x	x					
Increase charge acceptance	x	x						
Reduce oxidation potential of $Ni(OH)_2$	x							
Reduce reduction potential of $Ni(OH)_2$	x							
Increase overpotential for oxygen evolution	x	x	x	x				
Increase active material utilization	x							
Enhance cycle life	x						x	x
Eliminate poisoning effect of Fe (leached from substrate)				x				
Stabilize α-$Ni(OH)_2$ structure						x		

2.2.4 PREVIOUS PHASE TRANSFORMATION X-RAY AND NEUTRON DIFFRACTION STUDIES

Morishita et al. [11] performed a study on the phase transformations of the nickel hydroxide electrode in the charge-discharge process by XAFS and XRD. A Rietveld refinement is performed on the samples analysed by XRD at 0, 50, 100 and 150% of state of charge (SOC). Two structural models are distinguished for the β-$Ni(OH)_2$ and β-NiOOH phase, namely an ideal and fault phase model are assumed. (see Figure 5). The ideal phase model has an ideal oxygen packing sequence, whereas the oxygen packing sequence of the fault phase model is disturbed. Ideally the structure of the nickel hydroxide grows slab by slab. The oxygen packing is then ABABAB along the c direction. For the fault phase model two stacking faults in the oxygen packings can be distinguished, namely the (1) growth fault and (2) deformation fault. (1) In the growth fault the structure grows continuously with its natural packing rule and (2) in the deformation fault the structure is displaced in part. Below are the stacking faults underlined within the oxygen packing sequence along the c direction.

1. growth fault
   ABAB$\underline{\text{C}}$BCB … CBCB$\underline{\text{A}}$BAB
2. deformation fault

ABAB$\underline{C}$ACA … CACA$\underline{B}$CBC … BC$\underline{A}$BAB

These stacking faults can explain the line broadening in the XRD spectra, the electrochemical behaviour and the unexpected bands in the Raman spectra. [12]

The weight fraction of all phases present in the samples at 0, 50, 100 and 150% of SOC are determined (Table 2). The space group and lattice parameters can likewise be found in the table. The lattice parameters for the β-$Ni(OH)_2$ don't change with increasing SOC, but for the β-NiOOH a slight variation is visible. At 0% of SOC only β-$Ni(OH)_2$ is observed, with 76.5$_{wt}$% ideal and 23.5$_{wt}$% fault phase. At 50% of SOC the β-$Ni(OH)_2$ is for 40.7$_{wt}$% transformed into β-NiOOH. This is 95.8$_{wt}$% at the sample with 100% of SOC. At 150% of SOC the transformation of β-NiOOH toward γ-NiOOH is observed with a weight fraction of 18.4$_{wt}$%. Next to that, in the interlayer an increase of potassium ions and H_2O (OH^-) is noticed.

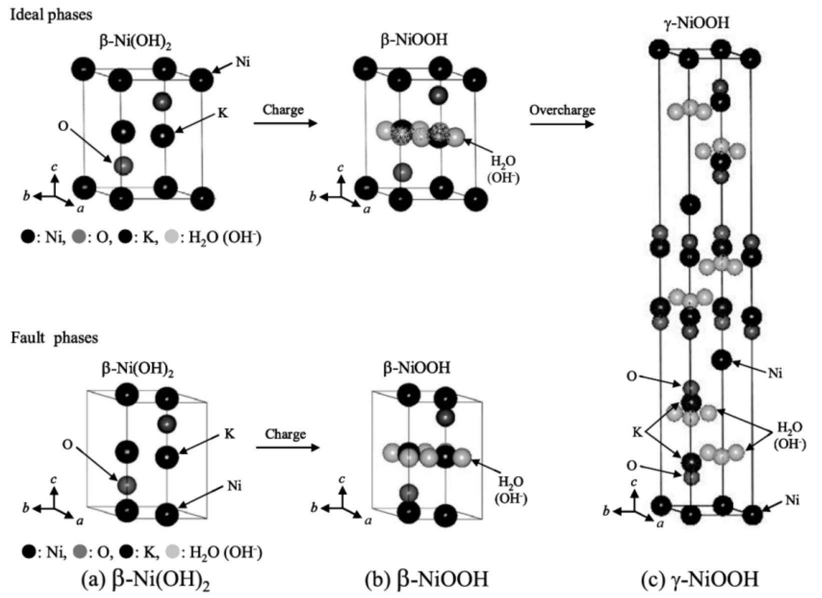

(a) β-$Ni(OH)_2$ (b) β-NiOOH (c) γ-NiOOH

Figure 5. Structure models of ideal and fault phases of β-Ni(OH)2 (a), β-NiOOH (b) and γ-NiOOH (c). [9]

Table 2. Phase properties of the Ni samples at 0, 50, 100 and 150% of SOC [9]

Phase	Spacegroup	Structure model	Unit cell parameters, a; b; c (Å)	Weight fraction ($_{wt}$%)
0% of SOC				
β-$Ni(OH)_2$	P-3m1 (164)	Ideal	3.147; b=a; 4.676	76.5
		Fault	3.150; b=a; 4.679	23.5
50% of SOC				
β-$Ni(OH)_2$	P-3m1 (164)	Ideal	3.147; b=a; 4.676	43.8
		Fault	3.150; b=a; 4.679	15.5
β-NiOOH	P-3m1 (164)	Ideal	2.927; b=a; 4.723	31.1
		Fault	2.895; b=a; 4.734	9.6
100% of SOC				
β-$Ni(OH)_2$	P-3m1 (164)	Ideal	3.147; b=a; 4.676	3.4
		Fault	3.150; b=a; 4.679	0.9
β-NiOOH	P-3m1 (164)	Ideal	2.925; b=a; 4.712	79.1
		Fault	2.906; b=a; 4.715	16.7
150% of SOC				
β-NiOOH	P-3m1 (164)	Ideal	2.907; b=a; 4.714	61.2
		Fault	2.878; b=a; 4.724	20.4
γ-NiOOH	R-3m (166)	Ideal	2.770; b=a; 20.831	18.4

A previous in situ neutron diffraction study on the nickel hydroxide electrode by Bardé et al. [6] showed a direct reduction of β-NiOOH and γ-NiOOH into β-$Ni(OH)_2$. Protonated and deuterated nickel hydroxide reference samples with different particle size, phase composition and oxidation state were chemically prepared and measured with neutron diffraction. Also, four samples in a specially designed cell (Figure 6) for neutron diffraction were studied upon charge and discharge. In Figure 7 and Figure 8 the results of the in-situ neutron diffraction experiments are shown. A gradual transformation upon discharge of the β-NiOOH into β-$Ni(OH)_2$ is seen in figure 7. In figure 8 a gradual transition upon discharge of γ-NiOOH into β-$Ni(OH)_2$ shows and no inconsistency in the shift. In both figures also Ni peaks show up for the current collectors and the asterix indicates a peak due to the electrolyte and cell. The second plateau phenomena, a partial transfer of 1.2 V to 0.8 V vs Hg/HgO during electrochemical reduction, is not found and is probably related to its surface properties.

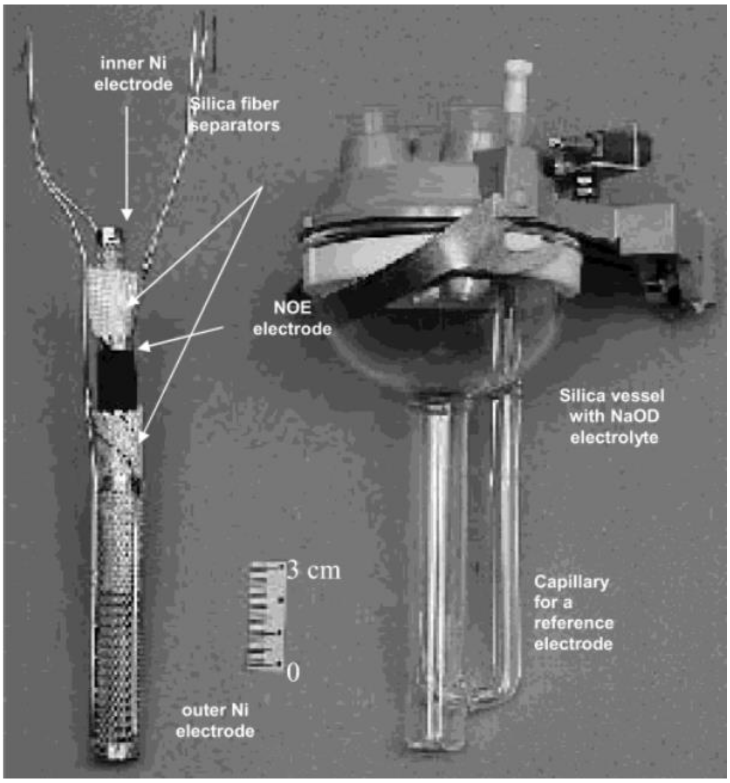

Figure 6. In situ neutron diffraction test cell

Accidental or intentional iron incorporation in the $Ni(OH)_2$/NiOOH electrode plays a critical role in improving the activity, but its not yet understood how. Cyclic voltammetry is performed on electrodes free of Fe versus electrodes with Fe impurities. The potential for the oxygen evolution reaction decreases significantly about 0.15 V when Fe impurities are added. In-situ conductivity measurements show an increase of 30 times the film conductivity with Fe incorporation, but this is not sufficient to explain the change in activity.[13]

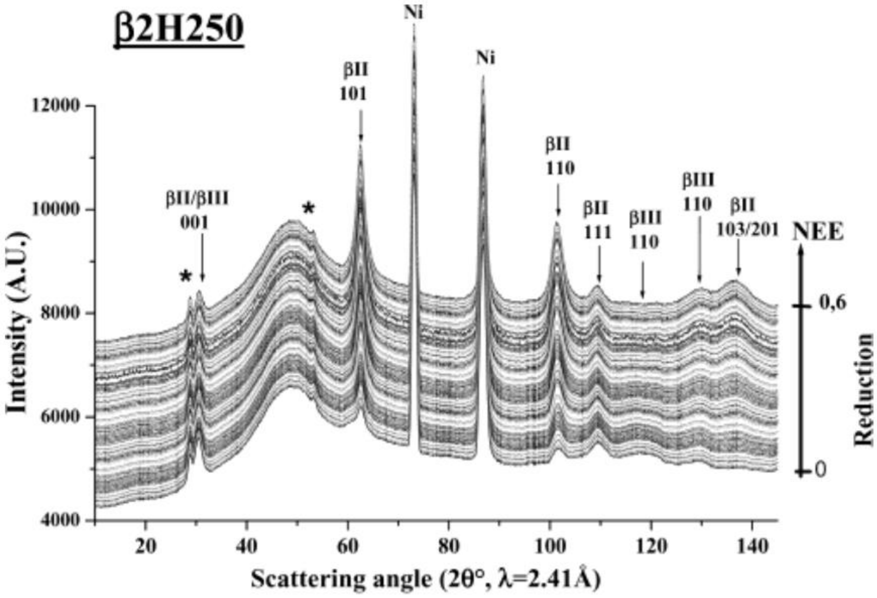

*Figure 7. In-situ neutron diffraction results of the reduction of β-NiOOH (βIII) into β-Ni(OH)₂ (βII) (Ni = nickel current collector, * = peak from electrolyte and cell).* [6]

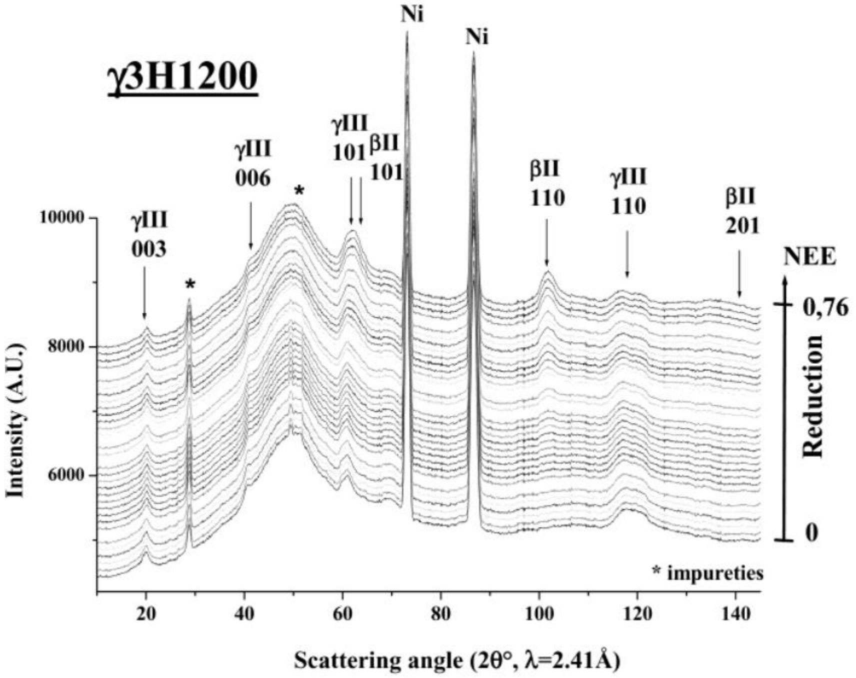

*Figure 8. In-situ neutron diffraction results of the reduction of γ-NiOOH (γ III) into β-Ni(OH)₂ (βII) (Ni = nickel current collector, * = peak from electrolyte and cell).* [6]

2.3 IRON STRUCTURE

(dis)charge reaction mechanisms

The discharge reaction mechanisms of the iron electrode in an alkaline solution develops in two steps. On the first plateau iron reacts upon discharge to become iron hydroxide.

$$Fe + 2OH^- \leftrightarrow Fe(OH)_2 + 2e^-$$
$$E^o = -0{,}88\ V\ vs\ SHE$$

For the second discharge plateau (deep discharge) a debate is still going on. As product feroxyhyte (δ-FeOOH), magnetite (Fe_3O_4) and hematite (α-Fe_2O_3) are considered. In the reversible reactions 1 and 2 the iron hydroxide is converted to iron oxide-hydroxide or magnetite subsequently. Reaction 3 is the further conversion of magnetite into hematite. Reaction 1 involves a sustaining proton flow through the electrode in order to change the compostion from $Fe(OH)_2$ to δ-FeOOH. The composition change develops through the whole material, so the mechanism is homogeneous in nature. [3], [14]

$$Fe(OH)_2 + OH^- \leftrightarrow FeOOH + H_2O + e^-$$
$$E^o = -0{,}56\ V\ vs\ SHE \qquad (1)$$

$$Fe(OH)_2 + 2OH^- \leftrightarrow Fe_3O_4 \cdot 4H_2O + 2e^-$$
$$E^o = -0{,}67\ V\ vs\ SHE \qquad (2)$$

$$2Fe_3O_4 + 2OH^- \rightarrow 3Fe_2O_3 + H_2O + 2e^-$$
$$E^o = -0{,}61\ V\ vs\ SHE \qquad (3)$$

In Figure 9 a typical discharge/charge curve of the iron electrode is depicted. The several plateaus (step 1 and step 2) are indicated and corresponding reactions are displayed. In this electrode reaction 2 is found for the second discharge plateau (Step 2). The crystal structures of the iron phases (Table 3) are useful to give insight into the structural changes of the electrode during operation. [2]

Table 3. crystal structure data on several iron phases [2]

phase	structure
α-Fe	BCC
Fe_3O_4 (magnetite)	Inverse spinel
α-FeOOH (goethite)	HCP
β-FeOOH	BCC
γ-FeOOH (lepidocrocite)	CCP
δ-FeOOH	HCP
$Fe(OH)_2$	HCP

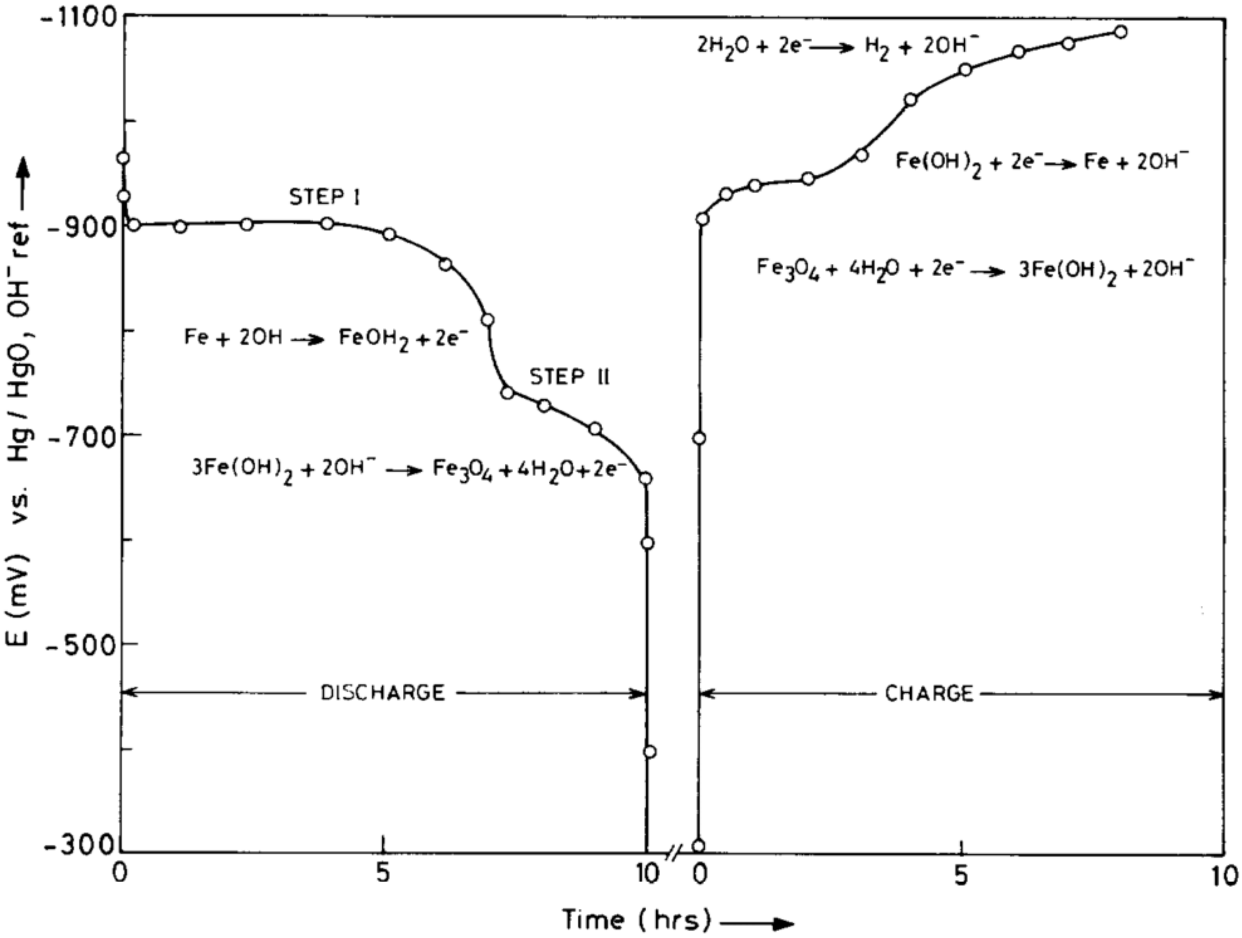

Figure 9. Typical discharge/charge curve of iron electrode in 6 M KOH with an indication of the reaction mechanisms at the voltage plateaus. [2]

First discharge plateau

In normal batteries the second plateau is not being used, due to a less negative potential. The first plateau is mainly used and the reaction is highly reversible.[15] Several voltammetry and X-ray diffraction studies have been performed on this first plateau. It can be divided in two steps via a soluble intermediate ferrite $HFeO_2^-$.

$$Fe + 3OH^- \leftrightarrow HFeO_2^- + H_2O + e^-$$
$$E^o = -0{,}75\,V\ vs\ SHE$$

This soluble ferrite intermediate than further reacts with H_2O to form iron hydroxide. [3]

$$HFeO_2^- + H_2O \leftrightarrow Fe(OH)_2 + OH^-$$
$$E^o = -0{,}88\,V\ vs\ SHE$$

The solubility of the ferrite ion in alkaline medium is very low, it is in the order of 10^{-4} M.[16] The solubility of $HFeO_2^-$ is rate determining and therefore directly influences the rates of crystallization and diffusion. The solubility of the intermediates are very temperature dependent and this is why iron electrodes perform worse at lower temperatures. Higher temperatures will give higher iron ion solubility, resulting in faster kinetics and a higher current density. There is an advantage of operating the battery at elevated temperatures. [17]

Second discharge plateau

Lee et al. [14] published in march 2018 a letter in ACS energy focussing on the second discharge plateau. Through cyclic voltammetry and a combination of SEM and X-ray diffraction and Raman spectroscopy they identified four stages of Fe anode evolution. Each sample was taken out of the cell and rinsed after a predetermined number of cycles and vacuum dried at 80˚C. They identified a development (I), retention (II), fading (III) and failure (IV) stage, see Figure 10.

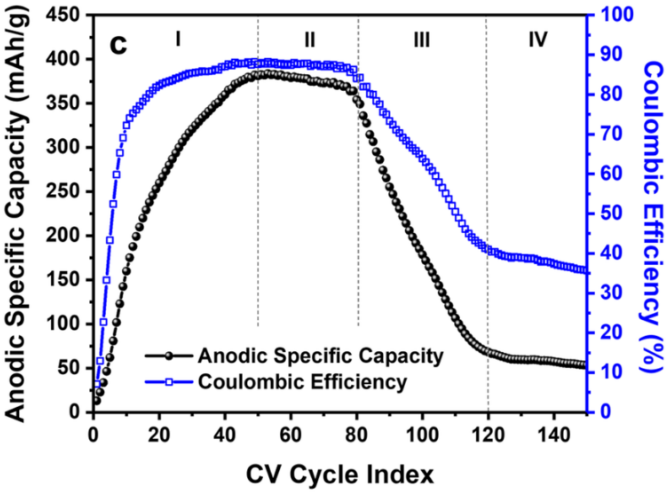

Figure 10. Evolution of specific capacity and coulombic efficiency over the charge-discharge cycles.

In Figure 11 the XRD, SEM and raman results are shown, where from the conclusions are made. In the first stage α-Fe remained dominant and this stage was highly reversible. The surface-limited charge-discharge reaction led to fragmentation of the Fe, with this the surface area grew and resulted in a higher capacity. In the second stage after 50 cycles SEM observations showed octahedral (figure 11b), which can be classified as the Fd-3m space group. Magnetite (Fe_3O_4) and maghemite (γ-Fe_2O_3) have the same crystal structure and spacegroup. They also have nearly identical XRD spectra, an insignificant peak shift and minor additional peaks show the difference. Nearly all studies claimed Fe_3O_4 prematurely. Raman spectroscopy (figure 11d) confirmed that the octahedral structures are γ-Fe_2O_3. As previously discussed the first charge-discharge reaction is based upon a dissolution-precipitation process, namely the dissolution of Fe into $HFeO_2^-$ and subsequent precipitation to $Fe(OH)_2$. $Fe(OH)_2$ is known to dissolve in highly alkaline solutions, so after the dissolution it can precipitate into γ-Fe_2O_3.

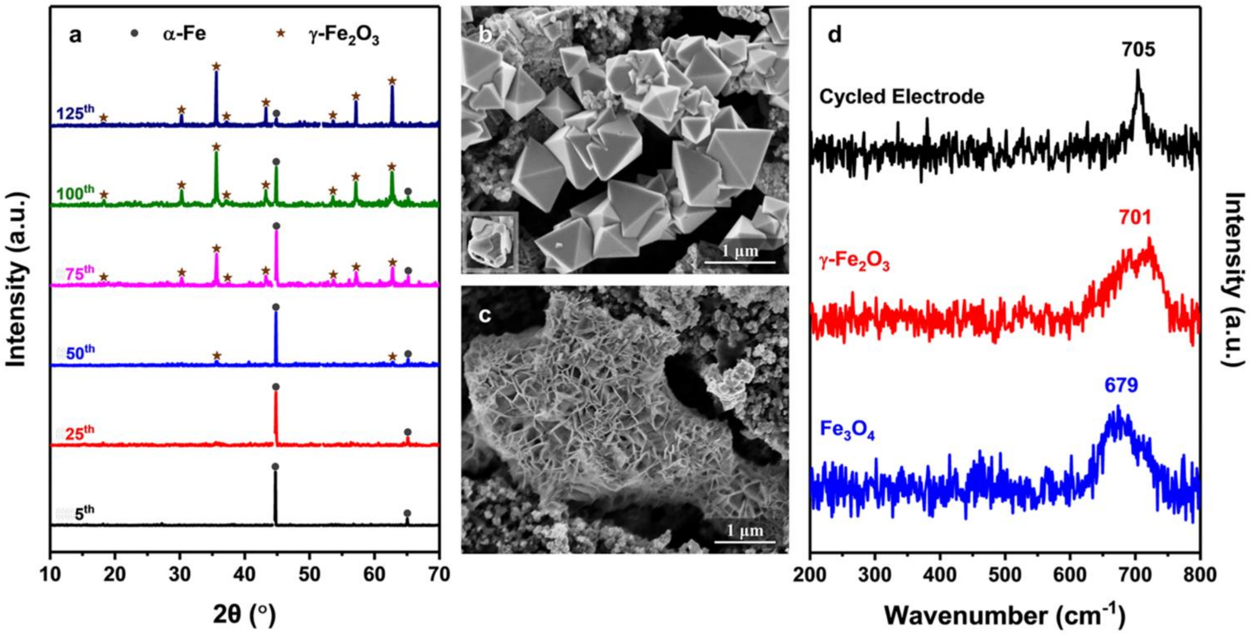

Figure 11. (a) Evolution of XRD spectra when cycling the iron anode. (b) SEM picture of octahedral maghemite and (c) iron fragment found after 75 cycles. (d) raman spectroscopy of electrode after 125 cycles versus magnetite (Fe_3O_4) and maghemite (γ-Fe_2O_3).

From the 80th cycle in stage III abrupt capacity fading takes place in conjunction with the accumulation of γ-Fe_2O_3. γ-Fe_2O_3 particles have a very low capacity under the same conditions. Agglomeration of γ-Fe_2O_3 clogs the surface of the Fe remainders and meanwhile the irreversible reaction of Fe towards γ-Fe_2O_3 will further decrease the Fe fragments.

This process goes on until the entire surface is covered with γ-Fe_2O_3 , this is the failure stage. In this stage only the Fe to $Fe(OH)_2$ reaction remains, the passivation by γ-Fe_2O_3 hinders further the reaction of $Fe(OH)_2$ towards γ-Fe_2O_3.

Activation and self-discharge

When the iron electrode is not used for a while it needs to be activated, this is done by repeated charging and discharging. During activation of the anode the magnetite reacts into iron.[18]

$$Fe_3O_4 + 4H_2O + 8e^- \leftrightarrows 3Fe + 8OH^-$$

For the deactivation process the reaction moves in opposite direction. If iron hydroxide is present in the electrode, than the iron hydroxide is deactivated according to:

$$3Fe(OH)_2 + 2OH^- \leftrightarrows Fe_3O_4 + 4H_2O + 2e^-$$

Nickel-iron batteries are known to suffer from self-discharge when at rest, due to a difference between the iron electrode potential and the hydrogen overpotential in the solution. The potential of the first plateau (E˚ = -0.88 V vs SHE) is lower than the hydrogen overpotential (E˚ = -0.83 V vs SHE) and thus iron is slowly corroding from Fe to $Fe(OH)_2$ in line with:

$$Fe + 2OH^- \leftrightarrow Fe(OH)_2 + 2e^-$$
$$E^o = -0{,}88\, V\ vs\ SHE$$

The counter reaction in the solution due to the hydrogen overpotential will produce hydrogen as followed.

$$2H_2O + 2e^- \rightarrow H_2 + 2OH^-$$
$$E^o = -0{,}83\, Vvs\ SHE$$

Along these lines the iron electrode is thermodynamically unstable at rest and during discharge, resulting in a decrease of charge acceptance. The electrode is losing 1-2% per day of the nominal capacity at 25˚C. During charge the iron electrode is stable, because the electrode potential is higher than the potential for dissolution. [19]

2.4 NEUTRON AND X-RAY DIFFRACTION

Neutron and X-ray diffraction complement each other. Neutrons have a high penetration depth, whereas X-ray is a surface technique. They are both non destructive. X-rays interact with the electrons surrounding the nucleus, whereas neutrons interact with the nucleus of an atom. Therefore neutrons are more sensitive to light elements, such as hydrogen and lithium and can distinguish between isotopes and atoms close to each other in the periodic table. X-rays are more sensitive to heavier elements and can not easily distinguish between two isotopes. Neutrons can also be used to determine magnetic moments and magnetic structures. Neutron diffraction is a strong characterization tool for different battery materials. It can be used to follow in-situ crystallographic transitions. [20]

Neutron and X-ray diffraction are an elastic coherent scattering process. Coherent scattering is a collective motion of neutron waves, also called constructive interference. Incoherent scattering is the random motion of neutron waves, without a collective direction. A scattering process is inelastic when the waves gain or lose energy, diffraction is elastic because there is no energy exchange. In Figure 12the initial and final wave vectors of elastic and inelastic scattering are shown. The scattering vector can be defined by simple geometry (trigonometric functions).

$$q = 2k \sin\theta$$

The wave number k is related to the X-ray and neutron wavelength λ by:

$$k = \frac{2\pi}{\lambda}$$

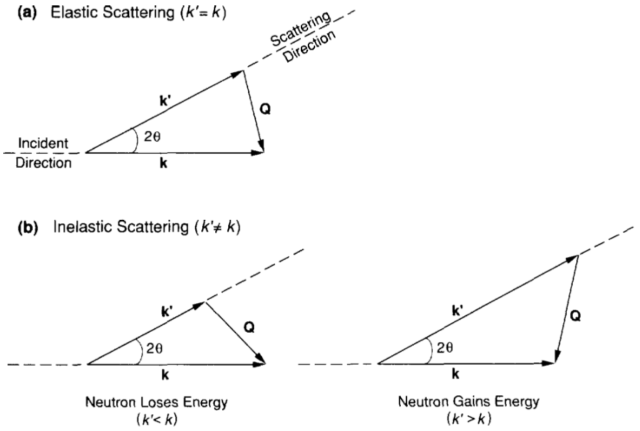

Figure 12. Wave vectors of elastic (a) and inelastic (b) scattering

Diffraction is also known as Bragg scattering, because diffraction takes place when Bragg's law is fulfilled.

$$n\lambda = 2d\ sin\theta$$

Where d is the lattice spacing and θ is the scattering angle. In Figure 13 a schematic of neutron diffraction is depicted, two neutron beams with equal wavelength and phase are scattered by two atoms of a crystal. The lower beam passes over an extra length of 2d sinθ. When this extra length is equal to an integer multiple (n) of the wavelength constructive interference takes place.[21]

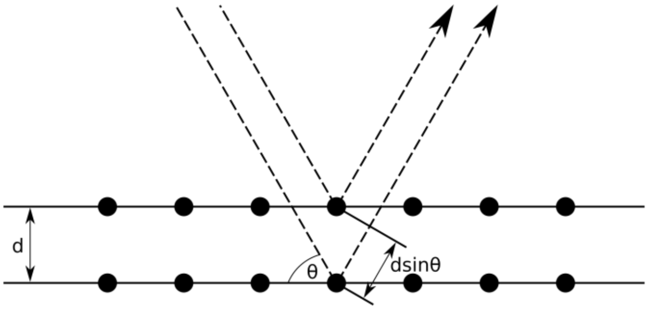

Figure 13. Two neutron beams with equal wavelength and phase are scattered by two atoms of a crystal wherefore Bragg's law is fulfilled. (Bragg diffraction) [21]

This relation can also be expressed with the Laue condition, where the scattering vector q is equal to the reciprocal lattice vector τ.

$$q = \tau$$

2.4.1 X-RAY POWDER DIFFRACTION

X-ray powder diffraction (XRD) is a fast analytical technique mostly used to identify phases of crystalline material and can give information on the lattice parameters. The X-rays are generated in an X-ray tube by heating a filament to get electrons, these electrons are accelerated towards a target when a voltage is applied, bombarding the target material to finally produce the X-rays. This happens when the electrons have enough energy to force out inner shell electrons of the target material, X-ray spectra are produced that are a characteristic of the target material. Then the X-rays are collimated and directed at a sample. The sample diffracts the X-rays and the diffracted rays are collected by the X-ray detector, whereupon the intensity of the diffracted rays and the angle between the incident and diffracted rays is determined. The sample rotates with an angle θ from the collimated beam and detector with 2θ, hereby the intensity of the diffracted X-rays is recorded. When the bragg equation is satisfied a peak in intensity occurs, due to constructive interference. The detected signal is processed and converted into a count rate, which is stored and displayed by the monitor. [22]

Master formula for X-rays

$$\frac{d\sigma}{d\Omega} = {r_0}^2 \sum_j f_{o,i}(\mathrm{q})\, f_{o,j}(\mathrm{q})\mathrm{P}(\Psi)\exp(-iq \cdot (r_i - r_j)$$

f(q) is atomic form factor
f(o) is atomic scattering factor (form factor in forward direction) [23]

In this study is a cobalt source used in the X-ray diffractometer. According to bragg's law are the diffraction peaks at the 2θ positions directly proportional to the wavelength of the incoming x-rays (λ). Cobalt (λ = 1.79 Å) has a longer wavelength than the typically used copper (λ = 1.54 Å) source. The result of the longer x-ray wavelengths are greater 2θ positions, giving more easily observable low angle peaks and better peak separation.[24]

2.4.2 NEUTRON POWDER DIFFRACTION

The master formula of elastic scattering for a system of nuclei is as followed.

$$\frac{d\sigma}{d\Omega} = \left|\sum_j \mathrm{b}_j \exp(i \cdot q r_j)\right|^2 \equiv S(q)$$

With scattering length b_j and nuclear position r_j. It is per definition equal to the structure factor S(q).

For a crystal the scattering cross section can be further specified as:

$$\frac{d\sigma}{d\Omega} = \exp(-2W)\, |F_N(q)|^2 \left|\sum_j \exp(i \cdot q r_j)\right|^2$$

With the Debye-Waller factor as a correction term for atomic vibrations due to temperature.

$$DWF = \exp(-2W) = \exp(-\langle q \cdot u_j \rangle^2)$$

The nuclear structure factor depends on the arrangement of atoms inside the unit cell. [25]

$$F_N(q) = \sum_i \mathrm{b}_i \exp(i \cdot q \Delta_i)$$

In neutron powder diffraction a monochromatic beam of neutrons is diffracted by a sample, the intensity of the diffracted beam is recorded as a function of 2θ (Figure 14). A powder consists of a lot of randomly oriented crystal grains, therefore there are no extinction effects and Bragg scattering takes place for all orientations. As a consequence, scattering cones with opening angles of 4θ become visible. These cones are called the Debye-Scherrer cones. [25]

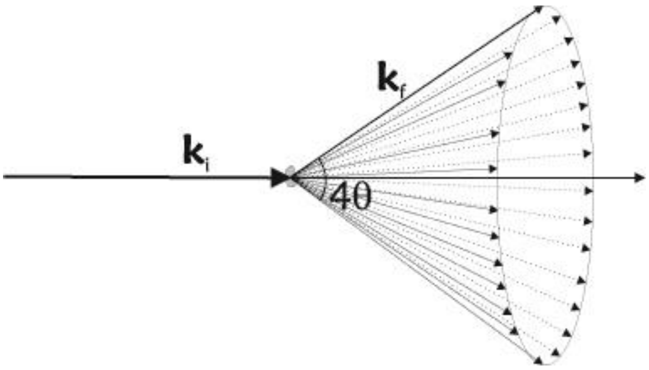

Figure 14. Schematic of a Debye-Scherrer cone

Pearl at TU Delft

Neutron diffraction used to be only available at large scale neutron facilities, which operate very bright neutron sources. In Delft a novel neutron powder diffractometer PEARL was developed, despite the low thermal power of the reactor of 2.3 MW. The layout of the diffractometer PEARL at the TU Delft is displayed in Figure 15. The beam tube is directly viewing at the reactor core, therefore the shielding of fast and epithermal neutrons is important. The background is reduced by a sapphire (Al2O3) single crystal of 1 cm thick. The fast neutrons are reduced by one order of magnitude. A shielding which consists of layers of paraffin, boron rubber, steel, polyethylene and heavy concrete reduces the background even further. The focusing Ge monochromator consists of 24 crystals and is placed at a distance of 7 m from the reactor core. The monochromator reflects and focusses neutrons from the reactor onto the sample. By rotation it can select different reflections and associated wavelengths. The sample has typically a diameter of 6, 8 or 9 mm and a height of 50 mm. Experiments are performed at room temperature in a vacuum vessel. Because of the vessel size the sample environment has a maximum diameter of 800 mm. A multi-pixel one-dimensional LiF-ZnS:Ag scintillator detector registers the diffraction pattern of the sample. The detector measures simultaneously around the sample and therefore gets fast results with low initial intensity.

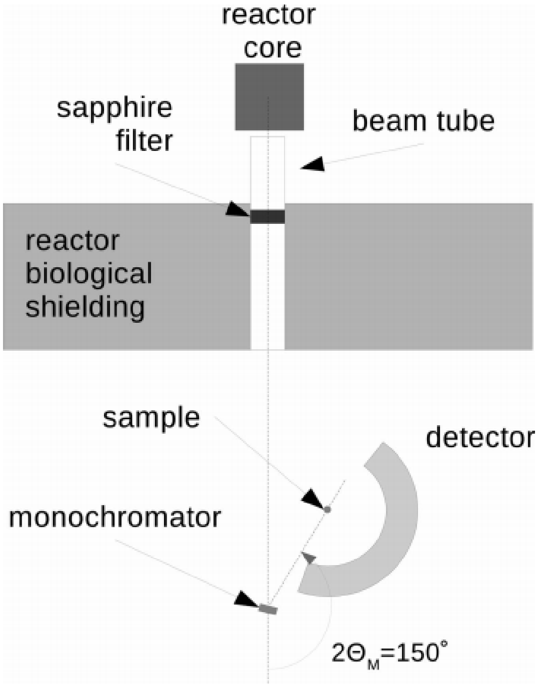

Figure 15. Neutron powder diffractometer PEARL layout

2.4.3 RIETVELD REFINEMENT

The Rietveld refinement model is very suitable for powder diffraction data. A quantitative analysis of mixtures can be performed and the refinement gives accurate and precise unit-cell parameters, even for complex diffraction patterns. Powder diffraction experiments are performed in a fraction of the time needed for single-crystal diffraction studies, which makes it in combination with Rietveld refinement very suitable for heating and phase transformation purposes.[26] To interpret the measured data a model can be fitted to the experiment by a least-square fitting method.[23]

$$I_c = I_0 \left\{ I_b + \sum_{ij} k_i F_{ij}^2 m_{ij} L_{ij} P(\Delta_{ij}) \right\}$$

i = Phase i
j = Reflection j
I = Incident intensity (normalisation = I_0)
k = Scale factor
F = Structure factor (including form factor and DW factor)
m = Reflection multiplicity
Intensity correction factors (geometry, texture, ..)
Peak-shape function depends on instrumental resolution, crystallite size and microstrain

It is important to keep in mind that the Rietveld method is a refinement technique, so the initial computer model needs to be reasonably close to the actual structure of the sample. This can be taken from similar structures, a model might be developed using distance-least-squares, electrostatic energy minimisation or other computer modelling procedures. In some cases a structure model can be assembled from high resolution TEM images.[26]

2.4.4 GSAS-II

GSAS-II is a software package that can be used for all types of crystallographic studies on simple materials or macromolecules, such as data reduction, structure solution and structure refinement. It can be applied to single-crystal and powder diffraction data from X-ray and neutron sources, which includes laboratory and synchrotron sources. Constant wavelength and TOF measurements are both supported and the scattered waves collected on two or one-dimensional detectors can be analysed. GSAS-II has the same functionalities as GSAS/EXPGUI, except for magnetic scattering, but GSAS-II has more functionality in diffraction analysis. GSAS-II can do data reduction, peak analysis, indexing, small-angle scattering fits, Pawley fits and structure solution in addition to structure refinement. It can manage large collections of related datasets in sequential refinements and subsequent parametric fitting. Where the same parameters are applied for the single-crystal structure and Rietveld refinements in GSAS-II and GSAS/EXPGUI identical results are attained, within the limits of standard uncertainties.[27]

2.5 METHOD

A commercial Ni-Fe Battery of the brand Iron Core Power with a nominal voltage of 1.2 V and a nominal capacity of 10 Ah is used. One battery consists of 2 Fe electrodes and 3 Ni electrodes and one electrode is build up out of 6 pockets (Figure 16). The nickel and iron electrodes are both examined the same way. First the electrodes from the shelf are analysed by SEM-EDX , X-ray diffraction and neutron diffraction. The electrode powders are taken out of the battery and analysed without any activation. The X-ray diffractometer is a Bruker D8-Advance instrument and a cobalt source is used with a wavelength of 1.79 Å. The neutron powder diffractometer PEARL is used where the powders are placed in a 8 mm (OD) vanadium can (ID = 7.5 mm).

Then the nickel and iron electrodes are tested at various state of charges from 0 to 100%. The battery is taken apart and the nickel and iron pockets are separated. The pockets are first activated by six times repeated cycling and then partially charged towards the desired value. First the discharge capacity of the pockets is determined with repeated cycling, then the pockets are charged to the desired values, assuming that 100% of the inserted charge contributes to battery charging (ignoring losses due to hydrogen/oxygen production). The state of charge (SOC) is calculated by dividing the partial charge capacity with the discharge capacity. The Ni pockets are charged with a current of 0.333 A for 8 hours and discharged with 0.167 A until 1 V. These pockets are charged up to 0%, 21%, 43%, 58%, 78% or 102% of their total charge capacity. The Fe pockets are charged with a current of 0.5 A for 6 hours and discharged with 0.222 A until 1.1 V. These pockets are partially charged up to 0%, 20%, 39%, 60% or 90% of their total discharge capacity. Subsequently these pockets are rinsed three times with distilled water and the powder is taken out of the pocket. The powder is dried in a vacuum oven at 60˚C and finally the powder is stored in the glovebox to be measured when a batch is ready. The powder is either transferred to a vanadium can for the neutron powder diffractometer PEARL measurement at the TU Delft or transferred to a plastic vacuum globe for the X-ray Diffraction experiments. The XRD measurements are performed with a cobalt source (1.789 Å). In Table 4 and Table 5 is an overview of the nickel and iron samples respectively with increasing state of charge (SOC). For every sample is the weight of the powder, discharge capacity, partial charge capacity and specific capacity outlined. The specific capacity is calculated based upon the weight and discharge capacity.

Preliminary experiments for the in-situ neutron diffraction test setup are performed. Different thicknesses of quartz glass are tested for the amount of their background noise. Three different sizes of nickel foam current collectors are measured, namely with 2, 3 and 4 mm internal diameter.

Figure 16. Battery out of container (a), nickel (b) and iron (c) electrode

Table 4. Ni capacity calculations

Sample number	SOC (%)	Weight powder (g)	Discharge capacity(mAh)	Partial charge capacity (mAh)	Specific capacity(mAh/g)
6	0	7.37	-	0	-
2	21	7.42	1200	250	162
1	43	7.59	1160	500	153
3	58	8.04	1280	750	159
4	78	6.9	1290	1000	187
5	102	7.62	1270	1290	167

Table 5. Fe capacity calculations

Sample number	SOC of sample (%)	Weight powder (g)	Discharge capacity(mAh)	Partial charge capacity (Ah)	Specific capacity(mAh/g)
1	0	-	1305	0	-
2	20	6.17	778	155	126.094
3	39	-	1815	724	-
4	60	-	1790	1082	-
5	90	4.96	1602	1448	323.0

3 RESULTS

SEM, XRD and Neutron diffraction measurements are made on the battery nickel electrode powder and the iron electrode powder without activation. Then the nickel and iron pockets are analysed at successive charge states. For future in-situ neutron diffraction experiments, measurements are made to compare various thicknesses of quartz glass and sizes of nickel foam current collectors.

3.1 NICKEL ELECTRODE

3.1.1 BATTERY POWDER FROM THE SHELF

First the nickel powder is taken out of the battery and without any activation analysed with SEM-EDX (Figure 17). This gives an initial idea of the content of the material. A point analysis is performed on particular grains in the sample and the result is shown in the graph. Mostly Nickel, oxygen and carbon atoms are found, but also some grains with iron incorporated show up. Later on there is no iron found with XRD or ND, so maybe this is just sloppy handling and a spill over from the iron samples.

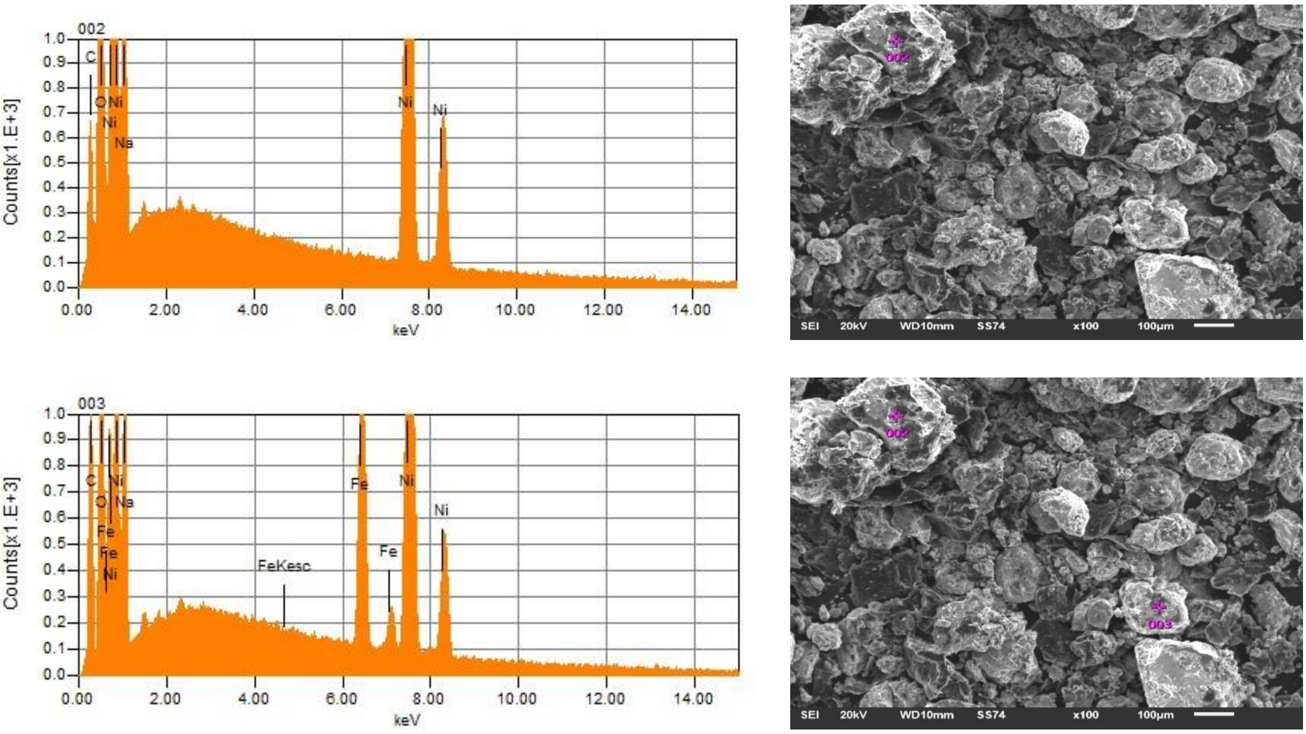

Figure 17. Unactivated nickel powder SEM-EDX grain analysis

Figure 18 shows the XRD results from the nickel powder without activation. 2 phases can be identified, β-Ni(OH)$_2$ and C. The nickel powder is placed in a 8 mm vanadium can and the unactivated Ni powder is measured with the neutron diffractometer (Figure 19). Here four phases are identified, but the γ-NiOOH turned out to be false, as can be seen by the weight fraction displayed in Table 6. Other phase properties can be found in Table 6 as well. The particle dimension of the graphite of 10 µm is reasonable, but for the nickel phases is too small. This result turned up with every refinement later on.

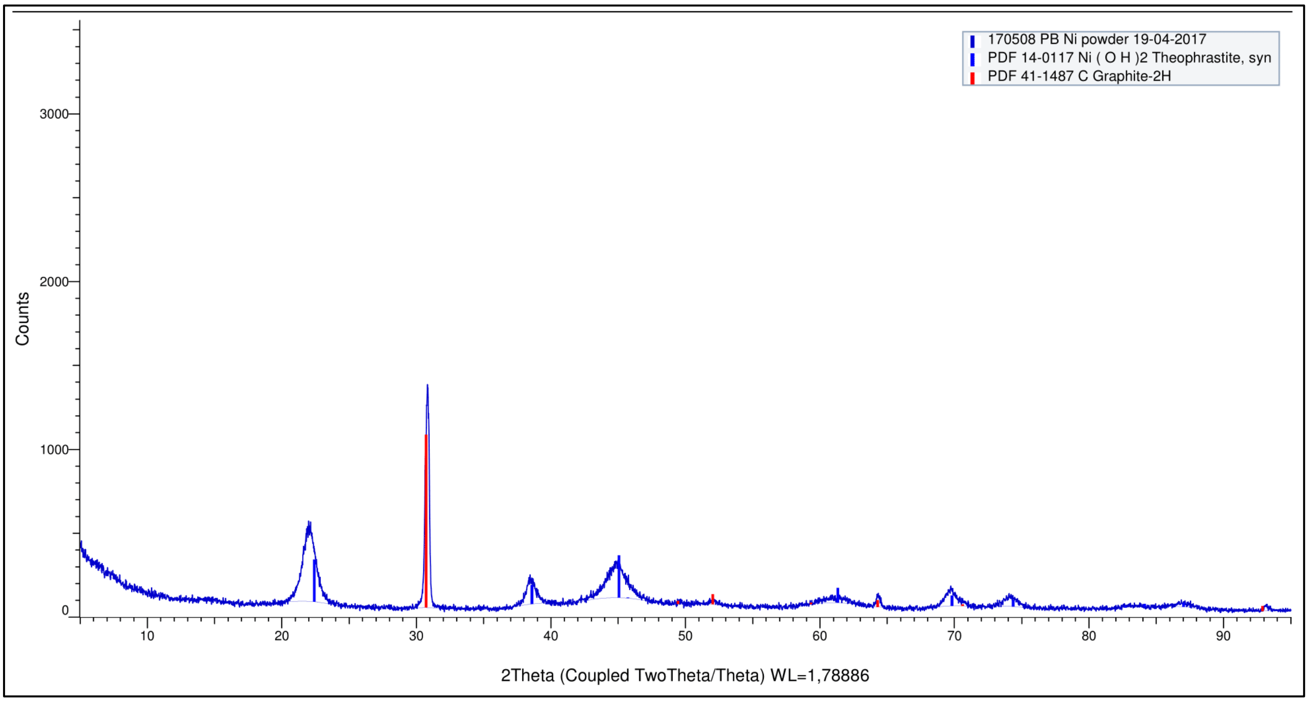

Figure 18. XRD results of the nickel electrode without activation

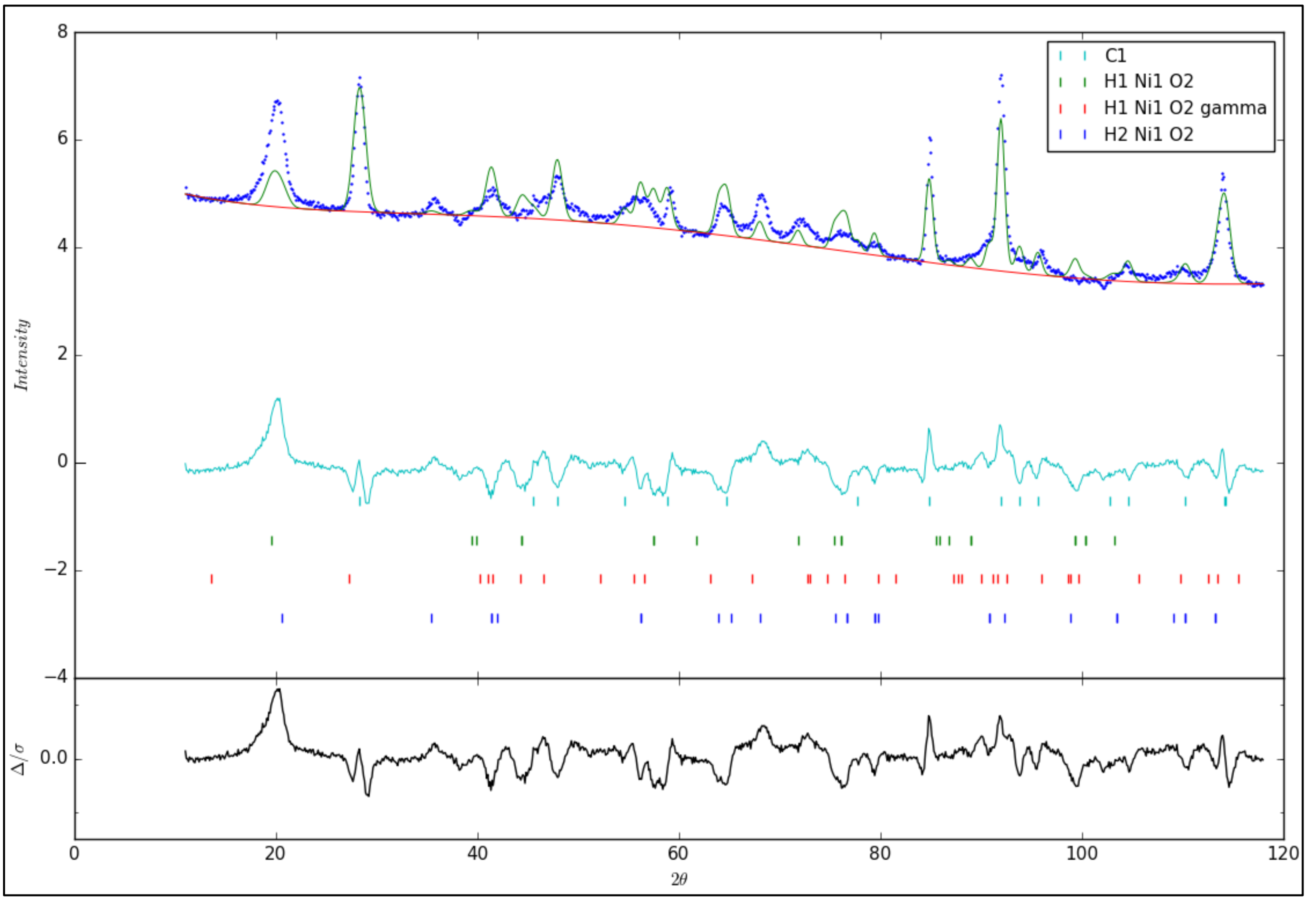

Figure 19. Rietveld refinement on ND pattern of nickel electrode without activation

Table 6. ND phase properties of Ni electrode without activation

Phase	Spacegroup	Unit cell parameters a; b; c (Å)	Weight fraction	Particle dimension (µm)
C	P 63 m c	2.448; a; 6.696	0.401	10
β-Ni(OH)$_2$	P -3 m 1	3.108; a; 4.585	0.380	0.001
β-NiOOH	P 3 m 1	2.808; a; 4.806	0.227	0.001
γ-NiOOH	R -3 m	2.77; a; 20.830	-0.007	-

3.1.2 X-RAY AND NEUTRON DIFFRACTION OF VARIED CHARGE STATES

The nickel electrode neutron diffraction and X-ray diffraction pattern at increasing charge states are shown in Figure 20. Peak fit on the neutron diffraction pattern of the nickel pockets with varied State of Charge and Figure 21, respectively. The first thing that stands out in Figure 20 is that with an increase in charge the background is decreasing, this in contrast to the XRD results (see Figure 21) which are placed at an offset to compare the different graphs. A peak fit is performed on the neutron diffraction pattern of nickel pockets at varied charge states (Figure 20). The peaks are indicated with colored vertical lines. The peaks at the red carbon line stay constant when charging. The peaks at the black Ni(OH)$_2$ lines decrease upon charge, which is in line with the expectation, because Ni(OH)$_2$ reacts to form NiOOH. That's also why peaks at the blue β-NiOOH and yellow γ-NiOOH line increase upon charge.

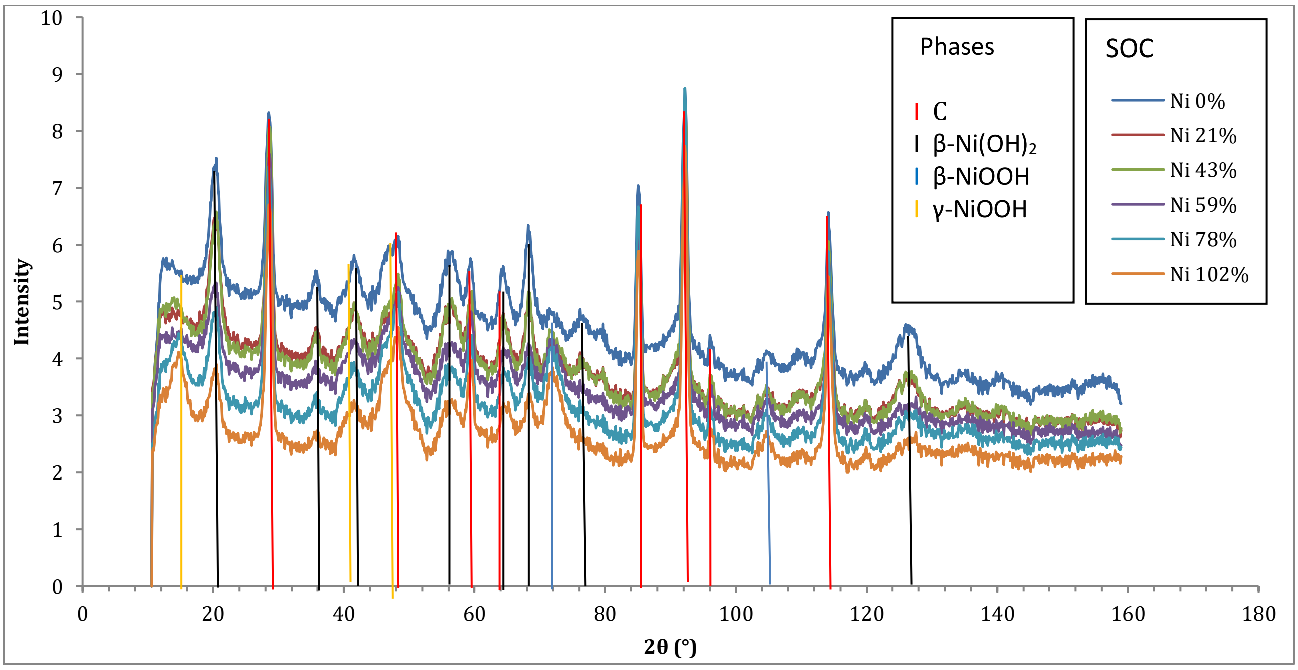

Figure 20. Peak fit on the neutron diffraction pattern of the nickel pockets with varied State of Charge

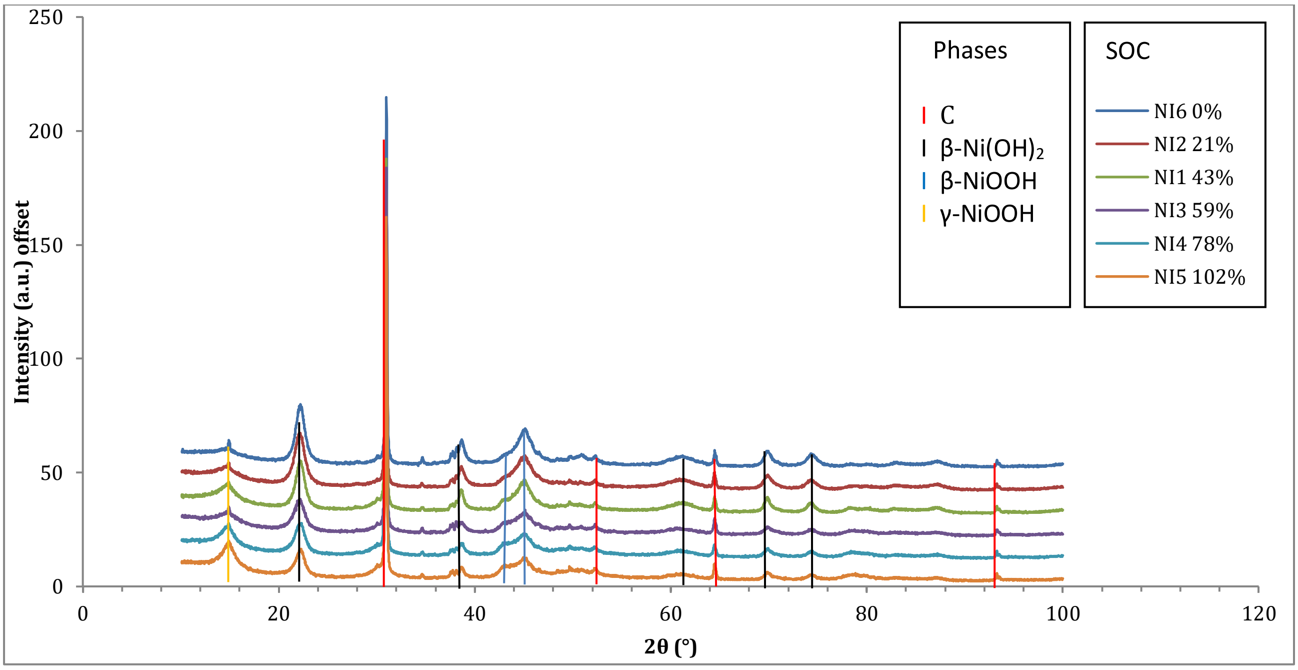

Figure 21. Peak fit on nickel pockets XRD with varied State of Charge (cobalt source, l=1.78886 Å)

The Rietveld refinement is performed simultaneously on the X-ray and neutron diffraction measurements for the same sample. The background is refined with the chebschev background function. X and Y displacement sample parameter and instrument parameters U,V and W are refined. For all samples the phase fractions are refined and for some the strain, size and unit cell parameters. In Figure 22-Figure 25 XRD and ND Rietveld refinements of samples ni 0% and 102% are plotted. Each samples is indicated with its SOC, for example 'Ni 0%' is a nickel sample with a SOC of 0%. The blue dotted pattern is the diffraction measurement, the green pattern is the Rietveld refinement model and the red line is the background function. The error function, which is the mismatch between the measurement and refinement model, is displayed as the black and turquoise pattern and in the legend the different phases corresponding to the colored stripes are found.

For ni 0% the Rietveld refinement fits well over the ND measurements. Only at a 2θ of 48° the refinement is not following the measurement. In the XRD measurement are the $Ni(OH)_2$ and NiOOH peaks broader than the carbon peaks. The refinement over the XRD measurement is less accurate, the peaks of the refinement are broader overall. Also is the carbon peak at 31° measured much higher than the refinement. In Figure 24 and Figure 25 the ND and XRD measurements of the ni 102% are shown. Here the ND refinement is less accurate, the refined peak at 15° is shifted to the left and at 72° the peak is too small. And again around 48° a broader peak is expected. For the XRD refinement the large carbon peak is refined very well, but some other peaks are too small in the refinement.

Crystal structures are taken from the ICSD database. Several phases have been tried on the rietveld refinement, also the same phase from different sources. The crystal structure data of Vadlamani et al.(C) [28], Kazimirov et al.(β-$Ni(OH)_2$ and β-NiOOH P3M1) [29] and Morishita et al.(γ-NiOOH) [11] gave the best fit. The γ-Fe [30], β-NiOOH C1M1 [29] and Ni phases where also tried, but did not result in a proper fit.

C [28]
β-$Ni(OH)_2$ [29]
β-NiOOH P3M1 [29]
γ-NiOOH [11]

From the phase fraction the weight fraction is calculated and plotted in Figure 26 (ND) and Figure 27 (XRD). The percentage carbon in the XRD is higher than for ND. For the ND measurements the β-$Ni(OH)_2$ content is decreasing and the γ-NiOOH content is increasing after 43%. β-NiOOH has a wave like function it increases until its peak at 58% and then decreases again. For XRD the carbon content is increasing and β-$Ni(OH)_2$ decreases with an increase in charge state. Whereas the β-NiOOH slowly decreases and γ-NiOOH increases, but both are much smaller than in the ND measurements.

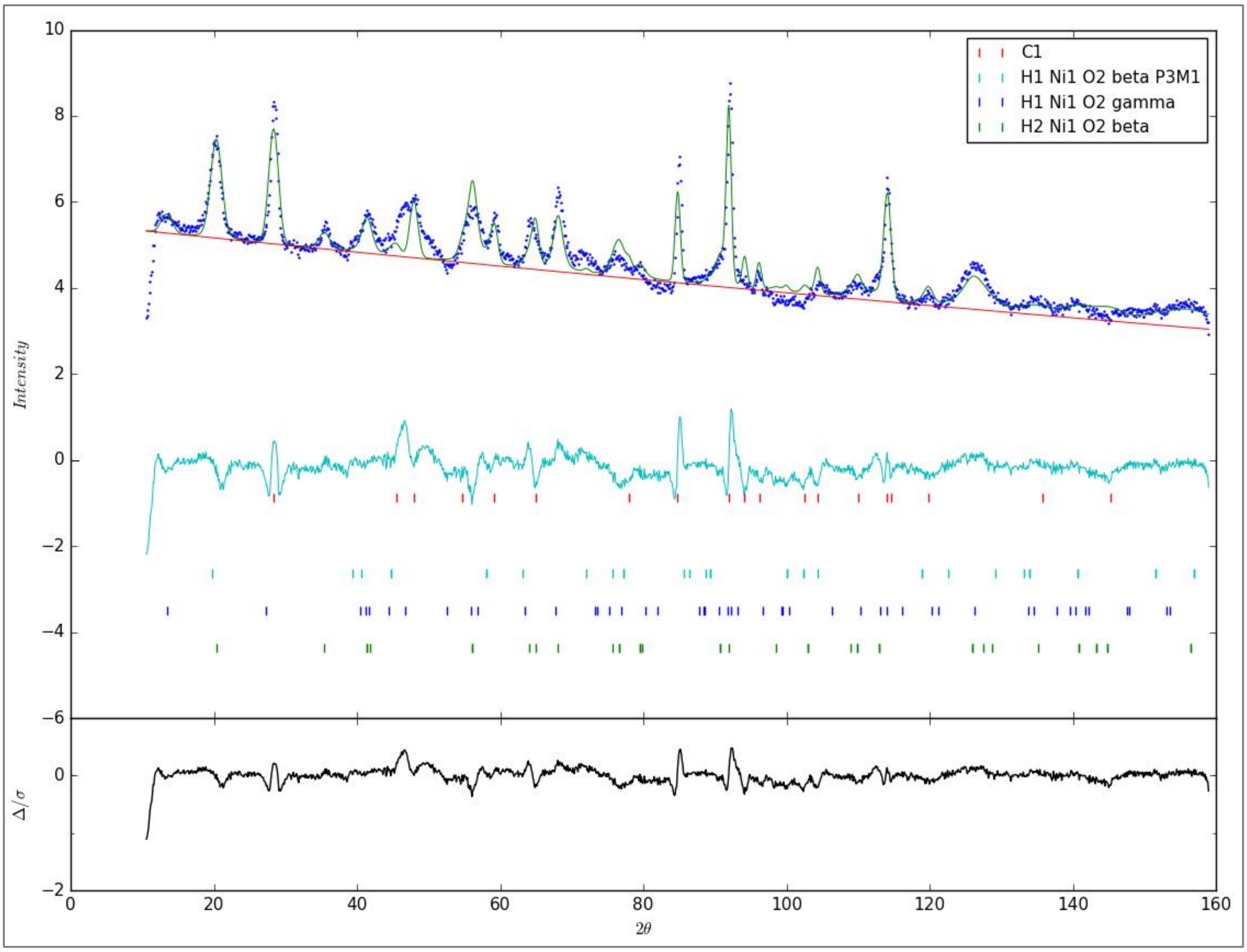

Figure 22. Rietveld refinement on neutron diffraction pattern of ni 0%

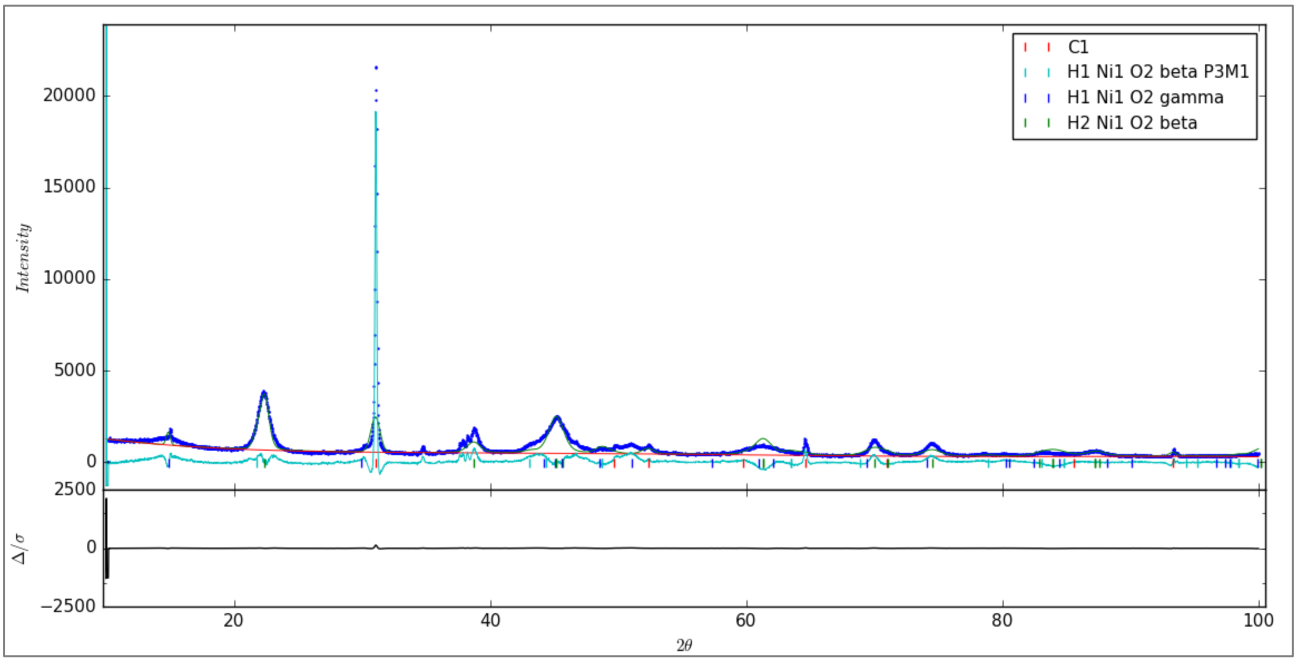

Figure 23. Rietveld refinement on X-ray diffraction pattern of ni 0%

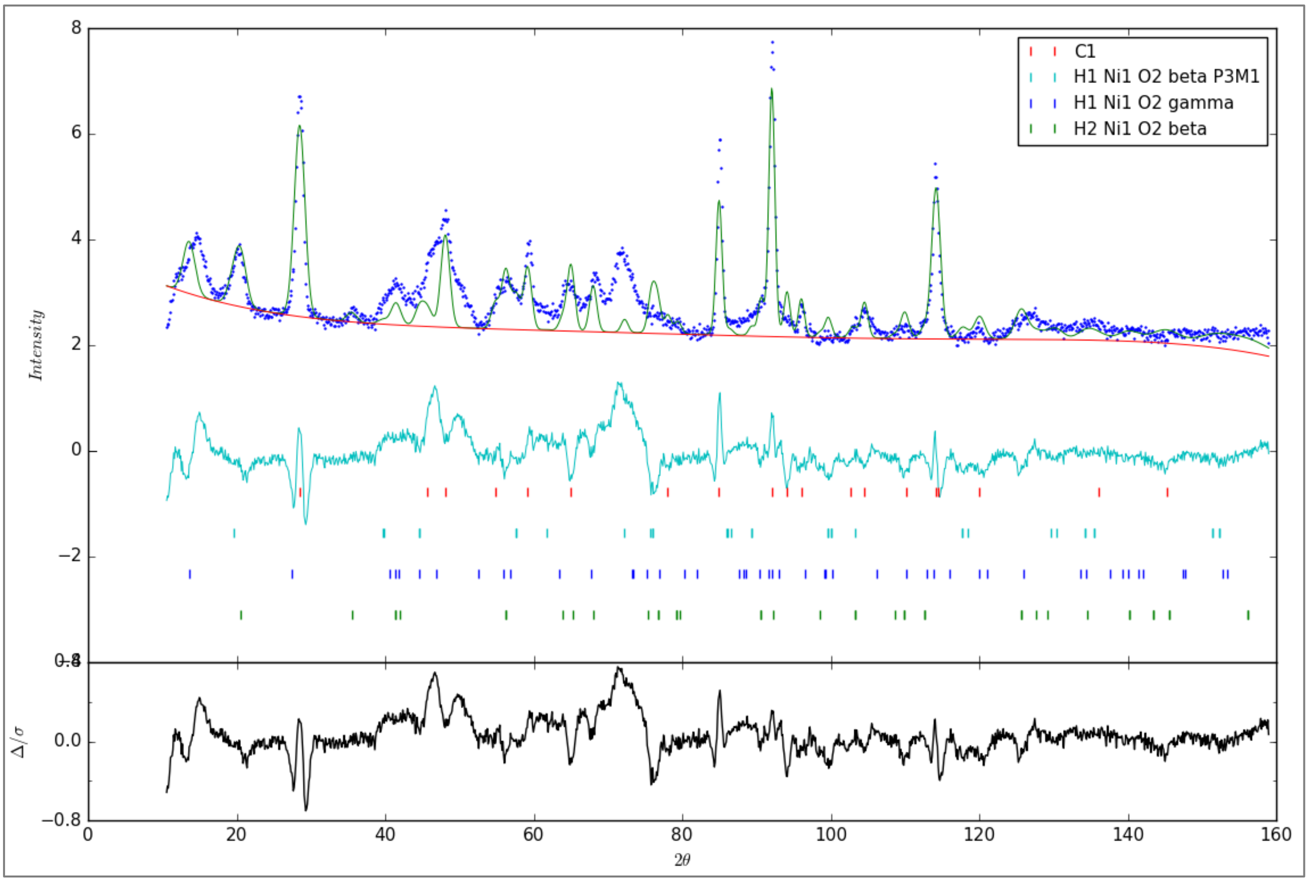

Figure 24. Rietveld refinement on neutron diffraction pattern of ni 102%

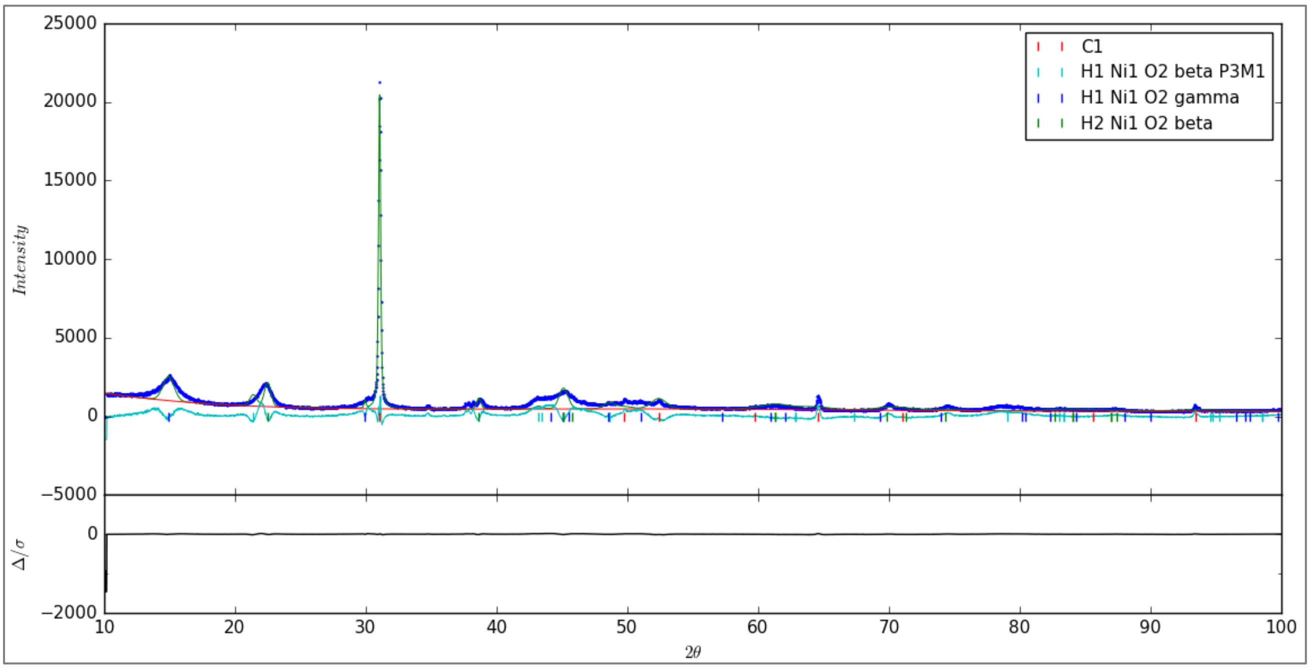

Figure 25. Rietveld refinement on X-ray diffraction pattern of ni 102%

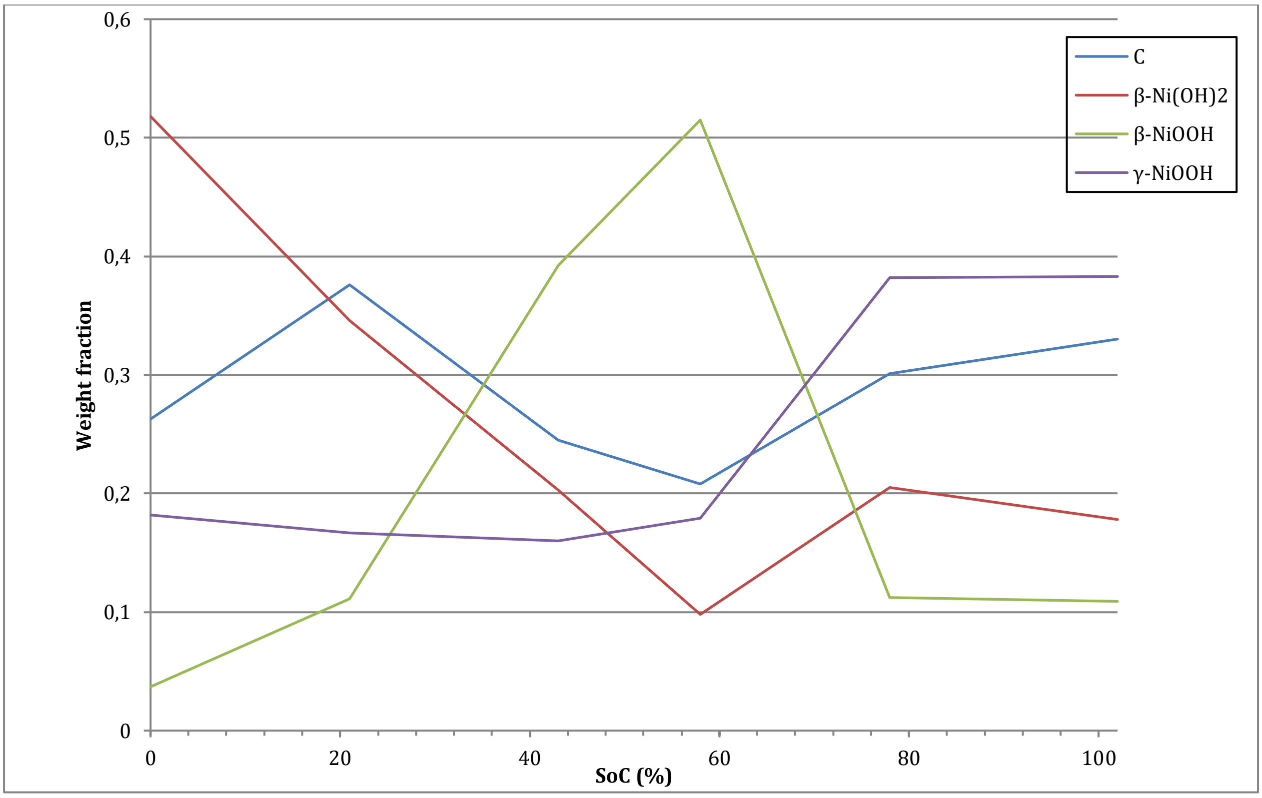

Figure 26. Weight fraction of the nickel electrode phases with increasing state of charge (deducted from the Rietveld refinement on the ***neutron diffraction*** *patterns)*

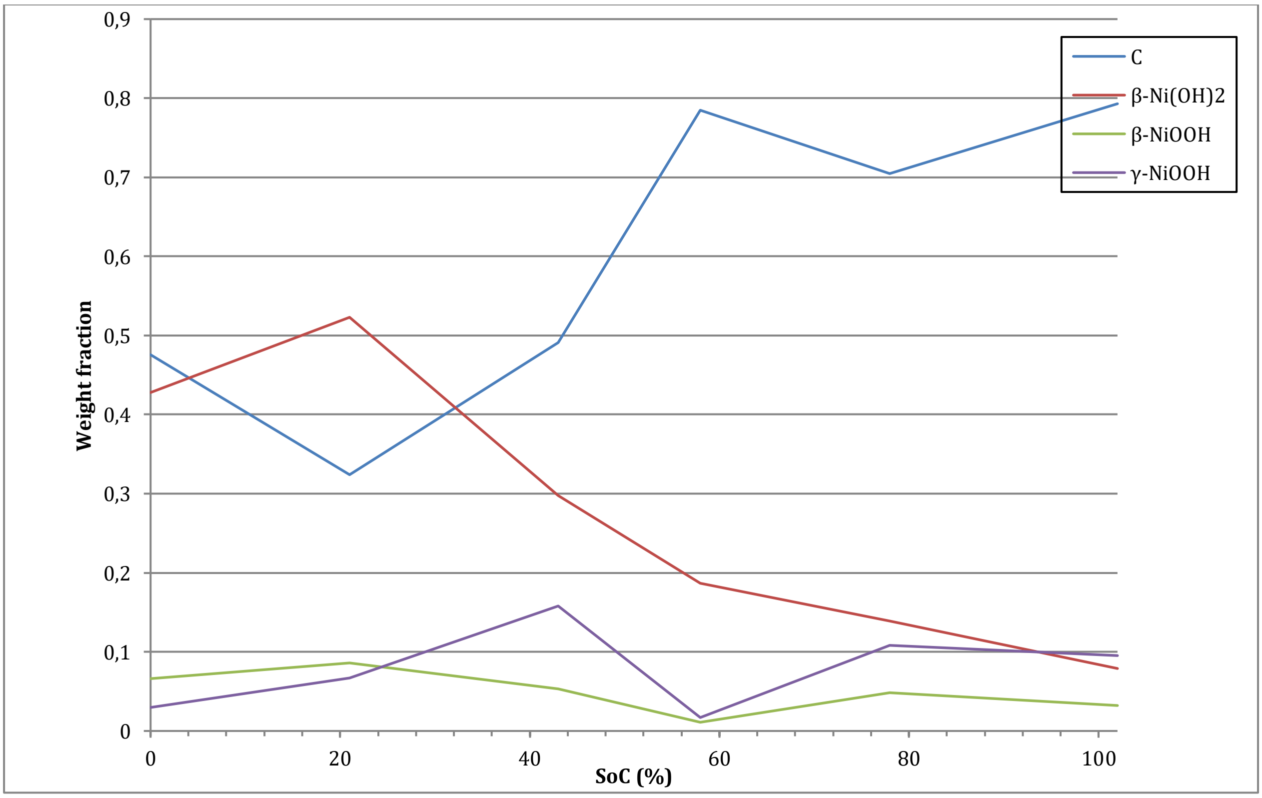

Figure 27. Weight fraction of the nickel electrode phases with increasing state of charge (deducted from the Rietveld refinement on the ***X-ray diffraction*** *patterns)*

3.2 IRON ELECTRODE

3.2.1 BATTERY POWDER FROM THE SHELF

The iron powder is also analysed with SEM-EDX. In Table 7 a rough initial iron material composition can be found. The elements carbon, oxygen, sodium and iron are identified. On the image (Figure 28) can be seen that the Fe powder is a very porous material and the carbon is encapsulated by the iron or carbon is a background from the carbon tape. The Na is probably a remainder of the dried electrolyte. In a more detailed analysis with XRD and ND (Figure 29 and Figure 30) four phases are identified, namely carbon, iron, goethite and iron oxide. For the neutron diffraction analysis all peaks are represented in the Rietveld refinement, resulting in a good fit. In Table 8 are the phase properties resulting from the refinement on the neutron diffraction pattern shown. The particle dimensions of Fe and FeOOH when included in the refinement went towards 1 nm, so where not refined.

Table 7 SEM-EDX analysis on Iron electrode

Full picture analysis 500x			Grain analysis 200x		
atom	Mass%	Atom%	atom	Mass%	Atom%
C	20.41	36.40	C	37.90	50.94
O	31.91	42.72	O	37.06	37.39
Na	4.73	16.49	Na	10.72	7.53
Fe	42.96	16.48	Fe	14.31	4.14
Total	100.00	100.00	Total	100.00	100.00

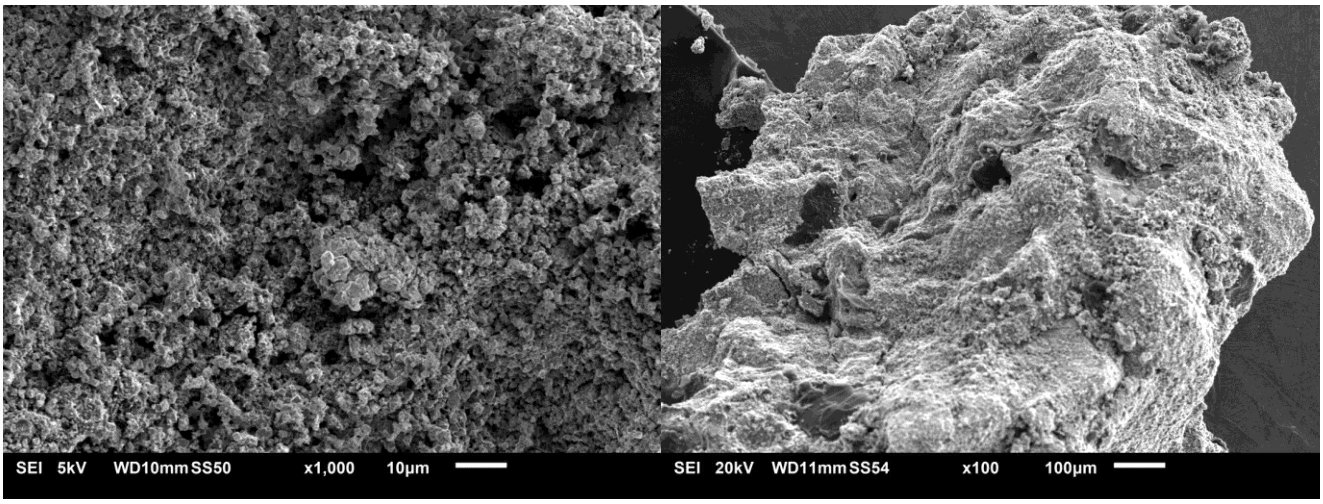

Figure 28. Iron powder SEM-EDX analysis

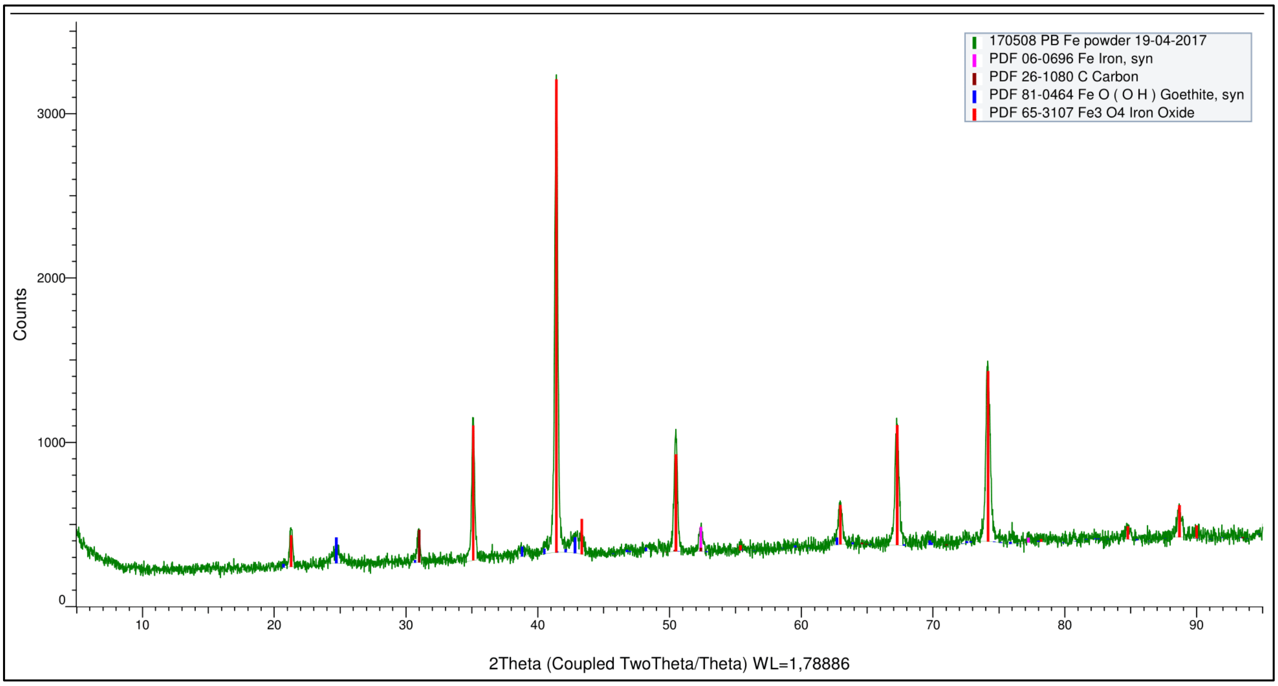

Figure 29. XRD results of the iron electrode without activation

Neutron diffraction results of the iron powder.

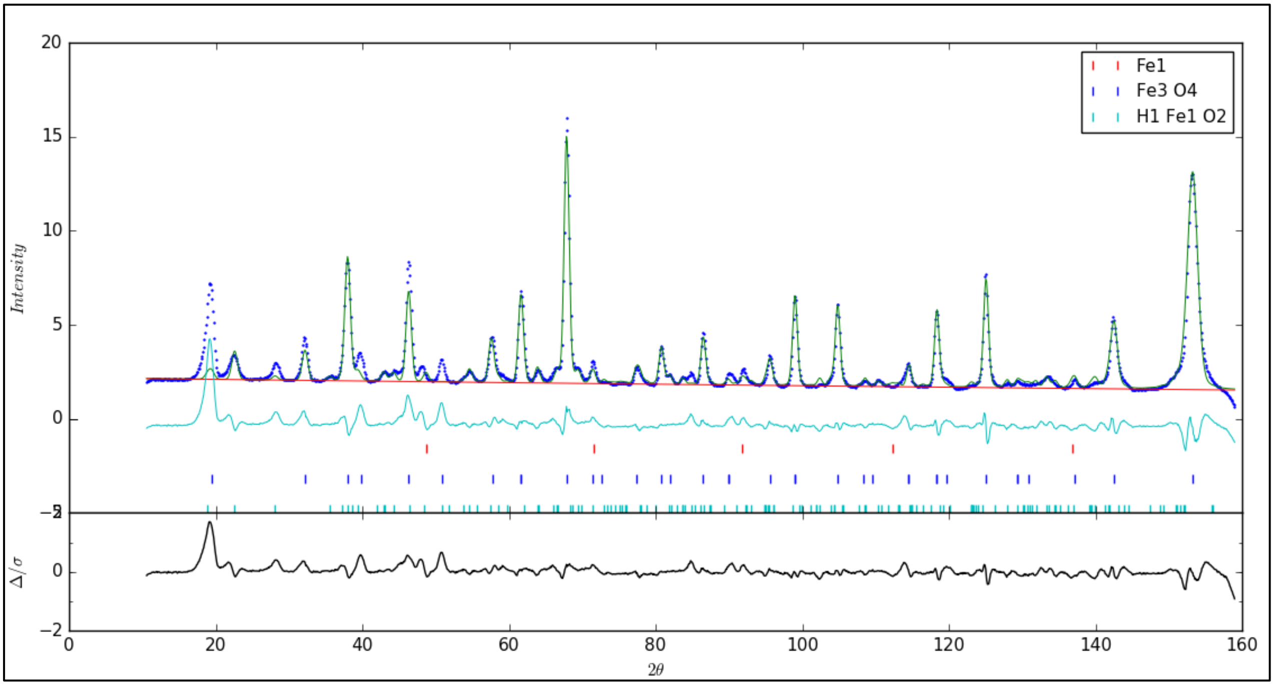

Figure 30. Rietveld refinement on the ND pattern of the iron electrode without activation

Table 8. ND phase properties of Fe electrode without activation

Phase	Spacegroup	Unit cell parameters a; b; c (Å)	Weight fraction	Particle dimension (μm)
Fe	Im-3m	2.833	0.019	-
Fe_3O_4	Fd-3m	8.395	0.775	0.301
FeOOH	Pbnm	4.609; 9.962; 3.021	0.206	-

3.2.2 X-RAY AND NEUTRON DIFFRACTION AT VARIED CHARGE STATES

All iron samples are measured by X-ray (Figure 32) and neutron diffraction (Figure 31). The X-rays are plotted with an offset, from up (0%) towards down (90%). ND patterns have no offset, the background lowers with an increase in charge state. The peaks are identified and marked with colored vertical lines. Four phases are identified in the samples, that is Fe, Fe_3O_4, $Fe(OH)_2$ and FeOOH. The high peaks are identified as pure Fe, the vertical blue lines are Fe_3O_4 and the green lines are FeOOH.

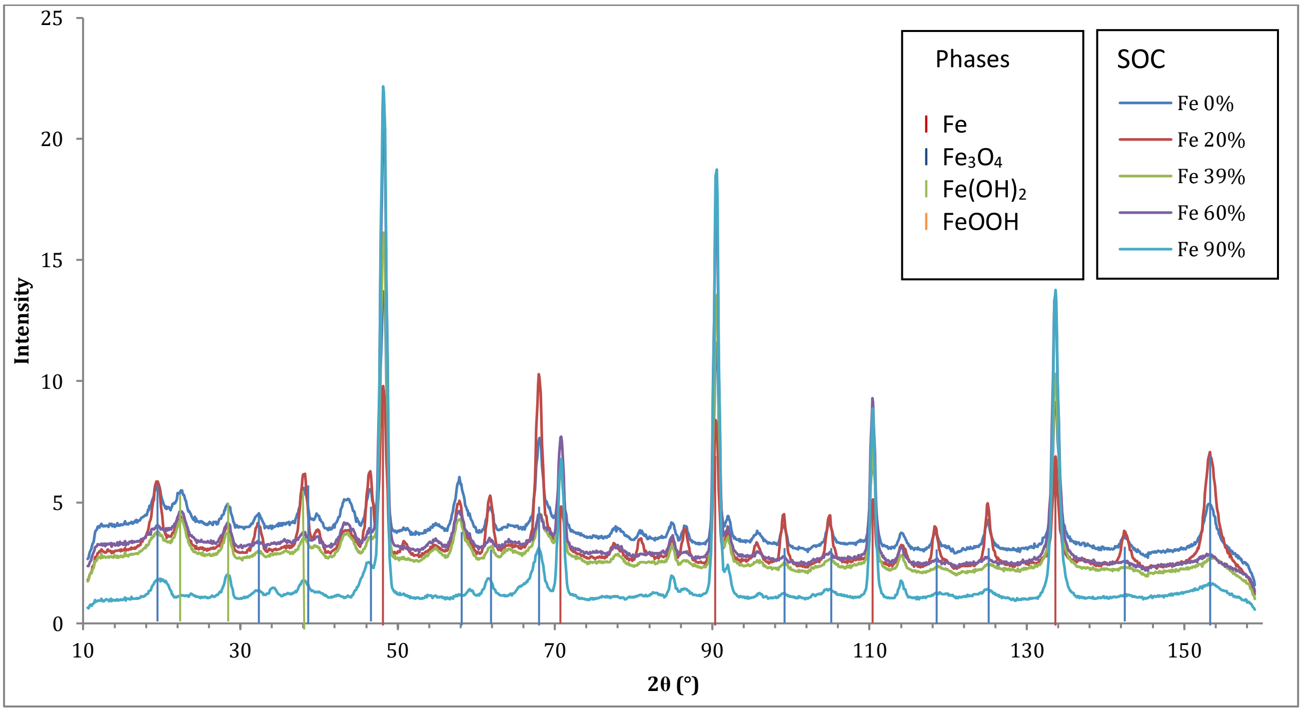

Figure 31. Peak fit on the neutron diffraction pattern of the iron pockets with varied State of Charge

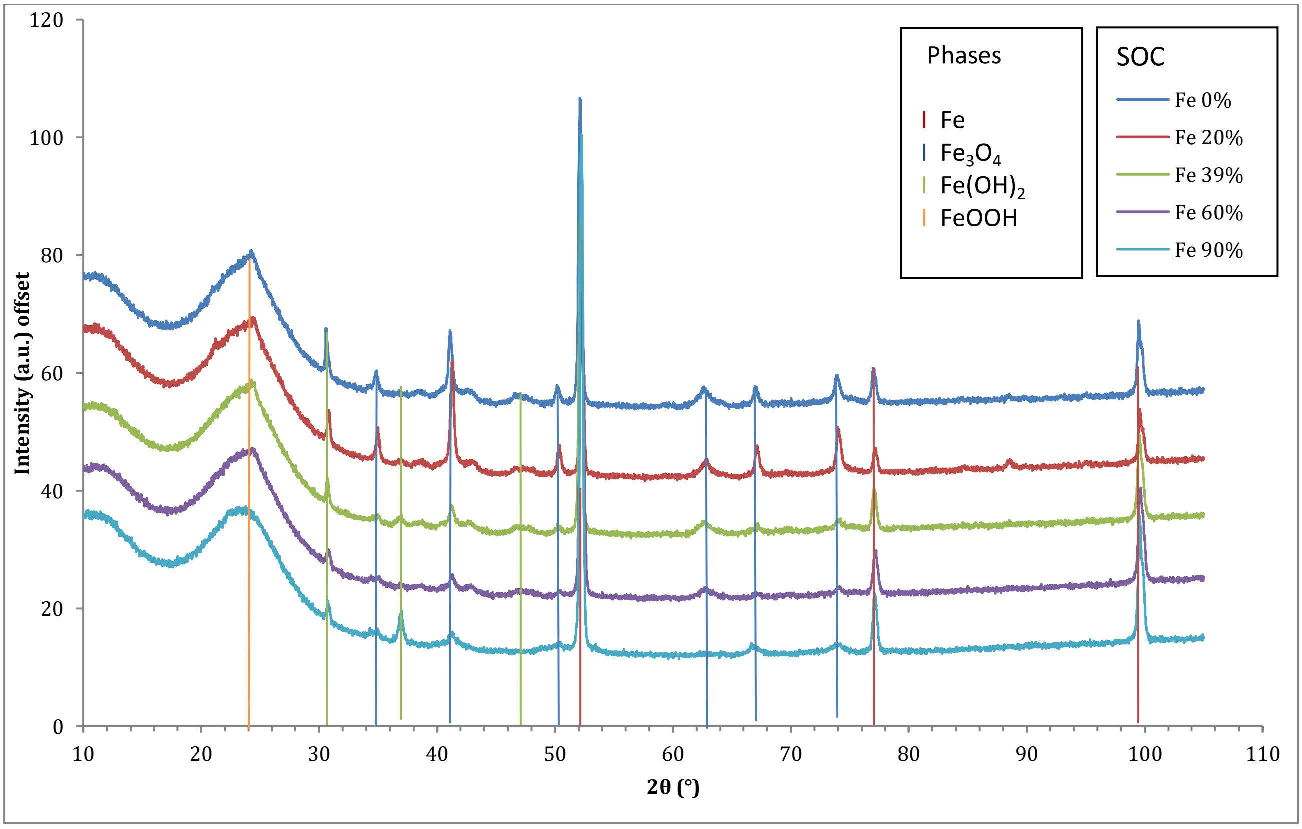

Figure 32. (Peak fit on the) X-ray diffraction on iron samples at varied SOC (Cobalt source, l=1.78886 Å)

The diffraction patterns are analysed by Rietveld refinement. The Fe 0% sample with 0% State of Charge (Figure 33 and Figure 34) and the Fe 90% sample (Figure 35 and Figure 36). The Rietveld refinement is performed simultaneously on the X-ray and neutron diffraction measurements for the same sample. The background is refined with the chebschev background function. X and Y displacement sample parameter and instrument parameters U,V and W are refined. The phase fraction, strain and particle size are refined separately for ND and XRD by GSAS II. For all samples the phase fractions are refined and for some the strain, particle size and unit cell parameters. Each samples is indicated with its SOC, for example 'Ni 0%' is a nickel sample with a SOC of 0%. The blue dotted pattern is the diffraction measurement, the green pattern is the Rietveld refinement model and the red line is the background function. The error function, which is the mismatch between the measurement and refinement model, is displayed as the black and turquoise pattern and in the legend the different phases corresponding to the coloured vertical lines are found. The iron ND results can be refined reasonably well with Rietveld refinement. The first peak around 20˚ is smaller in the refinement. Here again XRD gives issues, the peak around 24˚ is much broader than the refinement. The rest of the peaks are properly refined by GSAS II.

Several phases have been tried on the rietveld refinement, also the same phase from different sources. The crystal structure data of α-Fe [31], Fe_3O_4 [32] and α-FeOOH [33] resulted in the best refinement. Three different Fe phases are tested for the refinement, namely the α, δ [30]and γ [30][34] phase, where α -Fe came out as the best fit. The $Fe(OH)_2$ [35] and C [28] were also used in the refinement, but did not fit the measurement.

α-Fe [31]
Fe_3O_4 [32]
α-FeOOH [33]

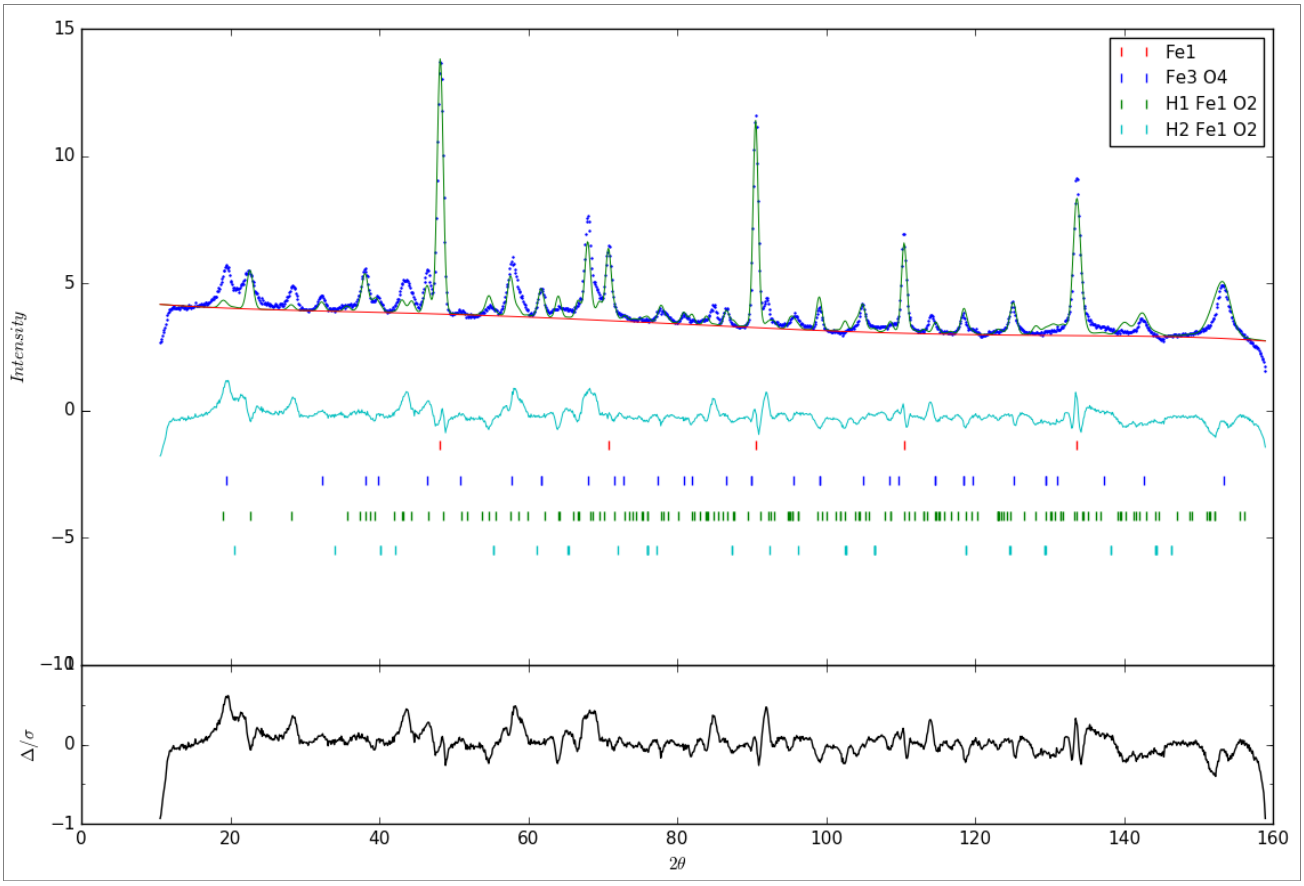

Figure 33. Rietveld refinement on neutron diffraction pattern of Fe 0%

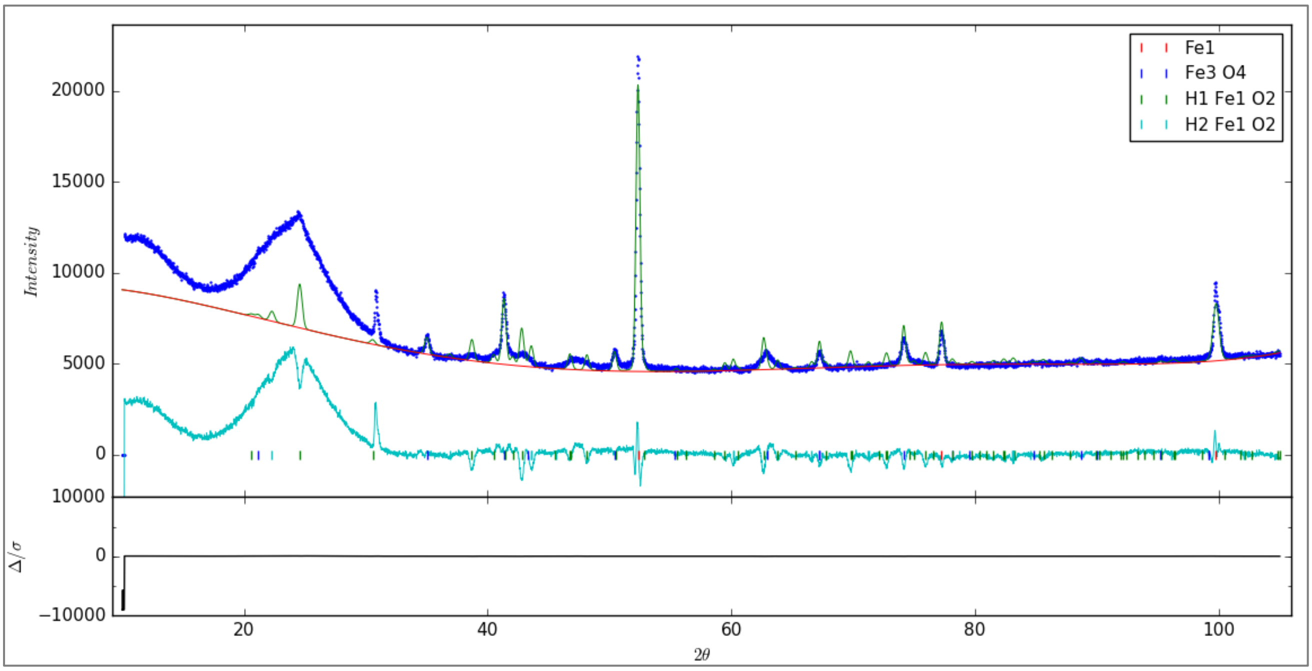

Figure 34. Rietveld refinement on X-ray diffraction pattern of Fe 0%

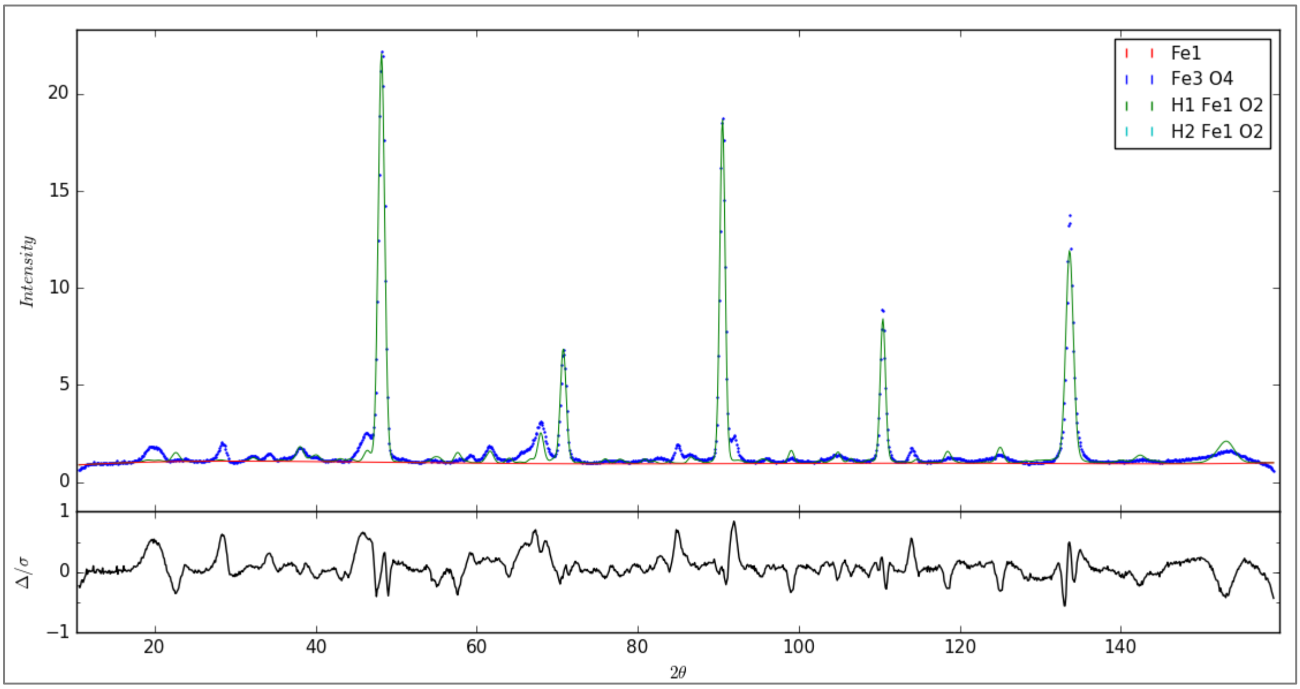

Figure 35. Rietveld refinement on neutron diffraction pattern of Fe 90%

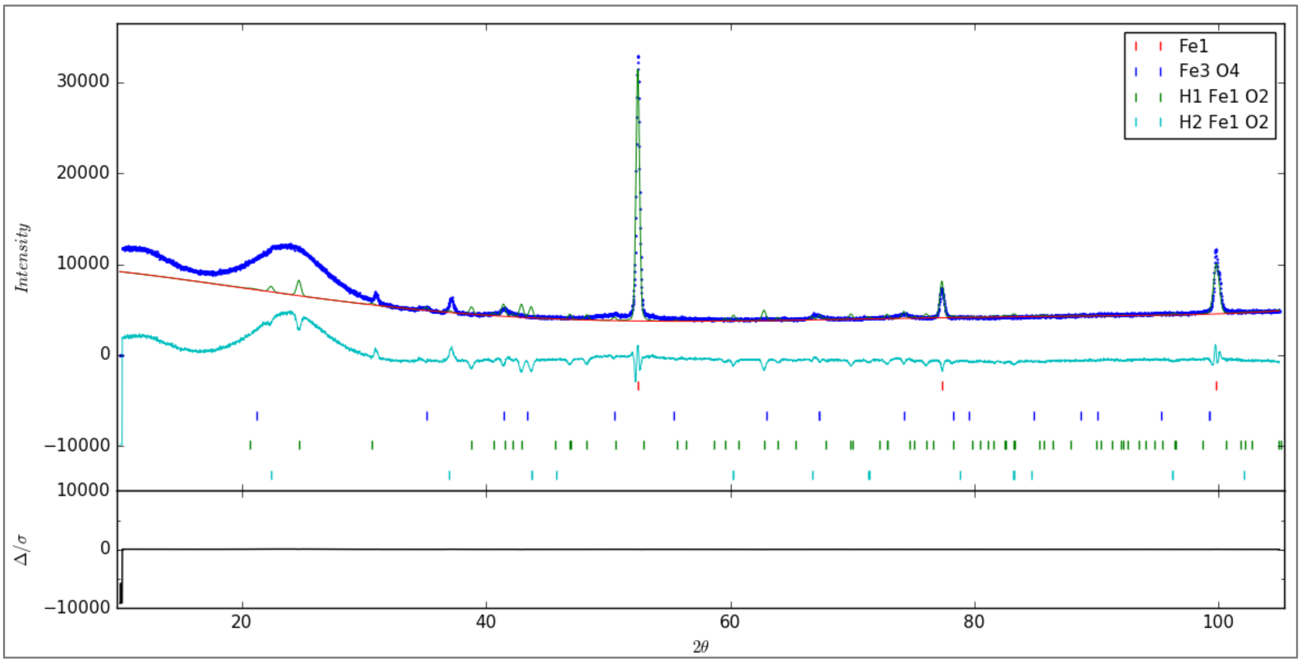

Figure 36. Rietveld refinement on X-ray diffraction pattern of Fe 90%

The phase fractions per sample are determined with the refinement and here from are the weight fractions deducted and plotted in Figure 37 and Figure 38. The weight fraction of Fe increases and FeOOH decreases with increasing state of charge. The samples from 39% - 90% demonstrate a lower Fe_3O_4 weight fraction, these samples are better activated. In contrast the second sample (20% of SOC) has more Fe_3O_4 which indicates it is not activated properly. The graph also visualizes that the $Fe(OH)_2$ content is very low for any of these samples.

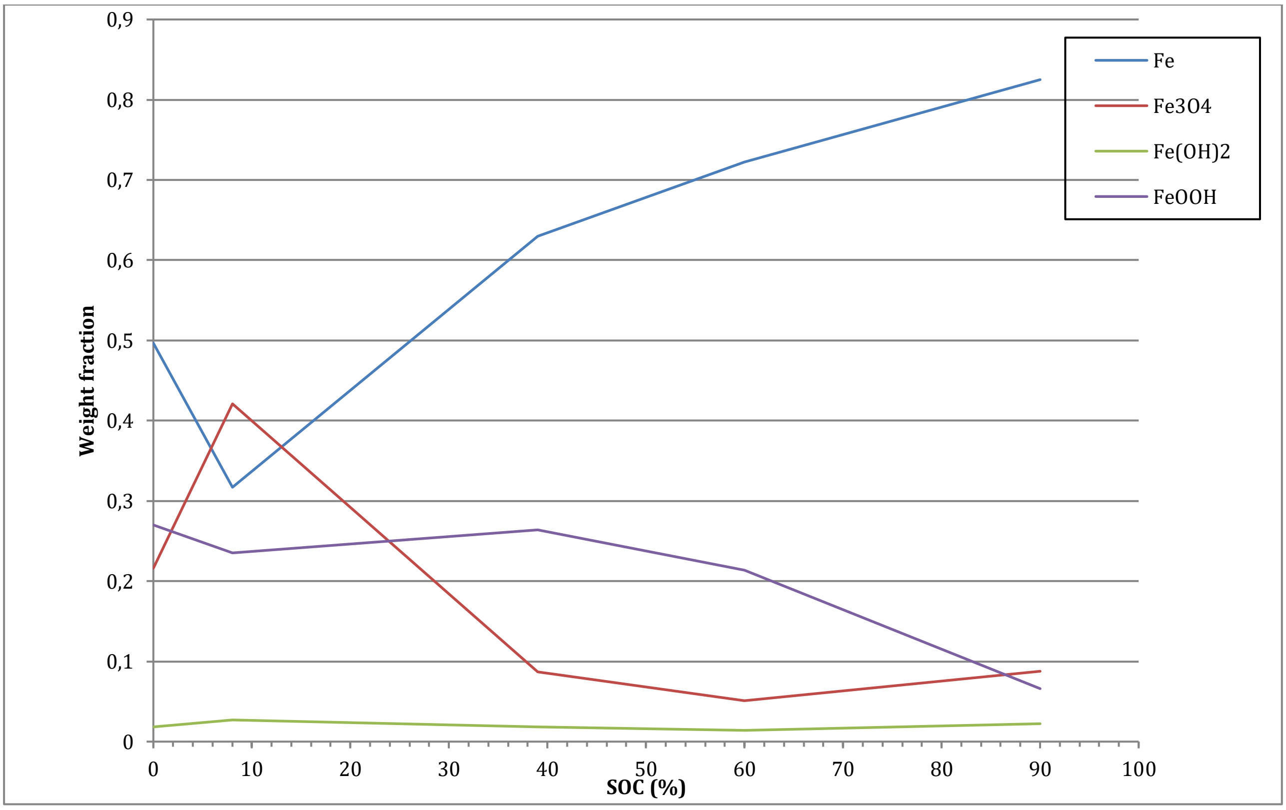

*Figure 37. Weight fraction of the iron phases with increasing state of charge (deducted from the Rietveld refinement on the **neutron diffraction** patterns)*

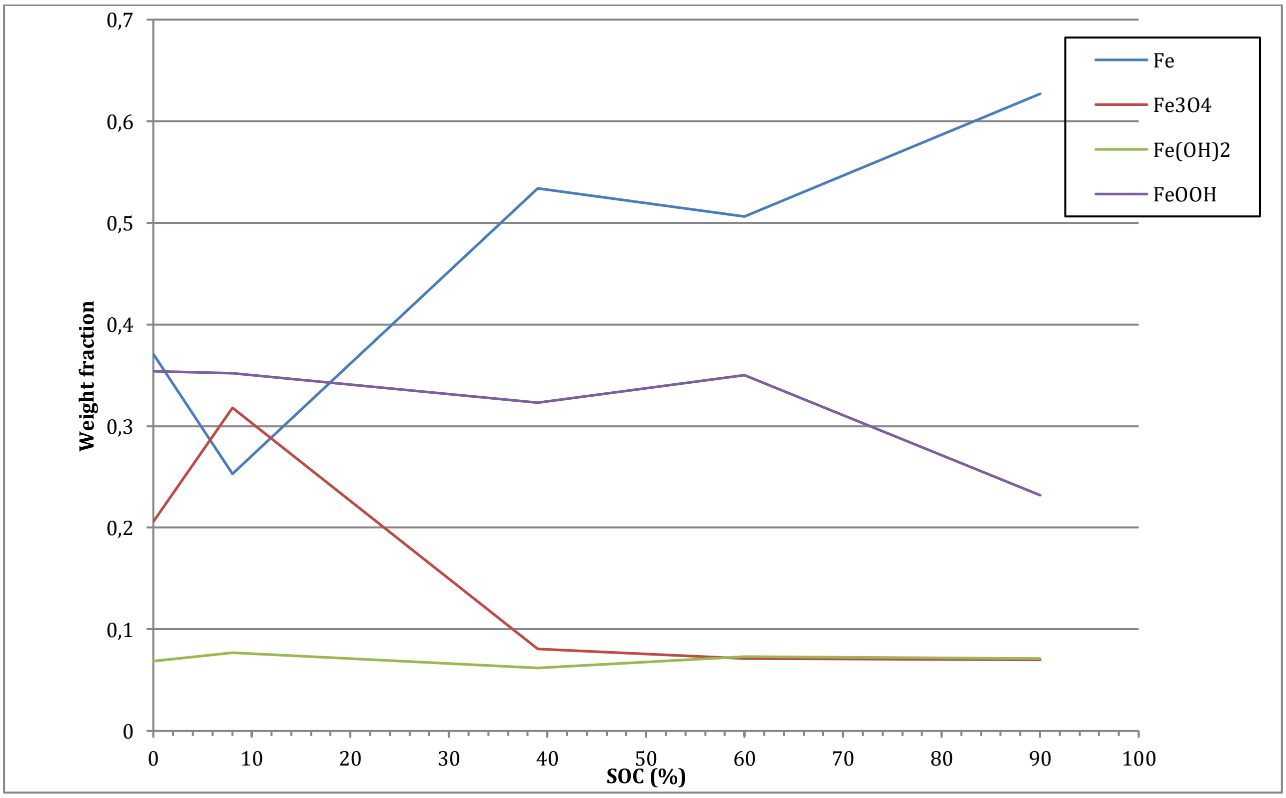

*Figure 38. Weight fraction of the iron phases with increasing state of charge (deducted from the Rietveld refinement on the **X-ray diffraction** patterns)*

3.2.3 PRELIMINARY EXPERIMENTS FOR IN-SITU TEST SETUP

The effect of wall thickness of quartz glass on the background noise with neutron diffraction is shown in Figure 39. The background is decreasing with increasing thickness. Several diameters of nickel foam electrodes are examined (Figure 40). Here no specific change in the neutron diffraction pattern is observed.

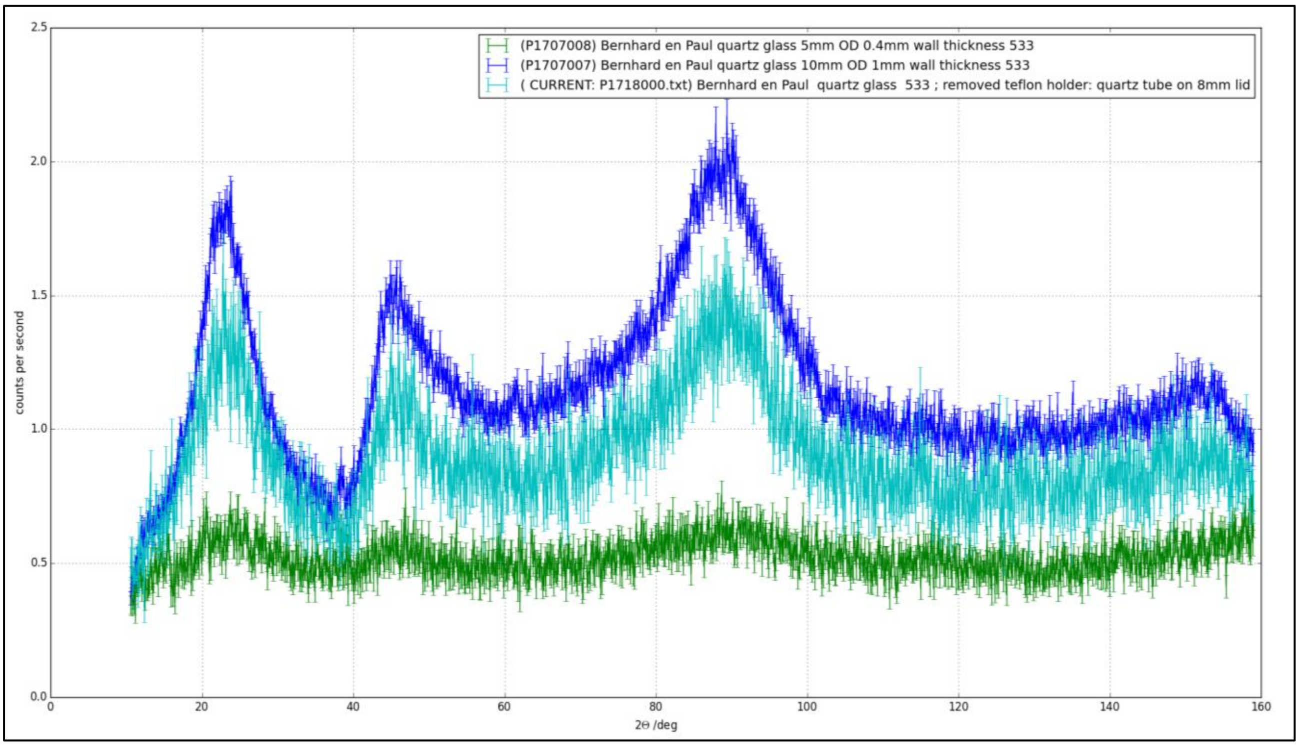

Figure 39. Neutron diffraction patterns of quartz glass with varied wall thickness

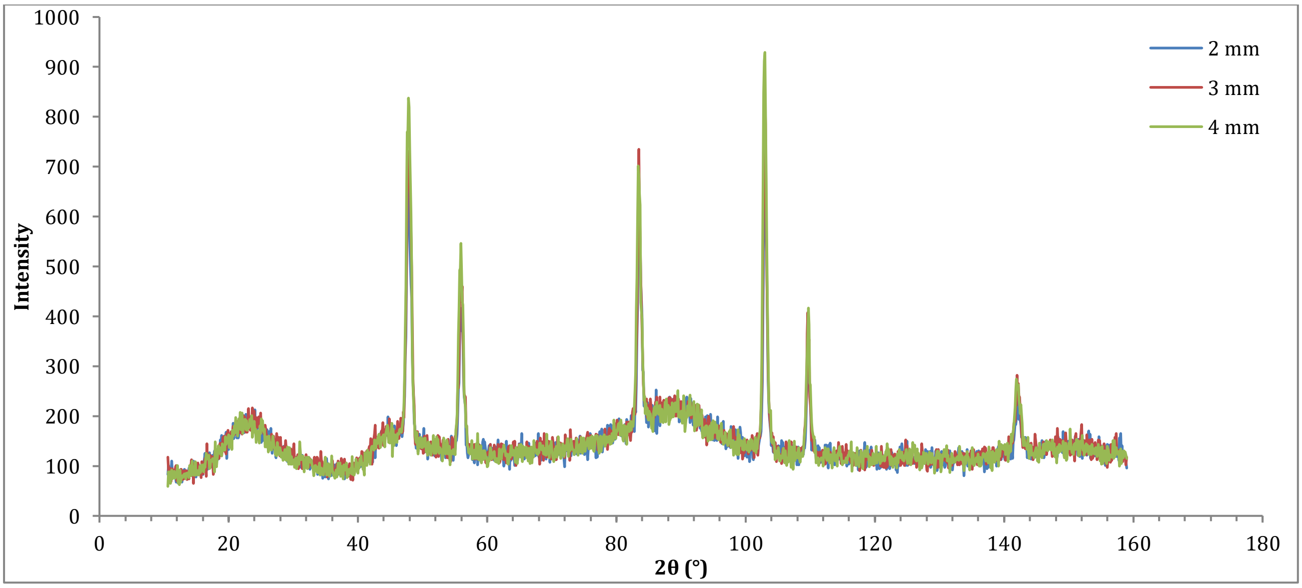

Figure 40. Neutron diffraction comparison of ni foam current collector with a inner diameter of 2, 3, or 4 mm

4 DISCUSSION

4.1 NICKEL ELECTRODES

4.1.1 BATTERY POWDER FROM THE SHELF AND PURE NI(OH)$_2$ NEUTRON DIFFRACTION

From the SEM and XRD analysis only the two compounds carbon and β-$Ni(OH)_2$ come to light. The ND analysis also shows β-NiOOH in the refinement. The particle dimension of the graphite of 10 μm is reasonable, but a particle dimension of 1 nm for the nickel phases is too small. This result turned up with every refinement later on. This has been stated in previous research and has been attributed by Morishita et al. to an ideal and fault phase. Here the ND patterns shift a little bit from each other apart, this is broadening the peaks. This research was not able to replicate the ideal and fault phase model, because during the refinement one of the phases would become very negative and they would substract from each other.

4.1.2 X-RAY AND NEUTRON DIFFRACTION AT VARIED CHARGE STATES

Neutrons are very sensitive to H-atoms and it is an incoherent scattering process (resulting in a higher background when more hydrogen is present). The first thing that stands out in Figure 20 is with increase in charge the background is decreasing, which indicates a decrease in H protons. This is what we would expect, because upon charge

$$Ni(OH)_2 + OH^- \rightarrow NiOOH + H_2O + e^-$$

The peak fit on the neutron diffraction pattern shows there are, next to the carbon, 3 phases present. The carbon has a weight fraction fluctuating around 0.3. The fluctuation is probably caused by the varying carbon amounts in the different samples. At 0% SoC a weight fraction of 0.182 γ-NiOOH is still present in the ND results. It is not clear why this is found. The γ-NiOOH is formed under high charge and overcharge, at 0% SoC there should be no γ-phase yet. Maybe during the activation the charge applied was too high, which resulted in γ-NiOOH formation. A reason why this does not convert back to β-$Ni(OH)_2$ during discharging can be due to a loss of contact in a part of the sample causing some part not to discharge. In a next cycle such parts may become connected again or not. One normally does not reach the theoretical capacities for Ni nor Fe electrodes.

If the carbon is left out in the weight calculations as in Figure 41, the nickel(oxy)hydroxide phases can be compared with the phase abundance of Morishita et al.(Figure 42) A comparison can be made between the fractions at 0%, 50% and 100% SOC. For Morishita et al. at 0% of SOC only the β-$Ni(OH)_2$ phase is apparent. At 50% of SOC the transformation towards β-NiOOH is in full motion with 40 $_{wt}$% already converted. At 100% of SOC almost all is transformed in β-NiOOH and the γ-NiOOH appears only at 150% of SOC with a fraction of 18 $_{wt}$%. Significant differences are found when compared with the result of this report. At 0% SOC the β-$Ni(OH)_2$ phase is 70 $_{wt}$%, this is significantly smaller than Morishita et al. Around 50% of SOC the β-$Ni(OH)_2$ transforms towards 58 $_{wt}$% β-NiOOH, this is a faster transition than M. found. At last for 100% SOC the largest fraction is γ-NiOOH with 57 $_{wt}$%, but this phase is not at all present yet in the measurements of Morishita et al.

Morishita et al. did not specify how they determined the state of charge, so maybe they calculated the SOC in a different way. There are different methods to estimate the SOC, it can be categorised into direct measurement and indirect estimation. As direct measurements the electrolyte PH, density measurements and cathodic galvanostatic pulses can be used. Here for accurate measuring device are needed, which can be expensive, and access to the battery materials is not always possible. Indirect estimation methods are easier to apply, those are voltage method, coulomb counting, a combination of voltage and coulomb counting method, Kalman filtering and pressure method. In the voltage method the voltage of the battery is used to calculate the SOC, this method is not very accurate. The Coulomb counting, or also called the current integration method, is an integration over time of the current used by the battery. Because there is no reference point, this method suffers from long-term drift. A combination of voltage and coulomb counting method is already better than each method on their own. Kalman filtering is a well-designed and proven method to estimate the SOC. The system input and output measurements are filtered to give a estimation of the dynamic SOC. [36] The pressure method can specifically be used for NiMH batteries because the pressure increases when the battery is charged. [37]

For the calculation of the SOC, efficiency losses were not taken into account, but this results in an even lower SOC, as a consequence the results diverges even more. Also they distinguished between an ideal and fault phase, this is not retrieved in the neutron diffraction analysis. The ideal and fault phase model are tested with Rietveld refinement on both beta phases, but the refinement did not improve with the distinction between ideal and fault phase. The c-parameter of γ-NiOOH is in agreement with Morishita et al. with a lattice distance of 20.8 Å. [11] For the gamma and beta phases no significant change in lattice parameters is found.

No neutron diffraction phase data is available for γ-NiOOH from existing literature, only XRD phase data files are at hand, where the H atom is missing. As reference material pure γ-NiOOH can be oxidized chemically from $Ni(OH)_2$ in a 8 M KOH solution with as oxidizing reagent 12% sodium hypochlorite.[11] The neutron diffraction pattern resulting from this reference material can be used to identify all γ-NiOOH peaks in the sample.

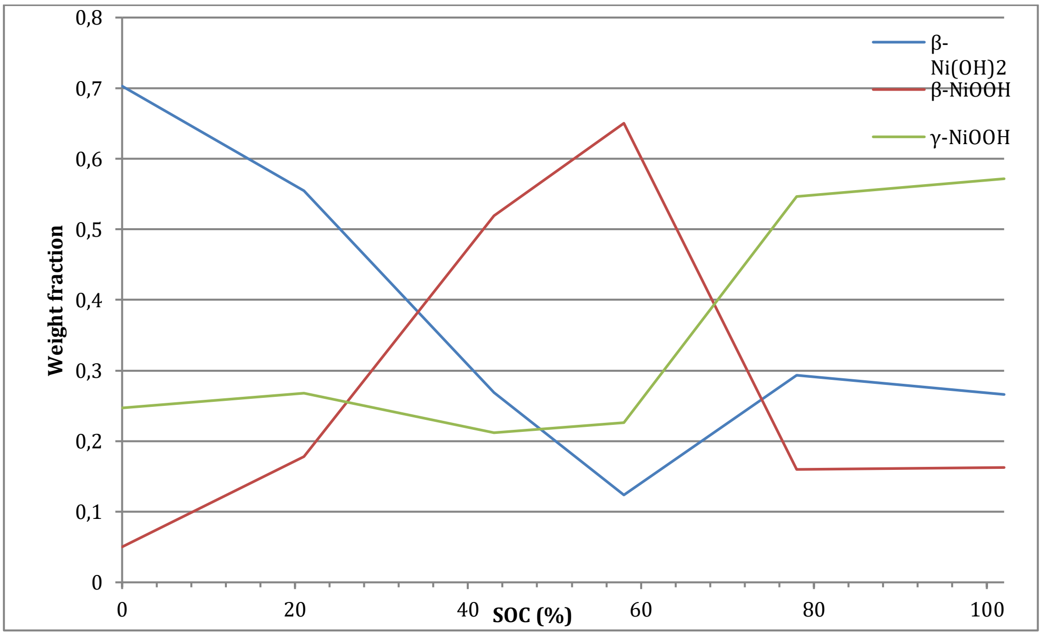

Figure 41. Weight fraction (without carbon) of the nickel(oxy)hydroxide phases with increasing state of charge (deducted from the Rietveld refinement on the neutron diffraction patterns)

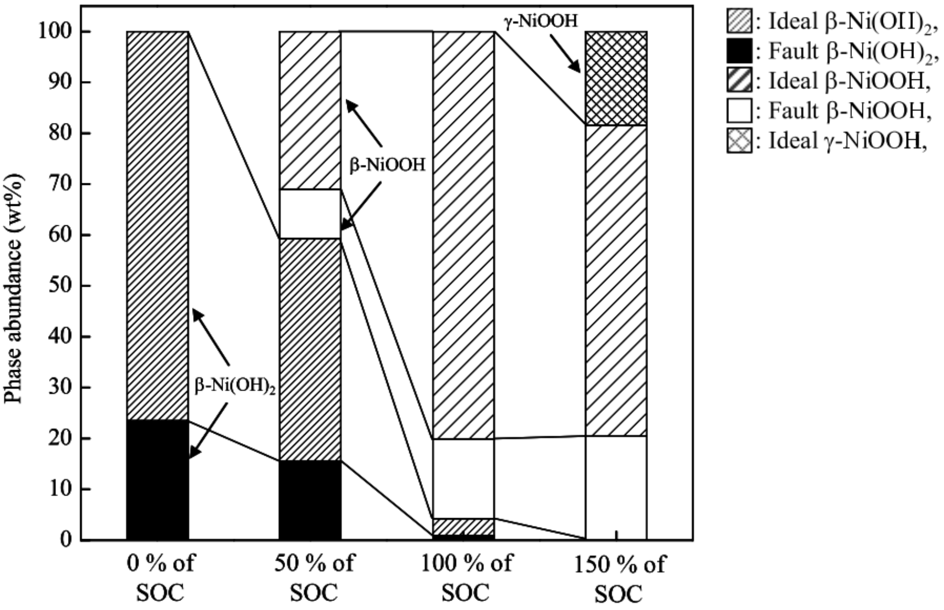

Figure 42. phase abundance for nickel(oxy)hydroxide samples at varied SOC.[11]

The XRD results vary significantly with ND. A small part of the sample is taken out and placed in the sample holder for the XRD measurements, also XRD is a surface technique, there for a smaller part of the sample is examined and thus can give different results. The higher percentage of carbon in XRD can be explained this way. Next to that, the carbon probably had a smaller particle size and as a consequence fitted better in the grooves of the sample holder. For this reason the carbon is left out in the weight fraction plot below. This gives a more accurate picture of the changes within the nickel(oxy)hydroxide phases. Just as with the ND results has the β-$Ni(OH)_2$ phase the largest fraction at 0% and the fraction decreases slowly with increasing SOC. At 58% of SOC the weight fraction jumps up towards 78_{wt}%, this is in contrast to the ND weight fraction where β-$Ni(OH)_2$ contains 12_{wt}%. If the XRD and ND graphs of nickel samples at 58% of SOC are taken from the appendix (Figure 54 and Figure 55 respectively). It can be clearly seen that the Rietveld refinement is in a mismatch with the measurement and some peaks from the refinement don't appear in the measurement. γ-NiOOH is steadily increasing with increasing SOC (if the 58% of SOC datapoint is dismissed, which can be done because of the error in the refinement).

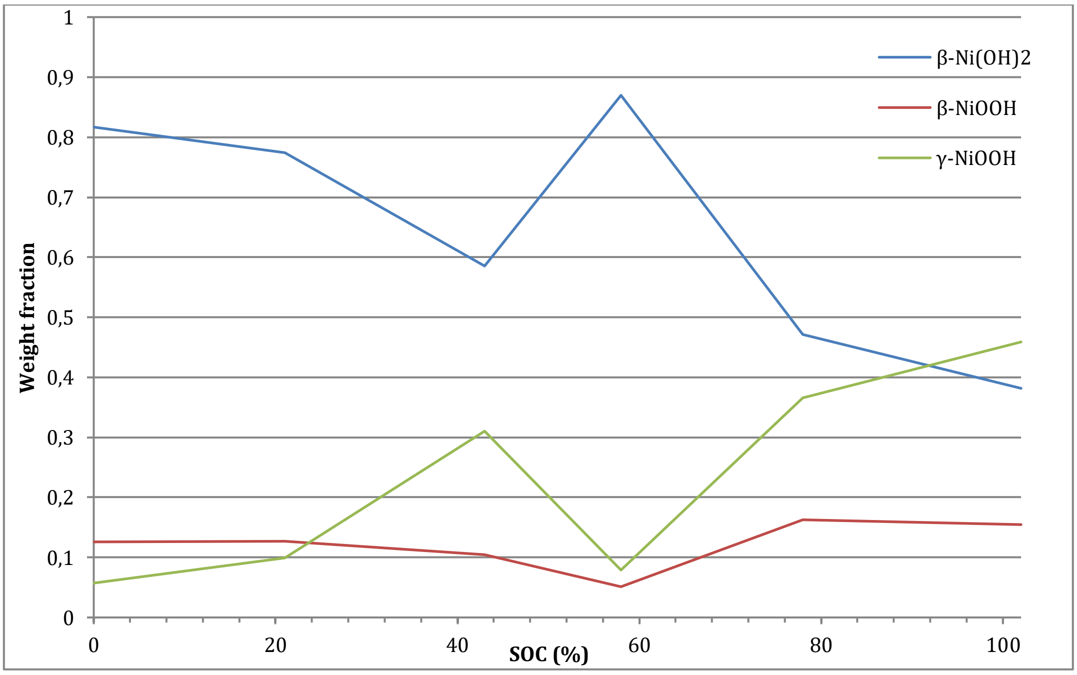

Figure 43. Weight fraction (without carbon) of the nickel(oxy)hydroxide phases with increasing state of charge (deducted from the Rietveld refinement on the X-ray diffraction patterns)

The hydrogen fraction of the nickel(oxy)hydroxide phases is varied to see the effect of this change. The refinement is a little better, but it's a minor improvement, so this is not further elaborated. The scattering process of the neutron diffraction with hydrogen is largely incoherent, so the height of the background gives an indication of the hydrogen content. The background function that's used is Chebyschev with six background coefficients. The first background coefficient is plotted to give an indication of the background height (Figure 44). The first background coefficient decreases from 4.12 to 2.19, which is a decrease of 47%. This decrease of background can be attributed to the decrease of hydrogen in the electrode.

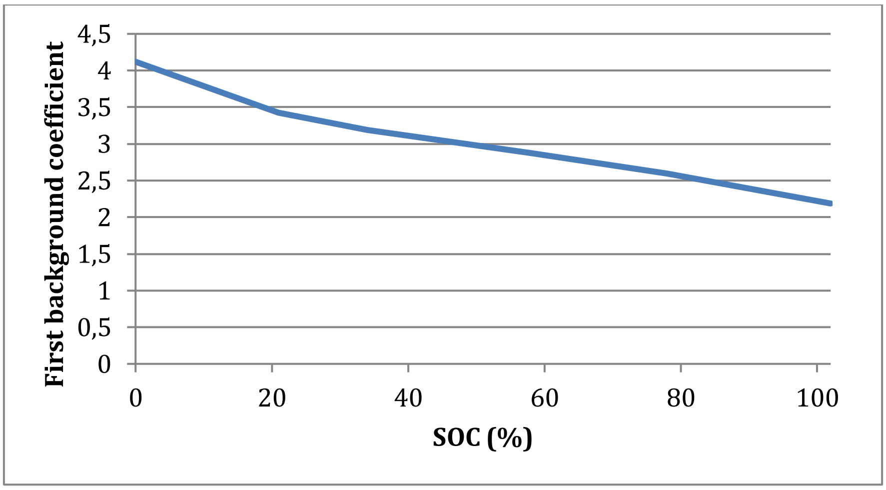

Figure 44. The first background coefficient (chebyschev function) of the rietveld refinement on the nickel neutron diffraction patterns

The nickel electrodes are charged before the sample is taken out and analysed, so the direct reduction of β-NiOOH and γ-NiOOH into β-Ni$(OH)_2$ cannot be verified with these experiments. Additional discharge experiments need to be performed to verify this. There is no intentional or accidental iron powder found in the nickel electrodes. Literature suggests that iron incorporation might further increase the efficiency of the electrode.

4.2 IRON ELECTRODES

4.2.1 BATTERY POWDER FROM THE SHELF

From the SEM, XRD and ND results three phases are identified, namely iron (Fe), goethite (FeOOH) and magnetite (Fe_3O_4). In the analysis the carbon content is too small and can be neglected. For the neutron diffraction analysis all peaks are represented in the Rietveld refinement, resulting in a good fit.

4.2.2 X-RAY AND NEUTRON DIFFRACTION AT VARIED CHARGE STATES

The Rietveld refinement is performed simultaneously on the ND and XRD pattern, but the phase fraction, size and strain are calculated separately. The particle size is not refined because the iron(hydroxide) phases went to 1 nm, this is too small to take seriously. The weight fraction of Fe is higher overall for the ND refinements compared to XRD, in contrast the FeOOH content is higher overall in the XRD measurements. But the tendencies in the graphs do compare pretty well. The weight fraction of Fe increases and FeOOH decreases with increasing state of charge. The increase of Fe is according to the first discharge plateau. The samples from 39% - 90% demonstrate a lower Fe_3O_4 weight fraction, these samples are better activated. In contrast the second sample (20%) has more Fe_3O_4 which indicates it is not activated properly. The graph also visualizes that the $Fe(OH)_2$ content is very low for any of these samples. A strange phenomena, where $Fe(OH)_2$ is expected, FeOOH is found. An explanation might be found in Figure 45 and the following reaction:

$$Fe(OH)_2 + OH^- \leftrightarrow FeOOH + H_2O + e^-$$
$$E^o = -0{,}56\, V\ vs\ SHE$$

In combination with

$$H_2O + e^- \rightarrow \tfrac{1}{2}H_2 + OH^-$$
$$E^o = 0\, V\ vs\ SHE \text{ at PH } 1$$

Gives

$$Fe(OH)_2 \rightarrow FeOOH + \tfrac{1}{2}H_2$$
$$E^o = -0{,}56\, V$$

The iron electrodes are discharged until 1.1 V vs open circuit voltage. Probably, this is too low and the second discharge reaction has already transformed all the $Fe(OH)_2$ into FeOOH. To explain why there is no $Fe(OH)_2$ when charging, this might have to do with kinetics. During charge the $Fe(OH)_2$ is transformed into Fe faster than FeOOH can produce it.
To get a more detailed picture, a reference electrode can be placed next time and the discharging can be stopped before the deep discharge occurs.

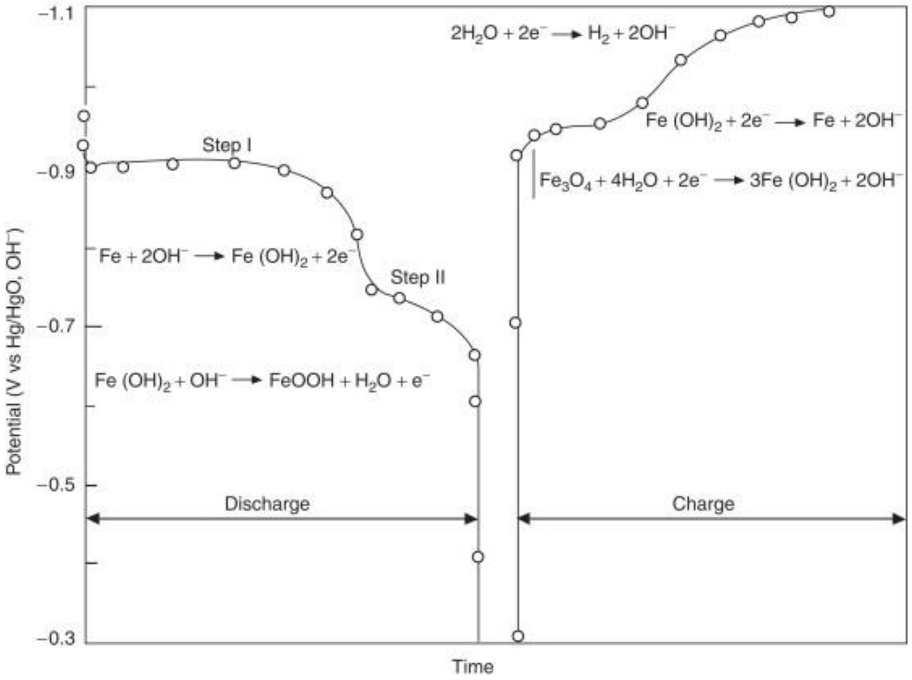

Figure 45. Discharge/charge curve of iron electrode in 6 M KOH [24]

Magnetite (Fe_3O_4) and maghemite (γ-Fe_2O_3) have the same crystal structure and spacegroup. They also have nearly identical XRD spectra. [14] published The peaks identified as magnetite, might also be maghemite. To find out the Fe_3O_4 was replaced by Fe_2O_3 in the Rietveld refinement. The refinement on the XRD spectra where indeed quite close, but the refinement on the ND pattern did not match. The Fe_3O_4 gave a much better fit, so the peaks identified as magnetite still holds.

Here again the first background coefficient of the neutron diffraction pattern is plotted (Figure 46) to give an indication of the hydrogen decrease. Please consider this to be a very rough estimation. The first background coefficient drops from 3.329 to 0.9453, this is a significant 72% decrease. This background drop can be attributed to the hydrogen decrease in the material.

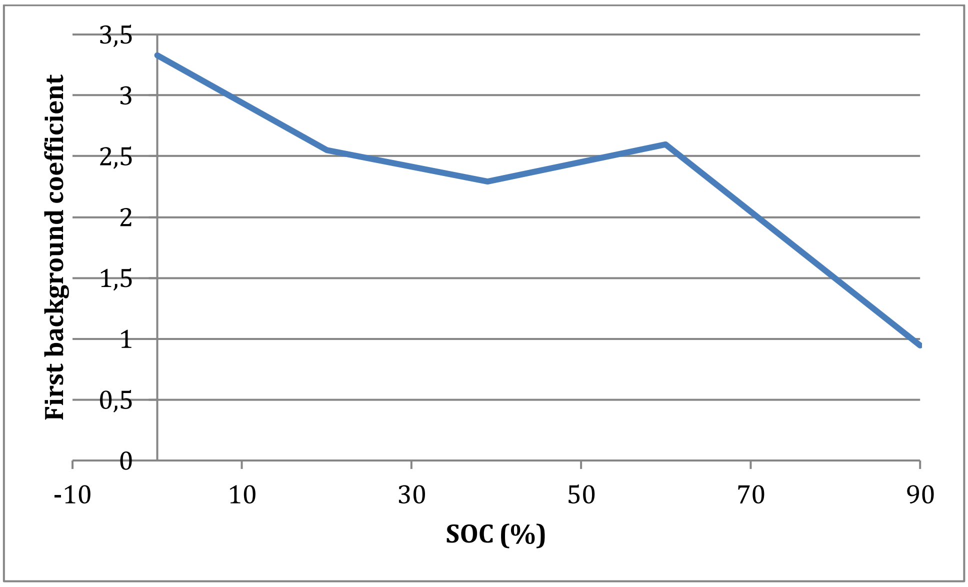

Figure 46. The first background coefficient (chebyschev function) of the rietveld refinement on the iron neutron diffraction patterns.

Great differences in the weight of the Fe samples are found, a sixth sample was left out because of the low powder content (0.26 g instead of 5.5 g on average). Probably most of it was lost from the sides of the pockets during the activation period, the charge capacity was dropping with every charge/discharge cycle. It is recommended to seal the pockets completely, so the iron powder is better contained.

4.3 PRELIMINARY EXPERIMENTS FOR IN-SITU TEST SETUP

For neutron diffraction the thinnest quartz glass will give the least background noise, but it is important that the glass can withstand the pressure difference when placed in vacuum during the neutron diffraction measurements. The KOH solution contained in the quartz glass can damage the diffractometer. If the glass breaks due to the pressure the KOH solution will contaminate the diffractometer. That’s why these measurements where performed without a vacuum. Unfortunately, there were two instances where the glass slided from the cap, even without a vacuum. This was probably because the KOH solution wetted the surface where the glass touches the cap. There for is important to make sure this surface is dry, otherwise use a different cap.

The size of the nickel foam current collector does not give significant differences between the spectra. Here the biggest size will put the most material in the neutron beam. It is of importance that the H_2 bubbles will flow up and leave the cell and won’t block the ion diffusion. That’s why there still needs to be enough space between the current collector and the quartz glass tube. For the neutron diffraction experiments you want as little KOH solution as possible in the beam (due to background noise), so here an optimum needs to be found.

In Figure 17 is an initial schematic drawing shown of an in-situ neutron diffraction test setup. Here the working electrode can be placed in the neutron beam. A counter electrode is bigger than the working electrode so the counter electrode wil not limit the reaction. There is a connection between the two electrodes, maybe this connection can be made over the whole length of the tube, neutron diffraction measurements need to clarify if this wil not give too much background noise. A reference electrode can be placed to get accurate voltage measurements. What is missing in the drawing is a gas outlet, so the hydrogen and oxygen gas can leave the cell. It would be nice to measure the hydrogen and oxygen gas with a gas analyser, so the real-time gas production will be known.

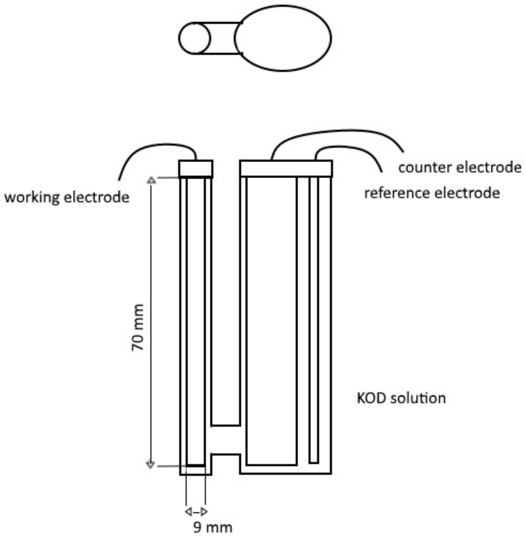

Figure 47. Schematic drawing of a proposed experimental setup

5 CONCLUSIONS

In the nickel electrode are next to the carbon, 3 phases present, namely nickel hydroxide (β-$Ni(OH)_2$) and two nickel oxy hydroxides (β-NiOOH and γ-NiOOH). The Rietveld refinement on the Ni samples with a varied SOC was successful with these compounds. In the comparison with Morishita et al. significant differences are found. The transition towards β-NiOOH and subsequently γ-NiOOH occurs faster. Already at 50% of SOC the weight fraction of β-NiOOH is 58 $_{wt}$% and at 100% of SOC the γ-NiOOH is 57 $_{wt}$%. The c-parameter of γ-NiOOH is in agreement with Morishita et al. with a lattice distance of 20.8 Å. A more precise SOC estimation with the Kalman filter can make the comparison more accurate. As reference material pure γ-NiOOH can be oxidized chemically from $Ni(OH)_2$ in a 8 M KOH solution with as oxidizing reagent 12% sodium hypochlorite. For the XRD measurements it is important that all compounds are equally distributed in the sample holder. In the iron electrode three phases are identified, namely iron (Fe), goethite (FeOOH) and magnetite (Fe_3O_4). Where $Fe(OH)_2$ is expected, FeOOH is found, this is because the second discharge reaction was already taken place. Next time a reference electrode can be used to give an accurate view of the voltage. The weight fraction of Fe increases and FeOOH decreases with increasing state of charge. Better activated samples demonstrate a lower Fe_3O_4 weight fraction. Maghemite (γ-Fe_2O_3) was taken into consideration in stead of Fe_3O_4, but this proved to be not the case. The weight fraction of Fe is higher overall for the ND refinements compared to XRD, in contrast the FeOOH content is higher overall in the XRD measurements. The hydrogen content is decreasing with increasing SOC proportional to background function both for the nickel and iron electrode. At last it is important to seal the pockets completely, so the iron powder is better contained. For the in-situ neutron diffraction test setup the thinnest quartz glass will give the least background noise. The largest diameter nickel foam current collector, gives as much background noise as the smaller versions do. So the 0.4 mm quartz glass and 4 mm nickel foam current collector will give the best neutron diffraction results.

6 REFERENCES

[1] F. M. Mulder, B. M. H. Weninger, J. Middelkoop, F. G. B. Ooms, and H. Schreuders, “Efficient electricity storage with a battolyser, an integrated Ni–Fe battery and electrolyser,” *Energy Environ. Sci.*, vol. 10, no. 3, pp. 756–764, 2017.

[2] K. Vijayamohanan, T. S. Balasubramanian, and A. K. Shukla, “Rechargeable alkaline iron electrodes,” *J. Power Sources*, vol. 34, no. 3, pp. 269–285, 1991.

[3] P. Tsai and S. L. I. Chan, *Nickel-based batteries: materials and chemistry*, no. March 1899. Woodhead Publishing Limited, 2013.

[4] A. K. Shukla, S. Venugopalan, and B. Hariprakash, “Nickel-based rechargeable batteries,” vol. 100, pp. 125–148, 2001.

[5] R. A. Huggins, *Advanced Batteries: Material Science Aspects*. Springer Science, Business media, 2009.

[6] F. Barde, M. R. Palacin, Y. Chabre, O. Isnard, and J. Tarascon, “In Situ Neutron Powder Diffraction of a Nickel Hydroxide Electrode,” pp. 3936–3948, 2004.

[7] Y. Sato, S. Takeuchi, and K. Kobayakawa, “Cause of the memory effect observed in alkaline secondary batteries using nickel electrode,” *J. Power Sources*, vol. 93, no. 1–2, pp. 20–24, 2001.

[8] Y. Sato, “SECONDARY BATTERIES – NICKEL SYSTEMS |Memory Effect,” in *Reference Module in Chemistry, Molecular Sciences and Chemical Engineering*, no. 2000, 2009, pp. 534–549.

[9] H. Huang, Y. Guo, and Y. Cheng, “Ultrastable α phase nickel hydroxide as energy storage materials for alkaline secondary batteries,” *Appl. Surf. Sci.*

[10] A. B. Separators and M. Effect, “SECONDARY BATTERIES – NICKEL SYSTEMS Electrodes : Nickel,” pp. 404–411, 2009.

[11] M. MORISHITA, S. OCHIAI, T. KAKEYA, M. W. Tetsuya OZAKI, Yoshiteru KAWABE, S. TANASE, and and T. SAKAI, “Phase Transformation in the Charge-Discharge Process and the Structural Analysis by Synchrotron XAFS and XRD for Nickel Hydroxide Electrode,” *electrochemistry*, vol. 76, no. 11, pp. 802–807, 2008.

[12] C. Delmas, “Stacking faults in the structure of nickel hydroxide: a rationaleof its high electrochemical activity,” *J. Mater. Chem.*, vol. 7, no. 8, pp. 1439–1443, 1997.

[13] L. Trotochaud, S. L. Young, J. K. Ranney, and S. W. Boettcher, “Nickel − Iron Oxyhydroxide Oxygen-Evolution Electrocatalysts : The Role of Intentional and Incidental Iron Incorporation,” 2014.

[14] D. C. Lee, D. Lei, and G. Yushin, “Morphology and Phase Changes in Iron Anodes Affecting their Capacity and Stability in Rechargeable Alkaline Batteries,” *ACS Energy Lett.*, vol. 3, no. 4, pp. 794–801, 2018.

[15] L. Ojefors, “Temperature Dependence of Iron and Cadmium Alkaline Electrodes,” vol. 123, no. 8, pp. 39–43, 1973.

[16] M. Pourbaix, *Atlas of electrochemical equilibria in aqueous solutions*, 2nd ed. National Association of Corrosion Engineers, 1974.

[17] C. Chakkaravarthy, “The nickel / Iron battery,” vol. 35, pp. 21–35, 1991.

[18] B. M. H. Weninger, “The Battolyzer: Combined short- and long-term energy storage,” TU Delft, 2016.

[19] A. K. Shukla, M. K. Ravikumar, and T. S. Balasubramanian, “Nickel / iron batteries,” *J. Power Sources*, vol. 51, pp. 29–36, 1994.

[20] A. Aguadero and L. Daza, “Neutron powder diffraction as a characterization tool of solid oxide fuel cell materials,” vol. 36, pp. 134–150, 2007.

[21] R. Pynn, *Neutron Scattering, a primer*. 1990.

[22] B. L. Dutrow and C. M. Clark, “X-ray Powder Diffraction (XRD),” *Geochemical Instrumentation and Analysis*. [Online]. Available: https://serc.carleton.edu/research_education/geochemsheets/techniques/XRD.html. [Accessed: 09-Jul-2017].

[23] W. Bouwman, “Diffraction from crystalline materials,” in *neutrons, x-rays and positrons*, 2017.

[24] G. P. Stahly, “Advantages of a Cu vs. Co X-ray Diffraction Source,” *http://www.tricliniclabs.com/downloadable-documents/Advantages%20of%20a%20Cu%20vs.%20Co%20X-ray%20Diffraction%20Source%20-%20Stahly%20-%20Triclinic%20Labs%20-Q32012.pdf*. p. 1, 2012.

[25] P. Jensen, L. Udby, and B. Lebech, “Diffraction from crystals,” *e-neutrons wiki*, 2017. .

[26] D. L. Bish and J. E. Post, *Modern powder diffraction*. Washington, D.C. : Mineralogical Society of America, 1989.

[27] B. H. Toby and R. B. Von Dreele, “GSAS-II: the genesis of a modern open-source all purpose crystallography software package,” *J. Appl. Crystallogr.*, vol. 46, no. 2, pp. 544–549, 2013.

[28] B. Vadlamani, K. An, M. Jagannathan, K. S. R. Chandran, and O. Ridge, “An In-Situ Electrochemical Cell for Neutron Diffraction Studies of Phase Transitions in Small Volume Electrodes of Li-Ion Batteries,” vol. 161, no. 10, pp. 28–30, 2014.

[29] V. Y. Kazimirov *et al.*, “Atomic structure and lattice dynamics of Ni and Mg hydroxides,” *Solid State Ionics*, vol. 181, no. 39–40, pp. 1764–1770, Dec. 2010.

[30] Z. S. Basinski, W. Hume-Rothery, and A. L. Sutton, “The Lattice Expansion of Iron,” *Proc. R. Soc. A Math. Phys. Eng. Sci.*, vol. 229, no. 1179, pp. 459–467, 1955.

[31] A. W. Hull, “The crystal structure of iron,” *J. Franklin Inst.*, vol. 184, no. 3, pp. 447–448, 1917.

[32] F. Bosi, U. Hålenius, and H. Skogby, “Crystal chemistry of the magnetite-ulvöspinel series,” *Am. Mineral.*, vol. 94, no. 1, pp. 181–189, 2009.

[33] E. Zepeda-Alarcon *et al.*, “Magnetic and nuclear structure of goethite (α-FeOOH): A neutron diffraction study,” *J. Appl. Crystallogr.*, vol. 47, no. 6, pp. 1983–1991, 2014.

[34] A. E. Westgren, A.;Lindh, “Krystallstruktur von Eisen und Stahl,” *Zeitschrift fuer Phys. Chemie*, vol. 98, pp. 181–210, 1921.

[35] R. G. W. Wyckoff, “Crystal Structures,” *rystal Struct. 2nd ed.; John Wiley Sons New York, NY, USA, 1963; Vol. 4, pp. 400–401*, pp. 400–401, 1963.

[36] S. M. Rezvanizaniani, Z. Liu, Y. Chen, and J. Lee, “Review and recent advances in battery health monitoring and prognostics technologies for electric vehicle (EV) safety and mobility,” *J. Power Sources*, vol. 256, pp. 110–124, 2014.

[37] Woodbank Communications, “State of Charge (SOC) Determination,” *Electropaedia*, 2017. [Online]. Available: https://www.mpoweruk.com/soc.htm. [Accessed: 03-Jul-2018].

7 LIST OF FIGURES

8 LIST OF TABLES

APPENDIX A

A1 XRD AND ND GRAPHS OF NICKEL SAMPLES AT VARIED STATES OF CHARGE

Below are the X-ray and neutron diffraction patterns displayed of the nickel samples in sequence with increasing SOC. Each samples is indicated with its SOC, for example 'ni 0%' is a nickel sample with a SOC of 0%. The blue dotted pattern is the diffraction measurement, the green pattern the Rietveld refinement model and the red line the background function. The error function is displayed as the black and turquoise pattern and in the legend the different phases corresponding to the colored stripes are found.

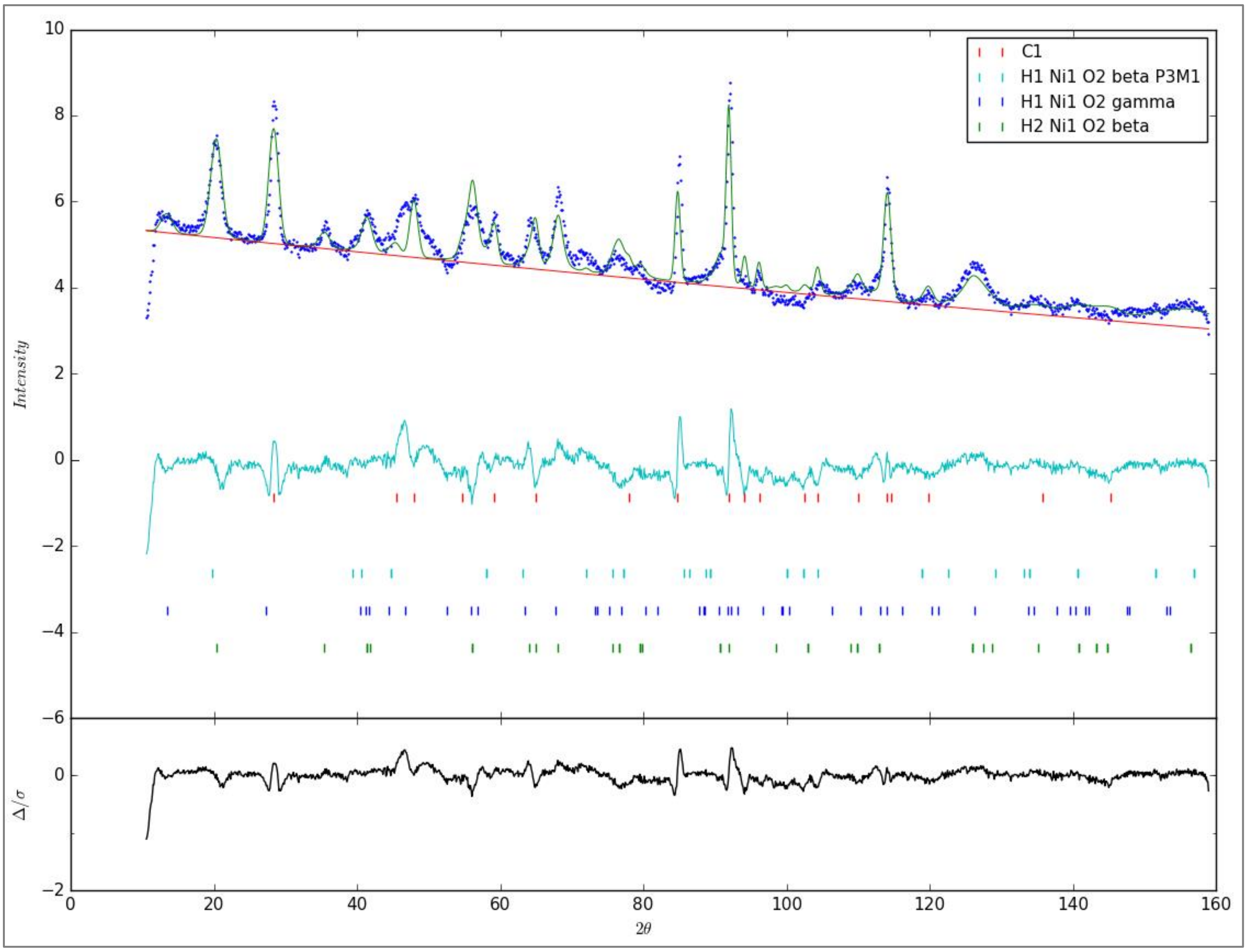

Figure 48. Rietveld refinement on neutron diffraction pattern of ni 0%

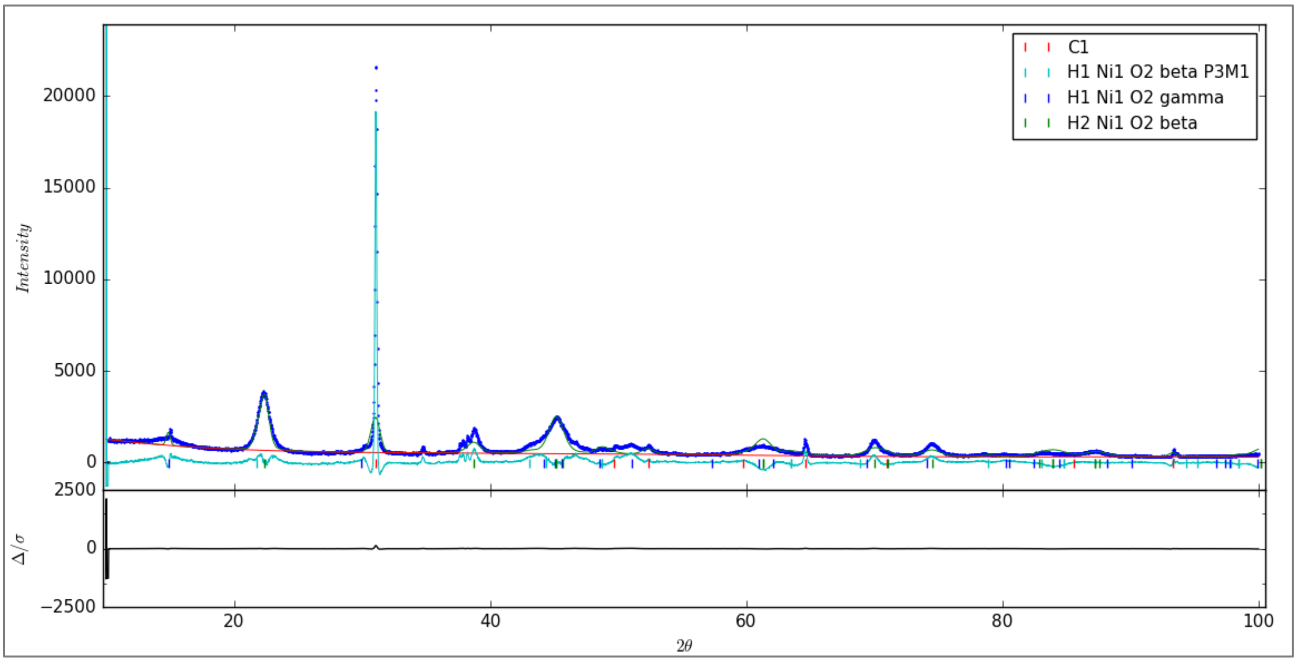

Figure 49. Rietveld refinement on X-ray diffraction pattern of ni 0%

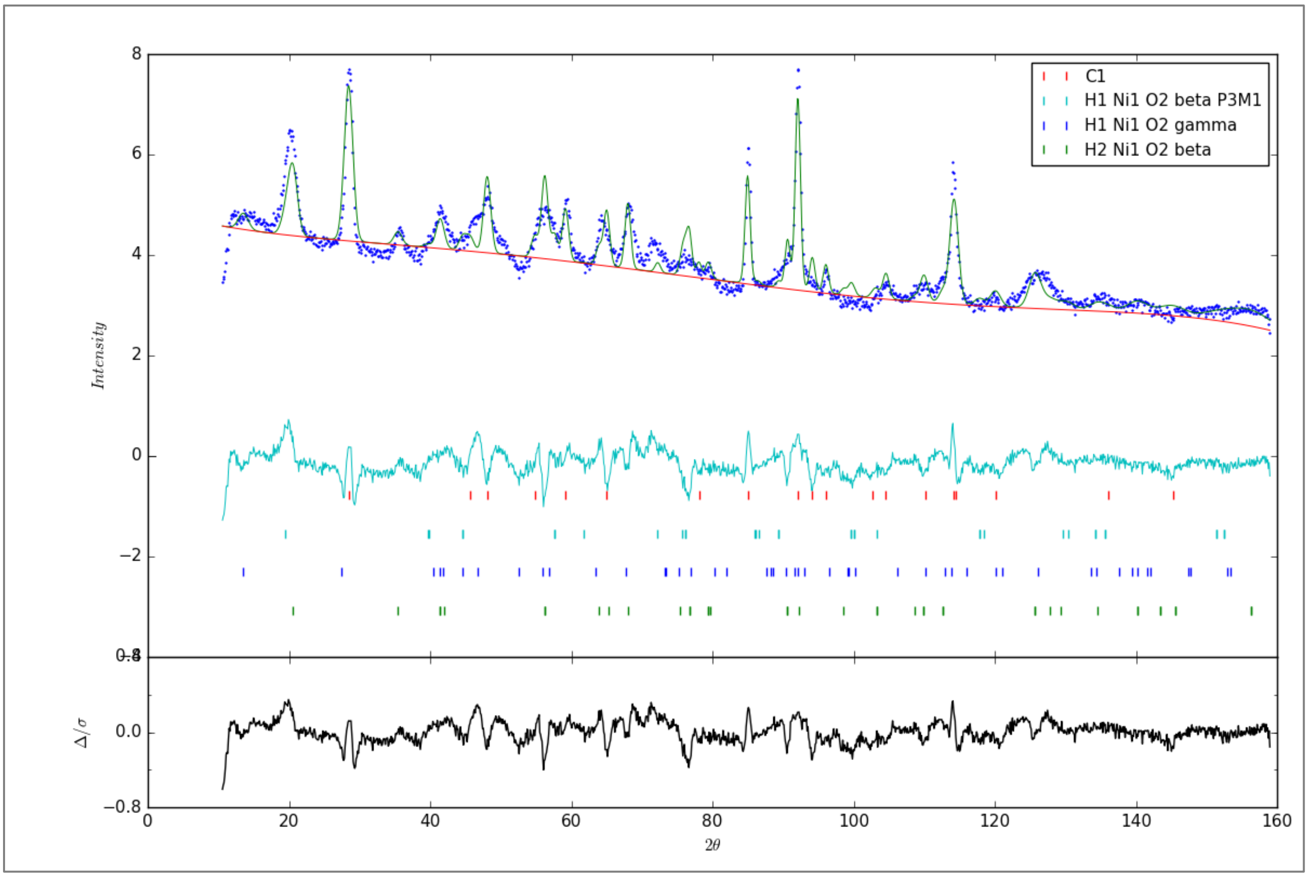

Figure 50. Rietveld refinement on neutron diffraction pattern of ni 21%

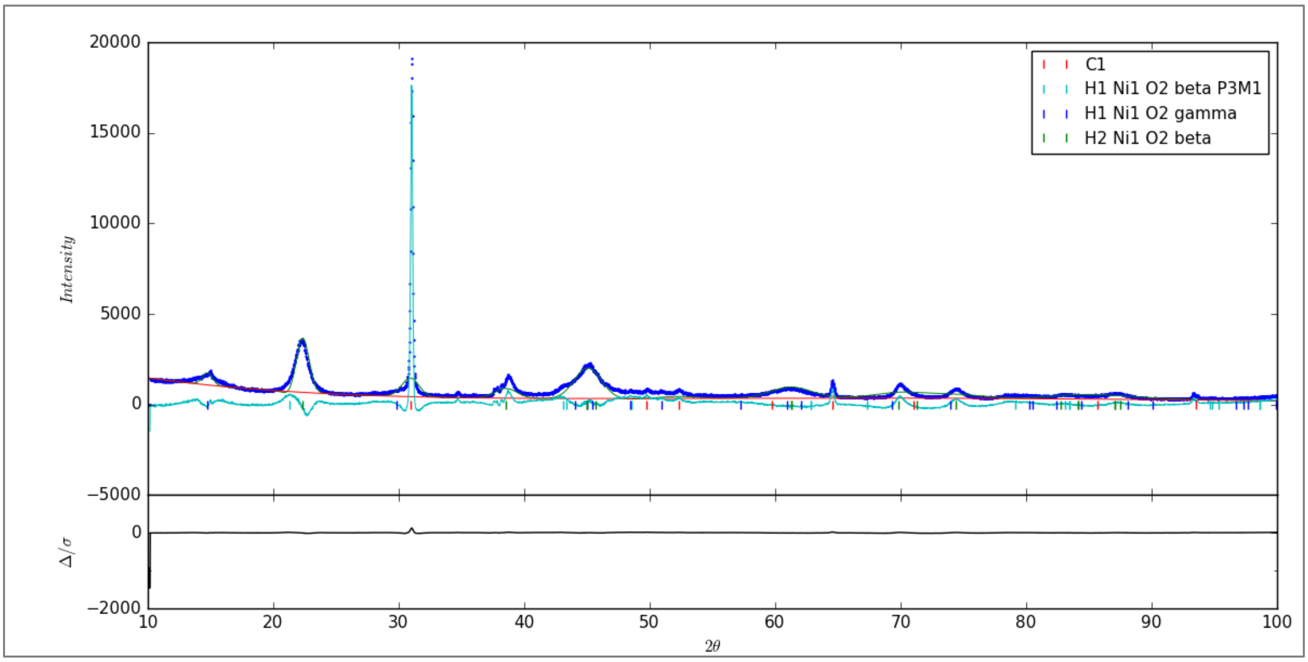

Figure 51. Rietveld refinement on X-ray diffraction pattern of ni 21%

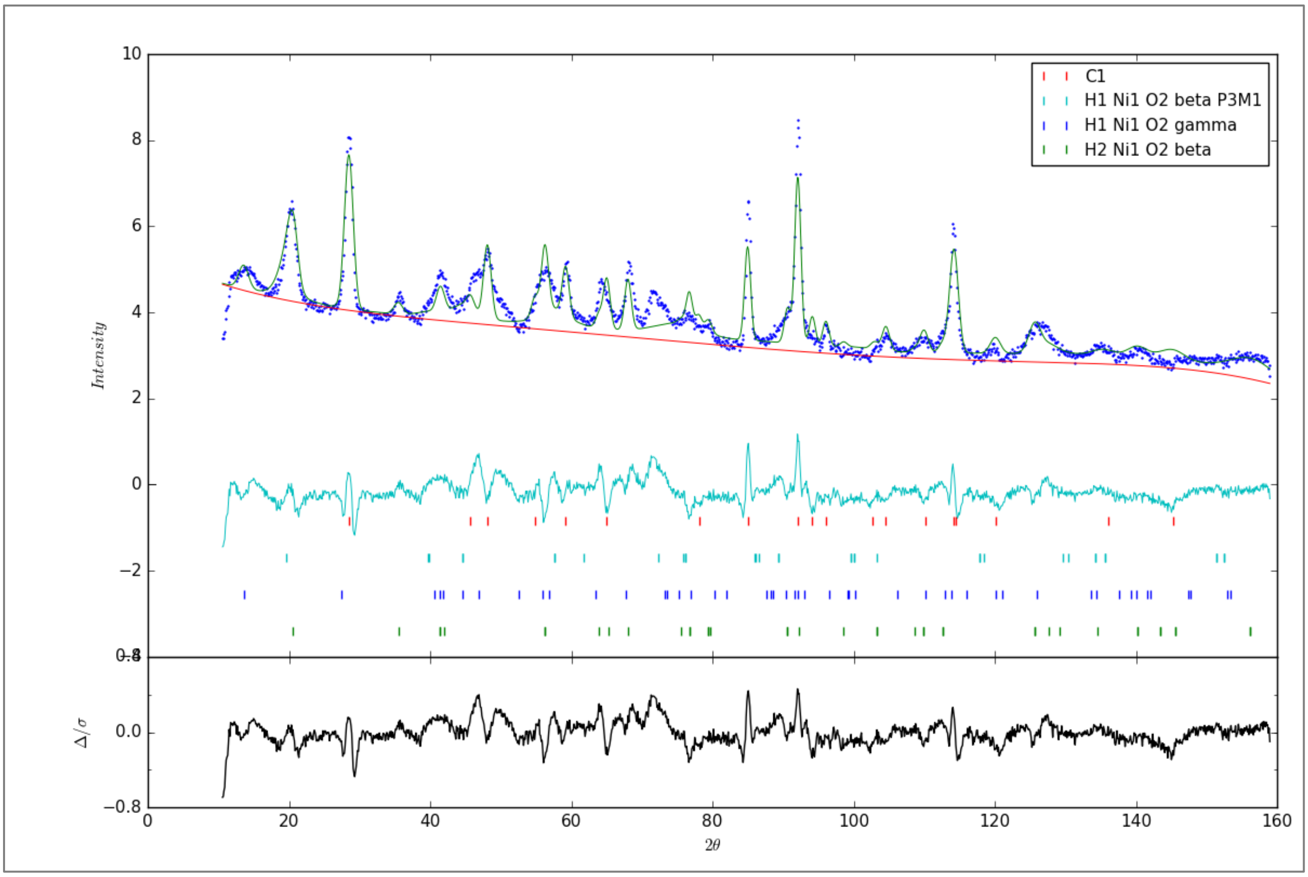

Figure 52. Rietveld refinement on neutron diffraction pattern of ni 43%

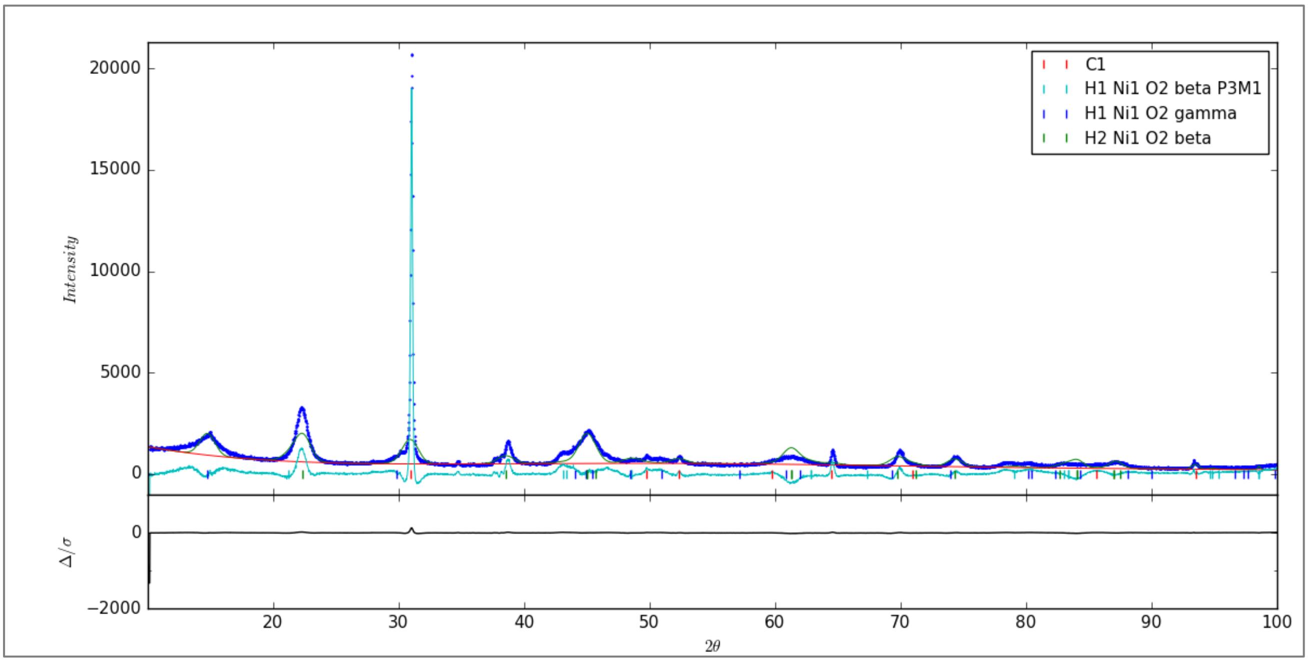

Figure 53. Rietveld refinement on X-ray diffraction pattern of ni 43%

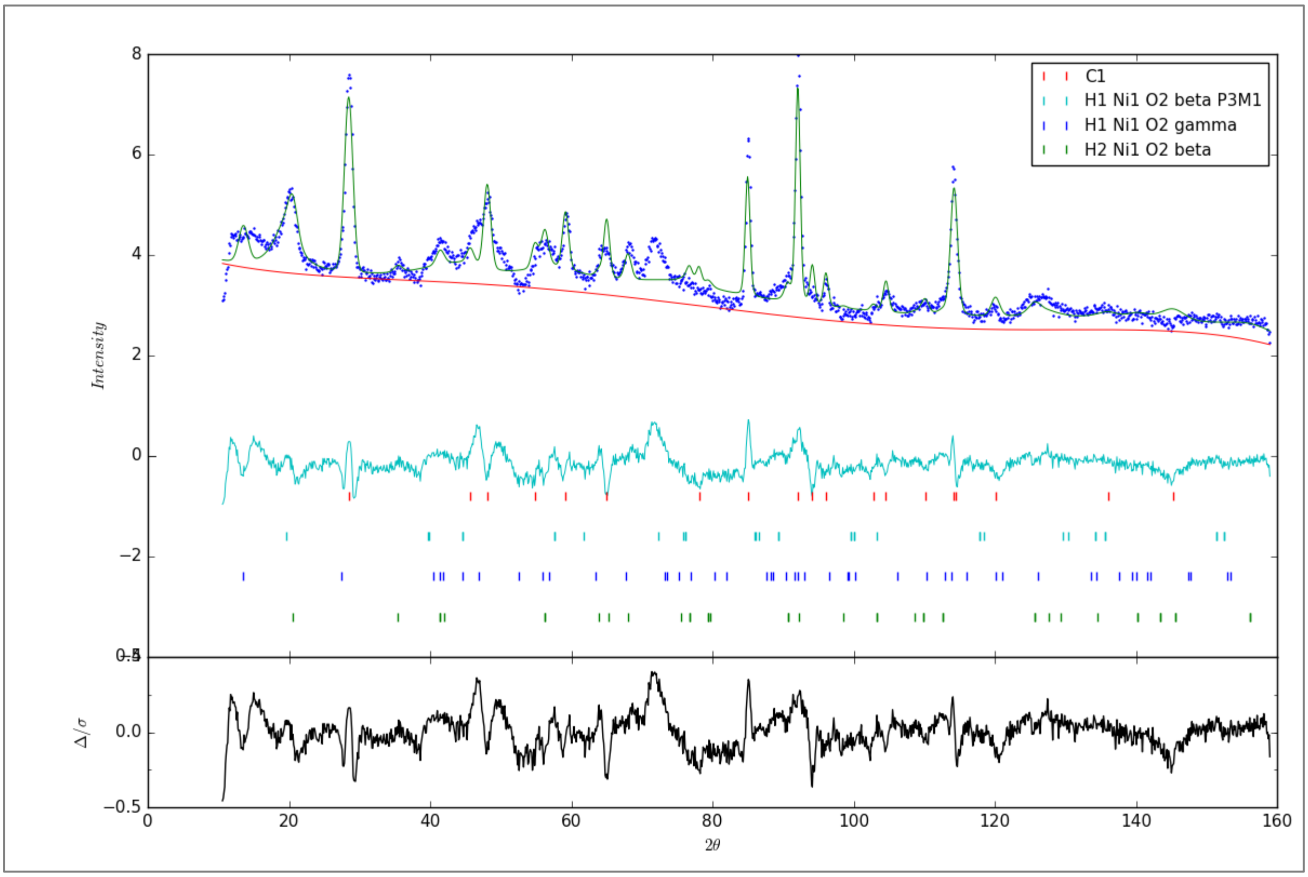

Figure 54. Rietveld refinement on neutron diffraction pattern of ni 58%

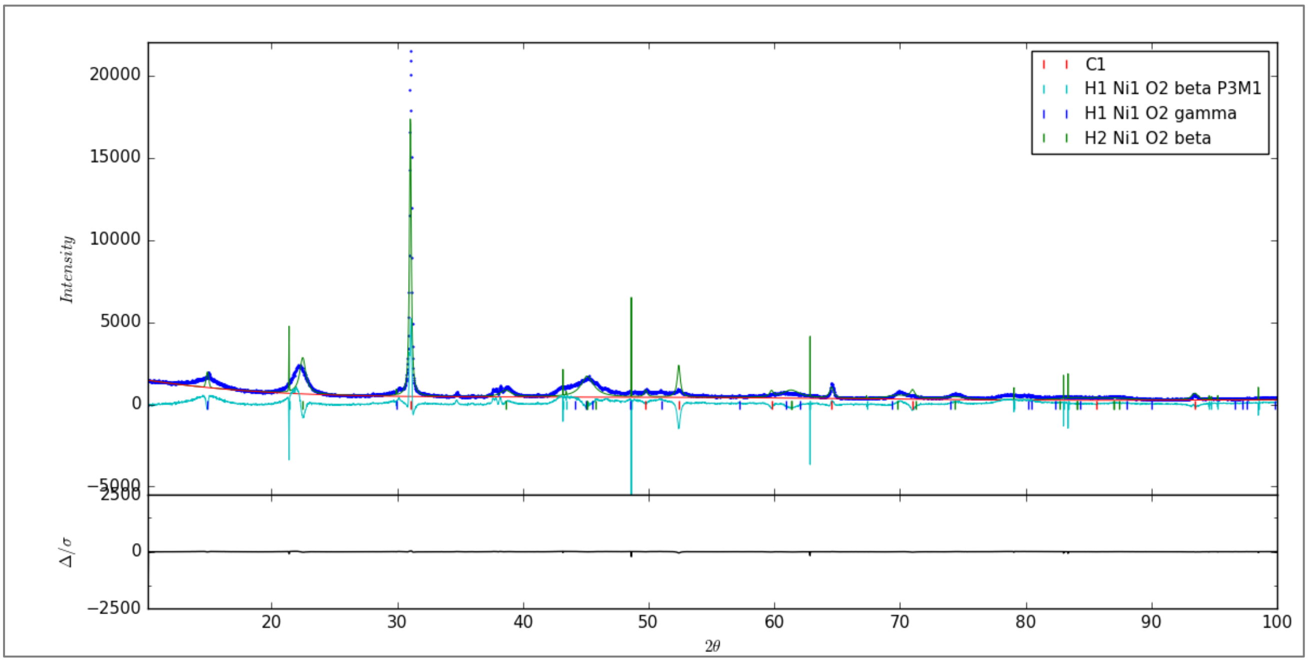

Figure 55. Rietveld refinement on X-ray diffraction pattern of ni 58%

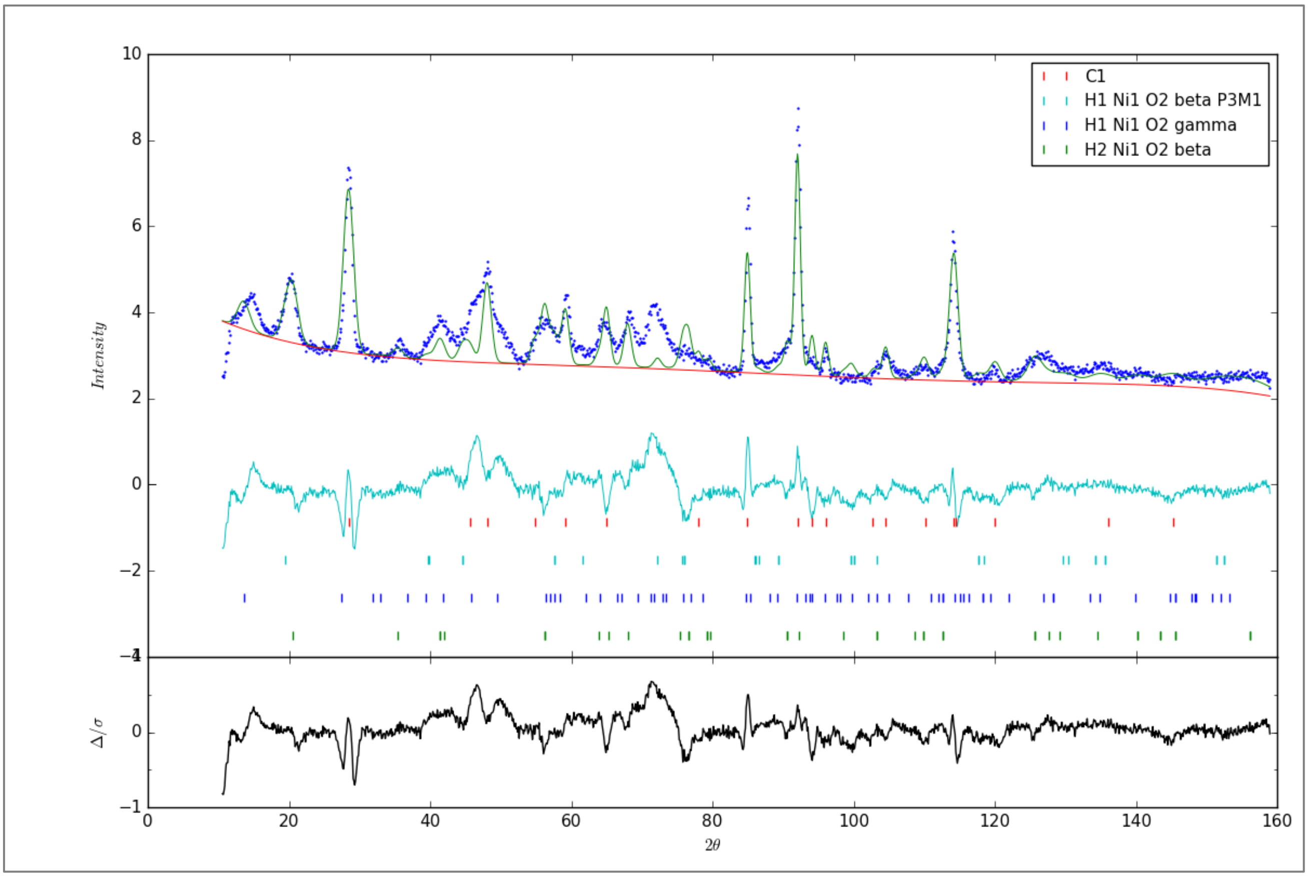

Figure 56. Rietveld refinement on neutron diffraction pattern of ni 78%

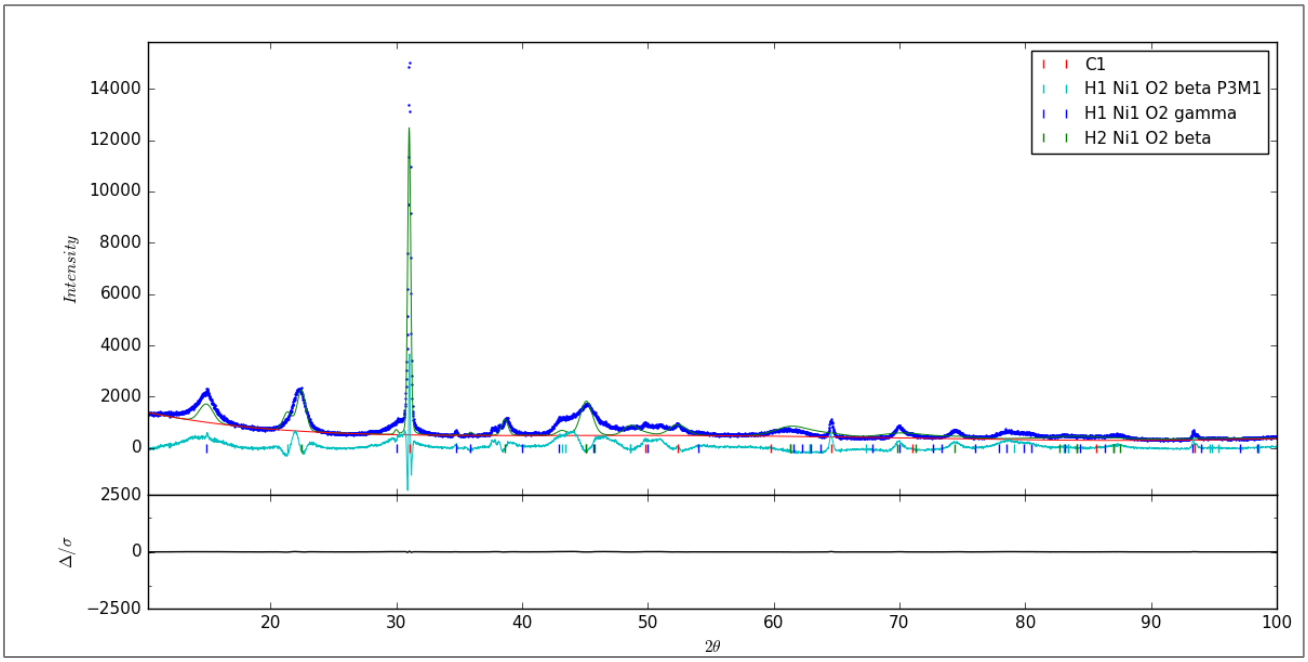

Figure 57. Rietveld refinement on X-ray diffraction pattern of ni 78%

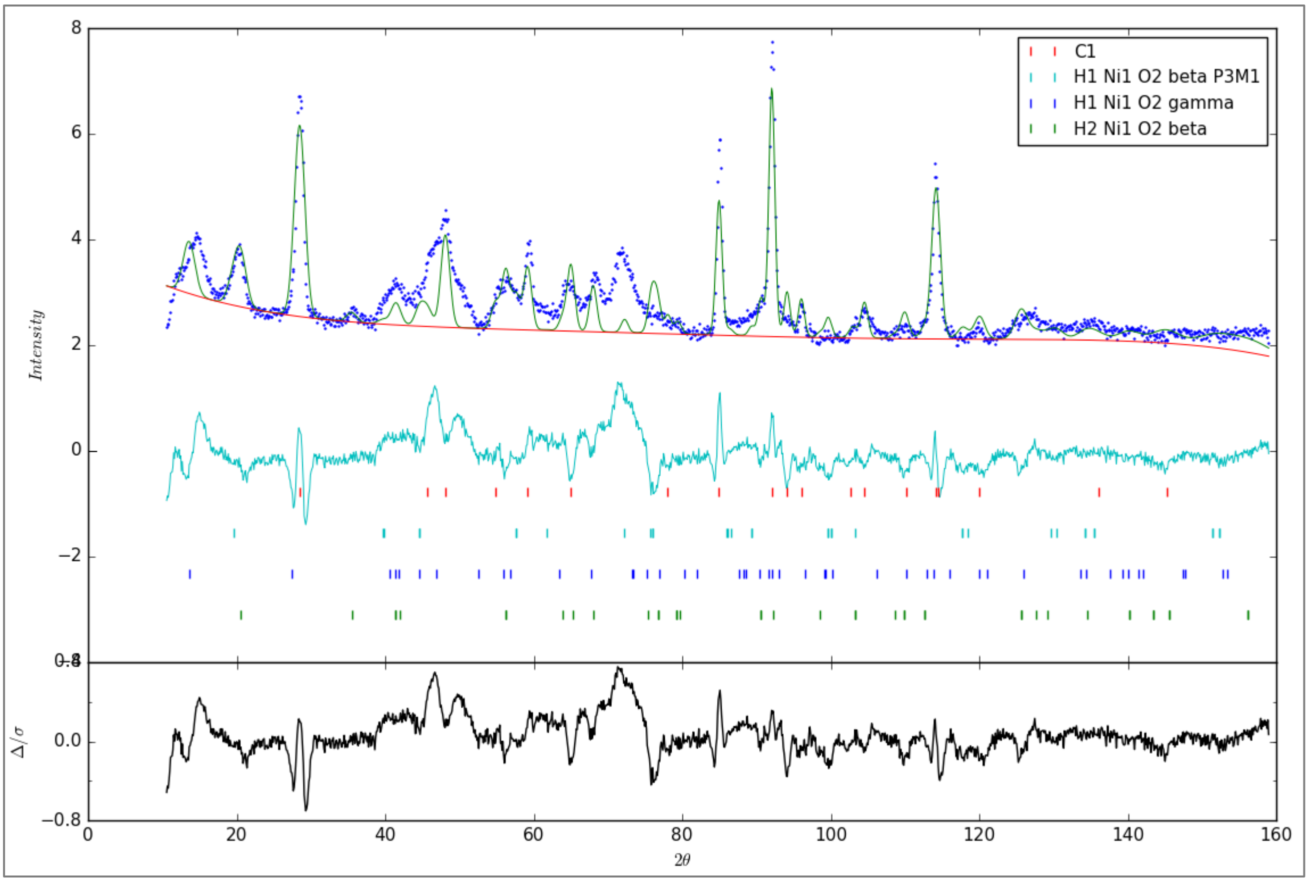

Figure 58. Rietveld refinement on neutron diffraction pattern of ni 102%

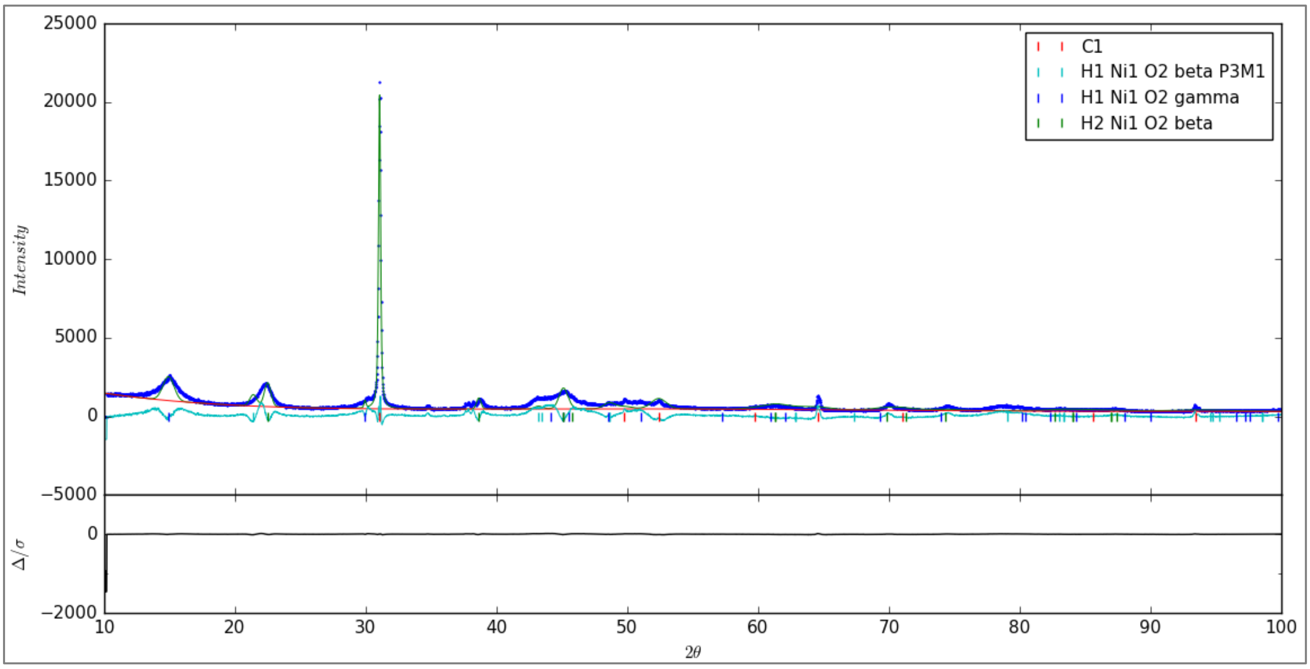

Figure 59. Rietveld refinement on X-ray diffraction pattern of ni 102%

A2 XRD AND ND GRAPHS OF IRON SAMPLES AT VARIED STATES OF CHARGE

Below are the X-ray and neutron diffraction patterns displayed of the iron samples in sequence with increasing SOC. Each samples is indicated with its SOC, for example 'Fe 0%' is an iron sample with a SOC of 0%. The blue dotted pattern is the diffraction measurement, the green pattern is the Rietveld refinement model and the red line is the background function. The error function is displayed as the black and turquoise pattern and in the legend the different phases corresponding to the colored stripes are found.

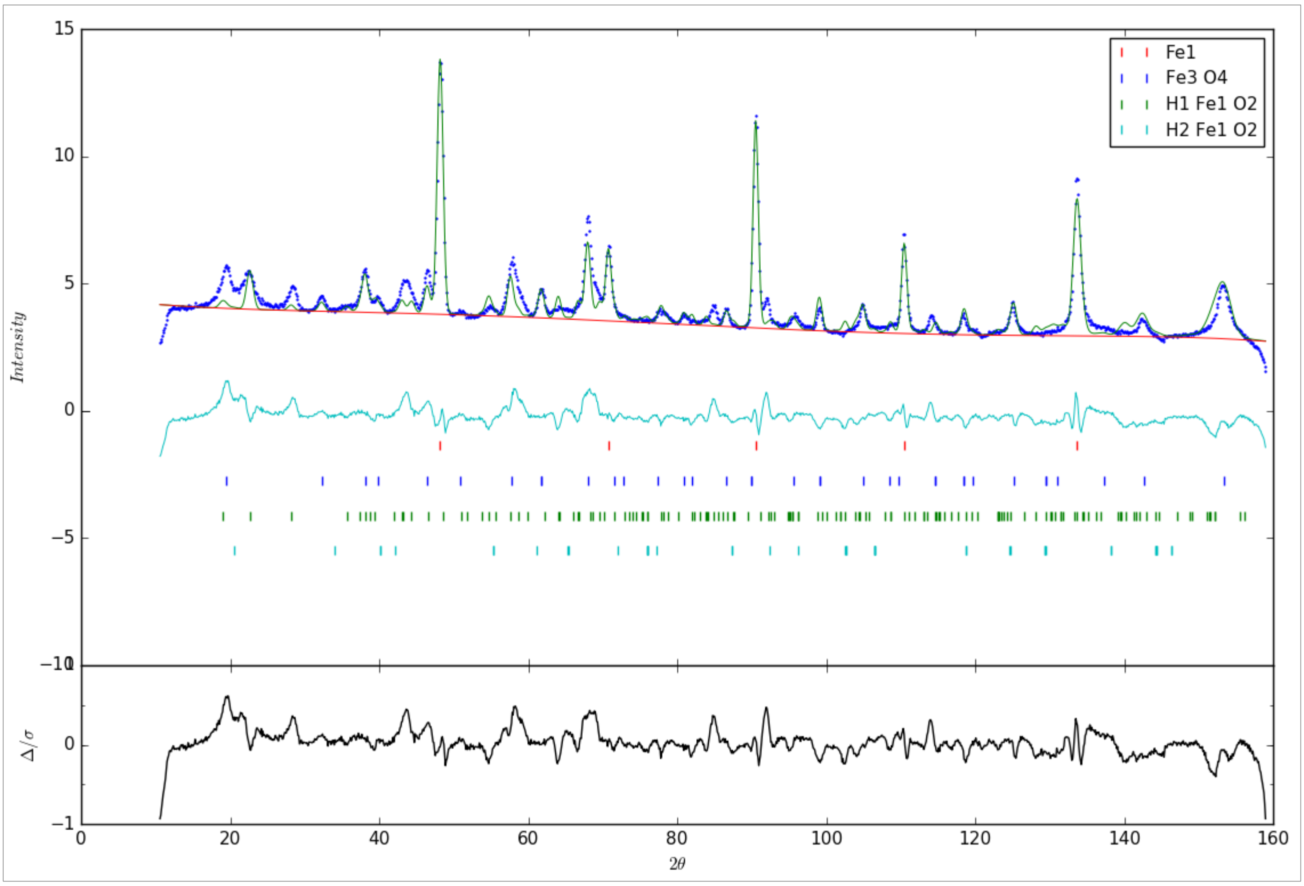

Figure 60. Rietveld refinement on neutron diffraction pattern of Fe 0%

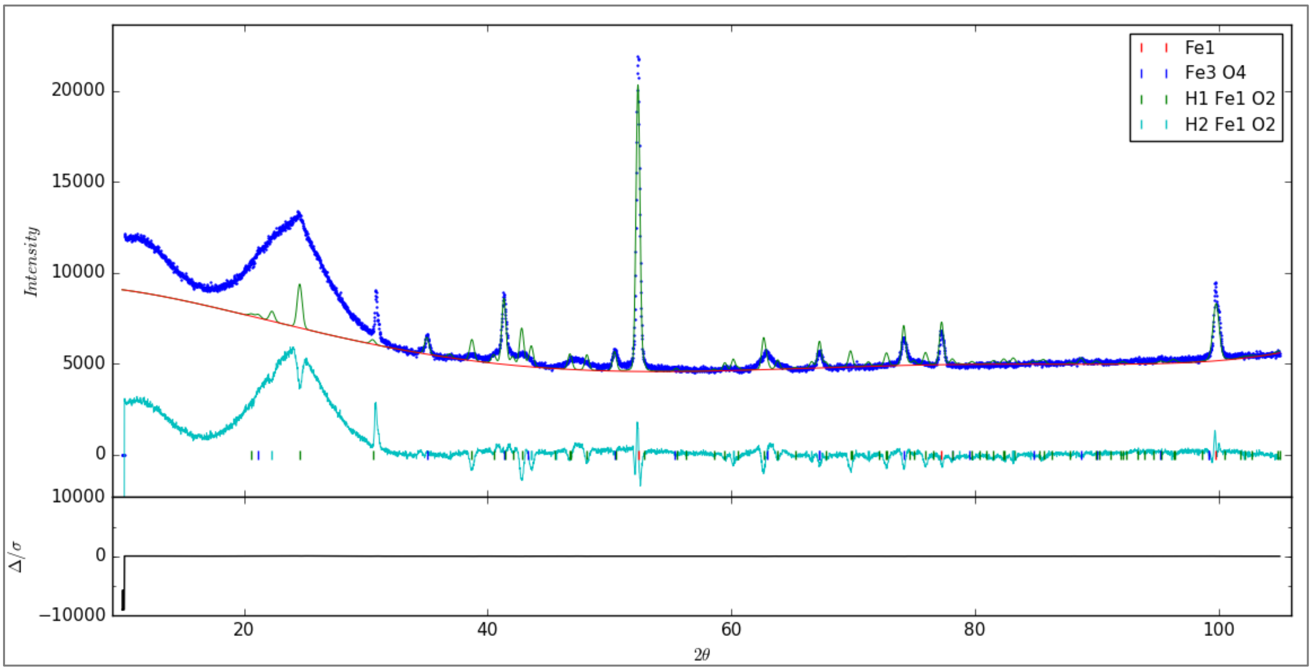

Figure 61. Rietveld refinement on X-ray diffraction pattern of Fe 0%

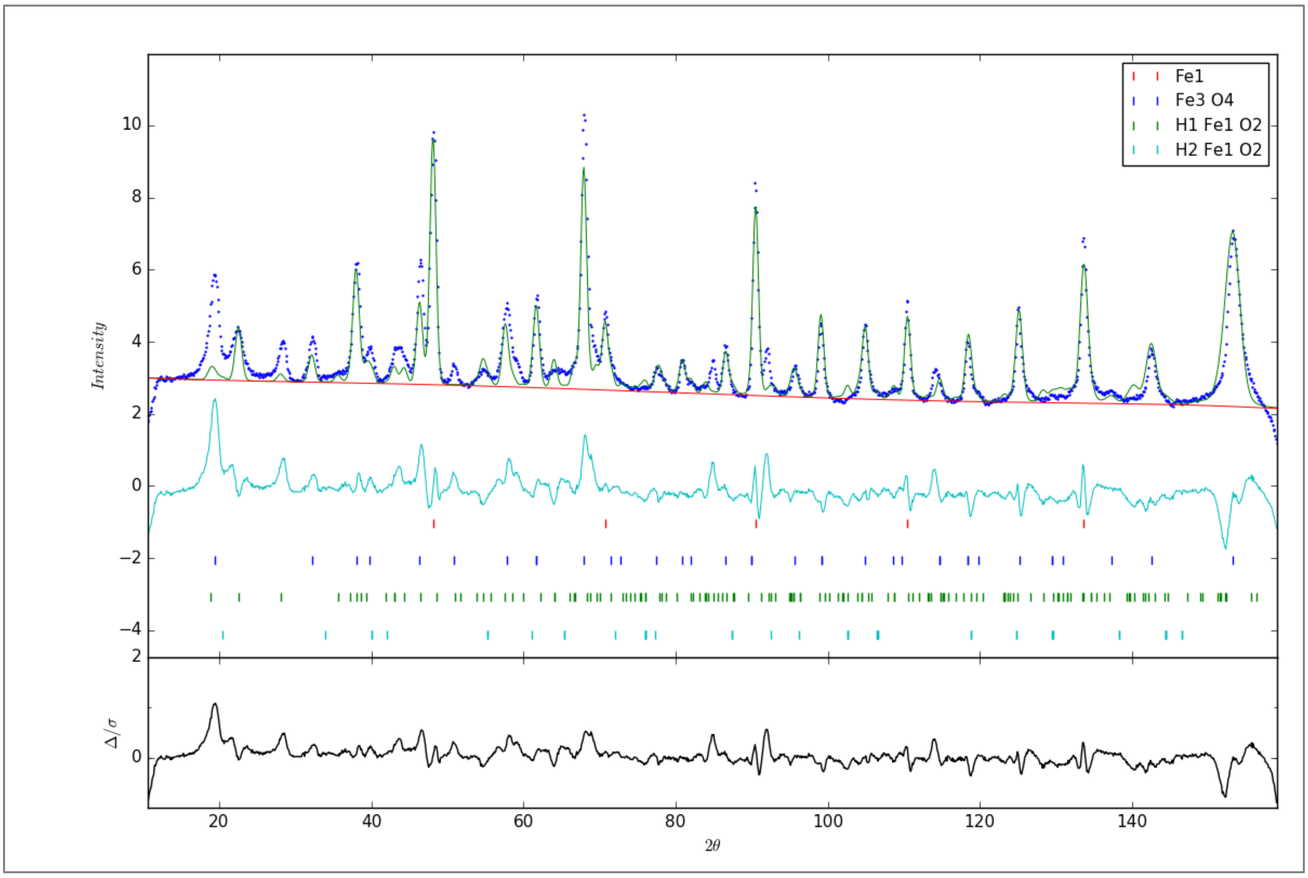

Figure 62. Rietveld refinement on neutron diffraction pattern of Fe 20%

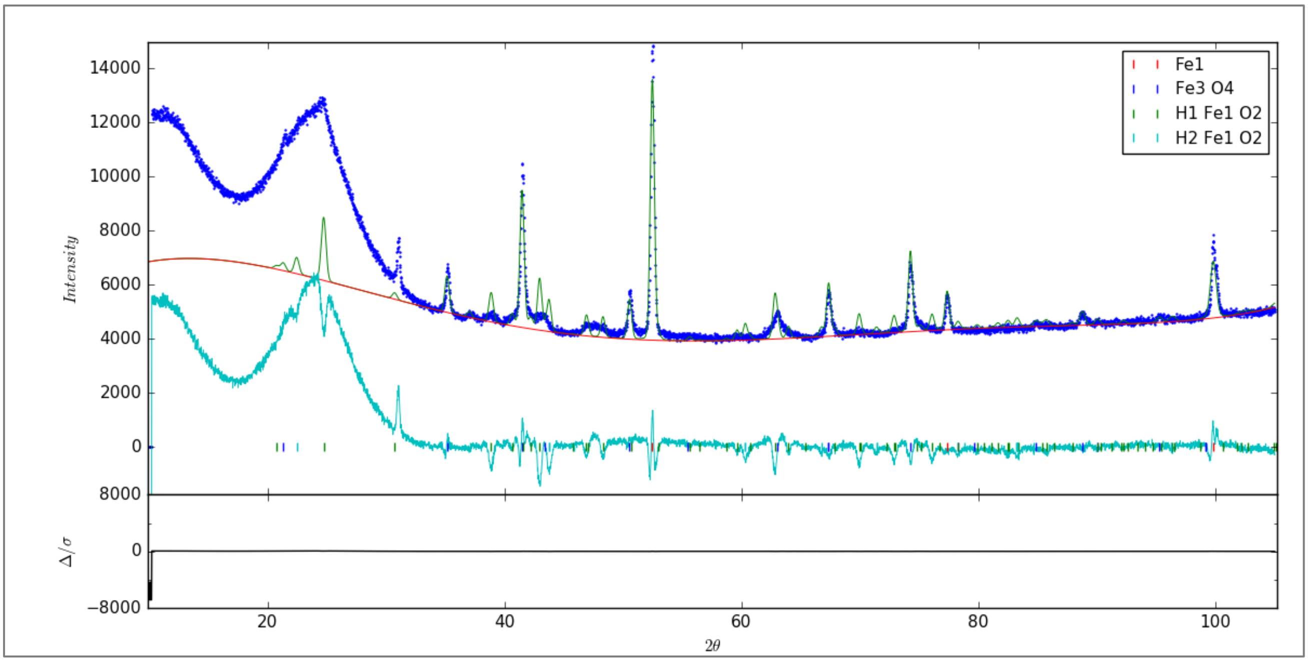

Figure 63. Rietveld refinement on X-ray diffraction pattern of Fe 20%

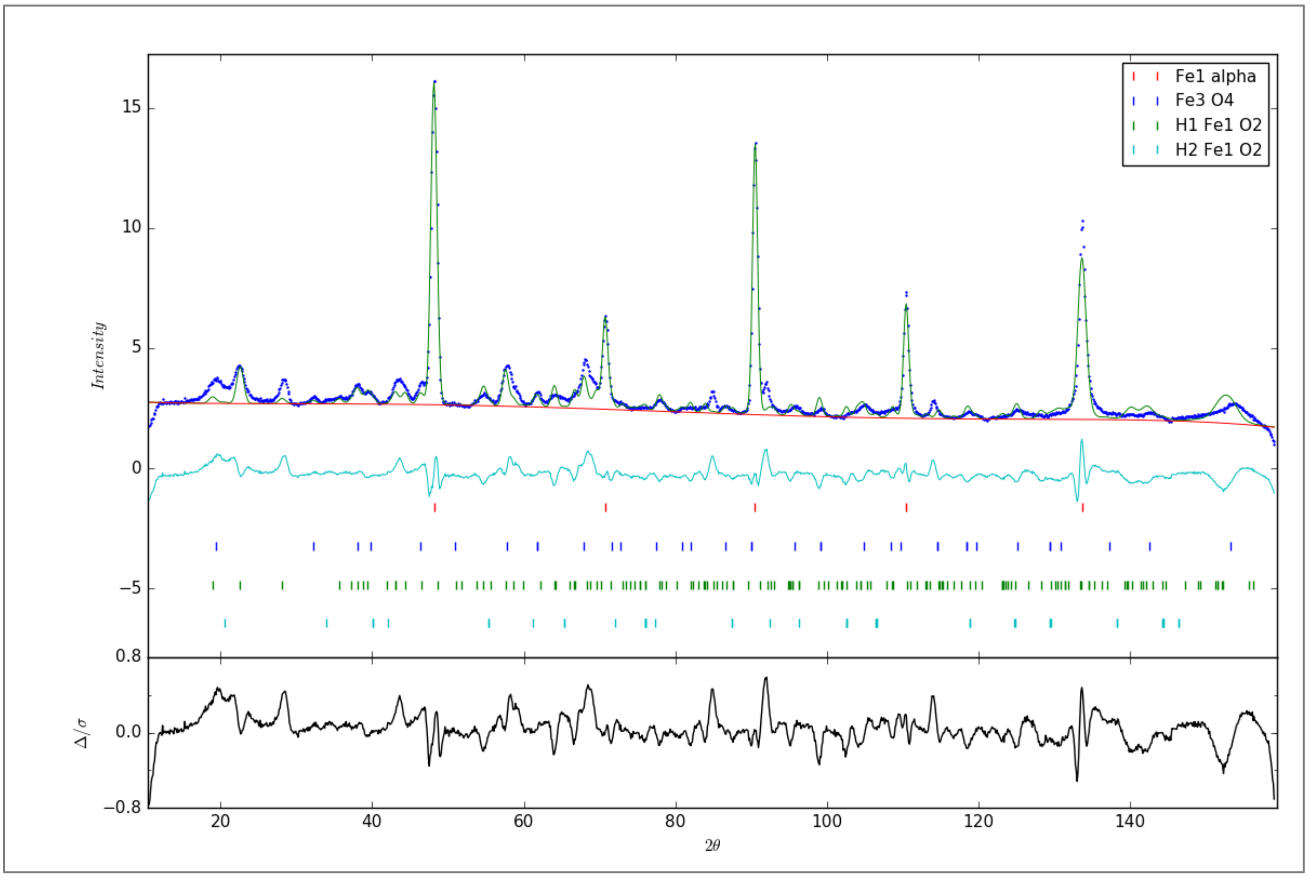

Figure 64. Rietveld refinement on neutron diffraction pattern of Fe 39%

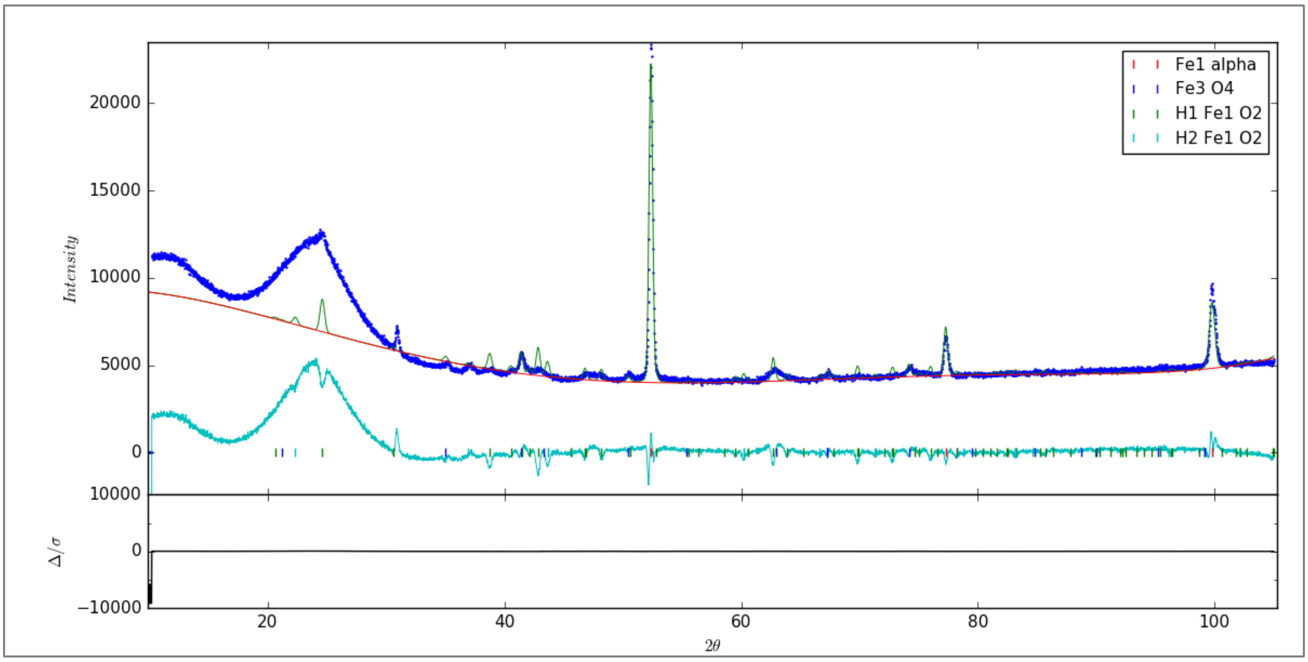

Figure 65. Rietveld refinement on X-ray diffraction pattern of Fe 39%

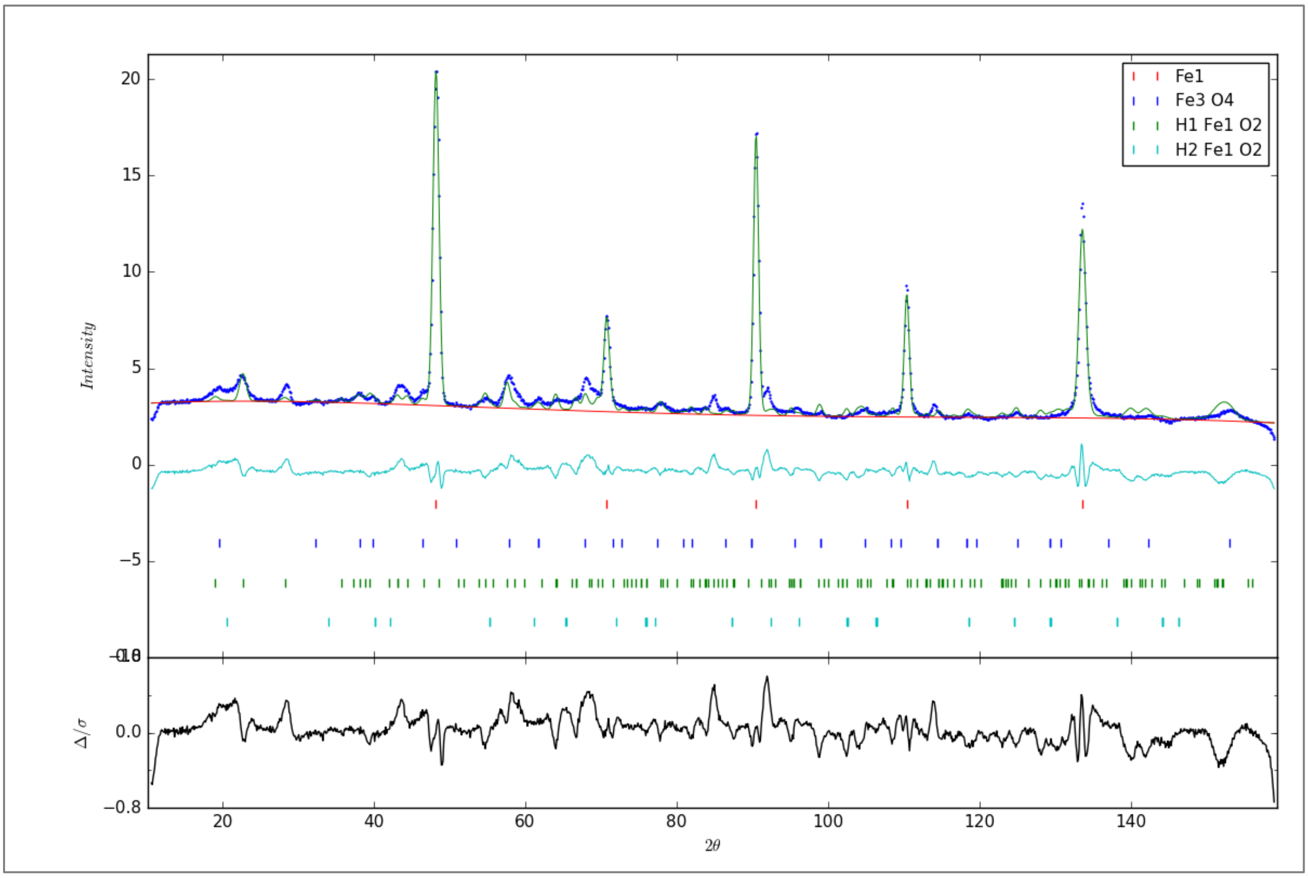

Figure 66. Rietveld refinement on neutron diffraction pattern of Fe 60%

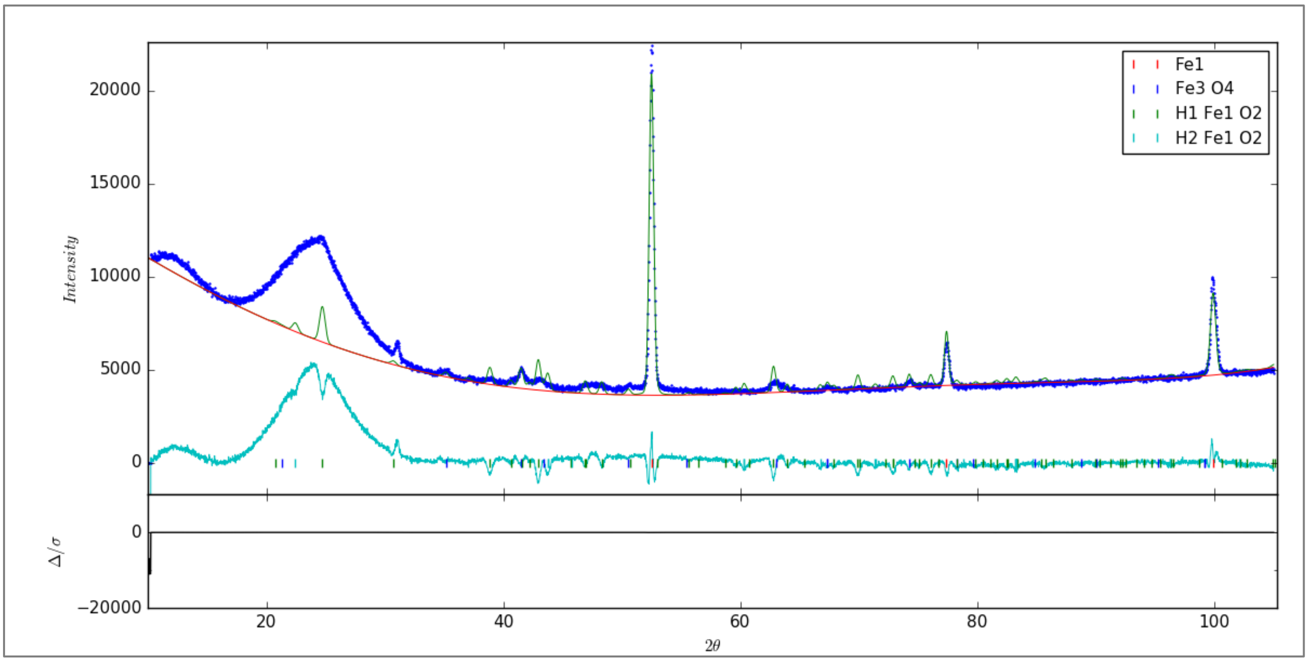

Figure 67. Rietveld refinement on X-ray diffraction pattern of Fe 60%

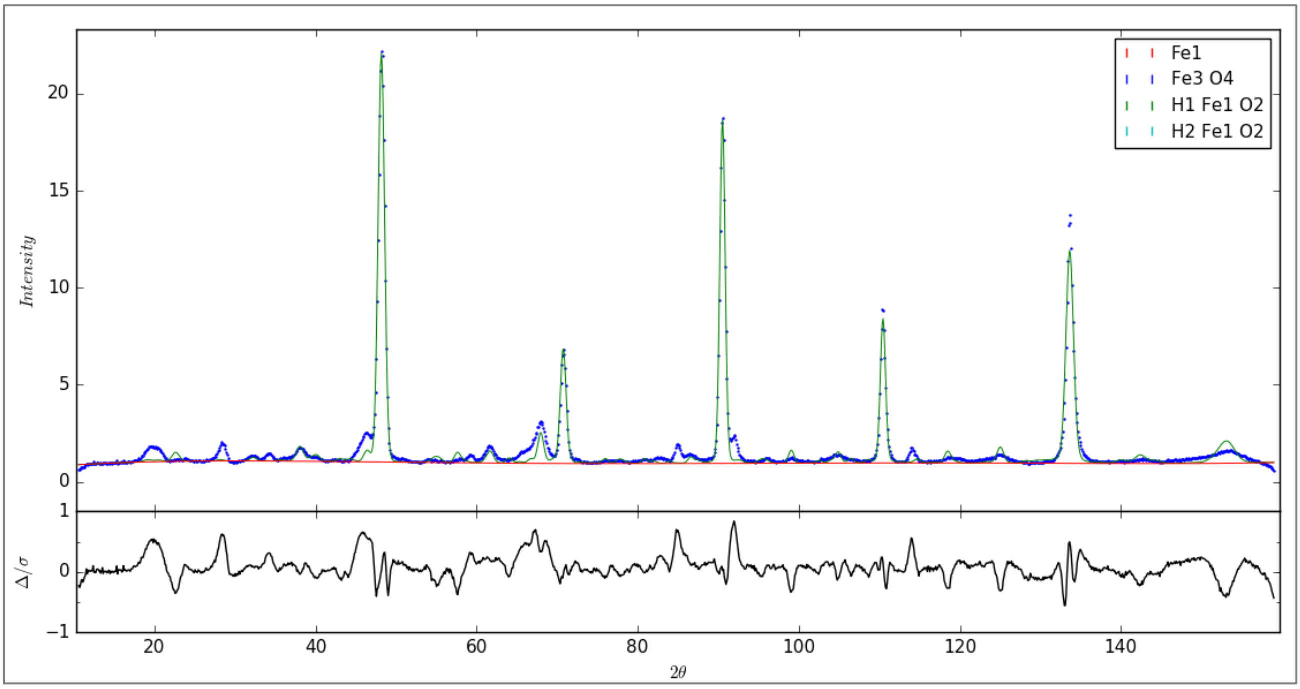

Figure 68. Rietveld refinement on neutron diffraction pattern of Fe 90%

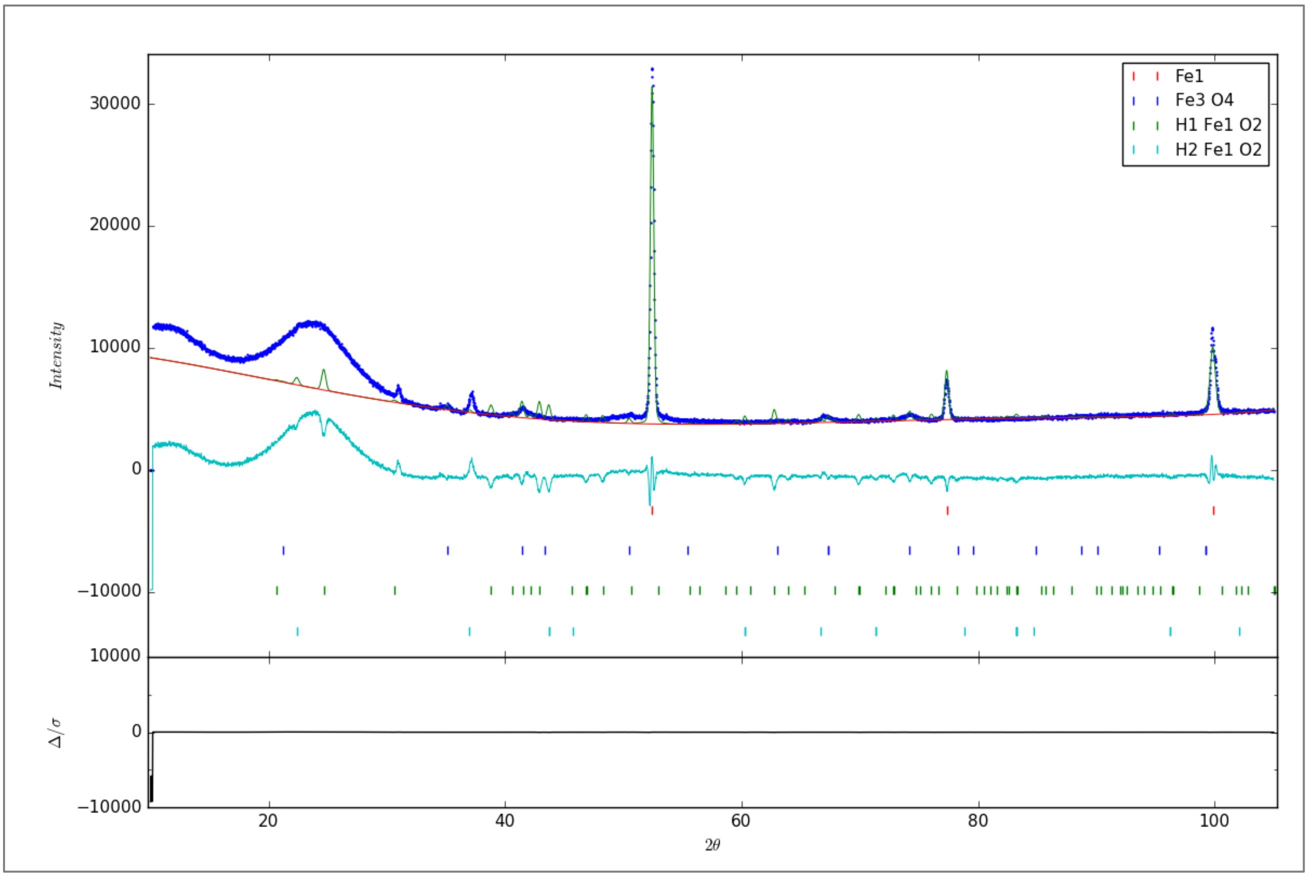

Figure 69. Rietveld refinement on X-ray diffraction pattern of Fe 90%

A3 REFINEMENT PARAMETERS OF NICKEL SAMPLES AT VARIED STATES OF CHARGE

The Rietveld refinement is performed in GSAS II and for every sample the parameters which are refined are displayed below, with the corresponding final result. The same two instrument parameter files are used for all the samples for ND and XRD respectively. Starred parameters are defined in advance. If a value is left out, predefined parameters are used.

NICKEL AT 0% OF SOC

ND

Background
*Background function: chebyschev
*Number of coeff.: 3
Background coefficients: 4.1198 -1.1409 0.0628

Instrument parameters
U = 5311.609
V = -11161.505
W = 7080.532

Sample parameters
Sample X displ. (μm) = 1977.106
Sample Y displ. (μm) = 2833.806

XRD

Background
*Background function: chebyschev
*Number of coeff.: 6
Background coefficients: 442.3845 -301.6567 -174.8176 459.5887 523.8522 -648.8637

Instrument parameters
U = -7971.333
V = -10200.309
W = -952.827

Sample parameters
Sample X displ. (μm) = -290.991
Sample Y displ. (μm) = -571.763

Phases

β-Ni(OH)$_2$
*Space group: P -3 m 1
Unit cell: a = 3.12229, c = 4.62081

	ND	XRD
phase fraction:	3.5791	17.8164
microstrain:	22615.5	22757.8

β-NiOOH
*Space group: P 3 m 1
Unit cell: a = 2.81801, c = 4.74817

	ND	XRD
phase fraction:	0.261	2.7828

microstrain:	*1000.0	8285.5

γ-NiOOH

*Space group: R -3 m
*Unit cell: a = 2.77000, c = 20.83100

	ND	XRD
phase fraction:	0.38	0.3715
*microstrain:	1000.0	1000

C

*Space group: P 63/m m c
Unit cell: a = 2.46182, c = 6.70079

	ND	XRD
phase fraction:	3.5085	38.2119
microstrain:	-12959.5	-96941.0

NICKEL AT 21% OF SOC

ND

Background

*Background function: chebyschev
*Number of coeff.: 6
Background coefficients: 3.4243 -1.3165 0.3871 1.1112 -0.272 -0.8315

Instrument parameters

U = 5523.727
V = -10300.571
W = 6014.849

Sample parameters

Sample X displ. (µm) = 948.406
Sample Y displ. (µm) = 3474.663

XRD

Background

*Background function: chebyschev
*Number of coeff.: 6
Background coefficients: 346.2923 93.2679 -19.388 -648.017 517.2462 -71.5142

Instrument parameters

U = 94351.213
V = -17622.912
W = 2316.424

Sample parameters

Sample X displ. (µm) = 482.275
Sample Y displ. (µm) = -226.724

Phases

β-Ni(OH)$_2$

*Space group: P -3 m 1
*Unit cell: a = 3.12680, c = 4.60600

	ND	XRD
phase fraction:	22.5243	27.1493
*microstrain:	1000.0	1000.0

β-NiOOH

*Space group: P 3 m 1
*Unit cell: a = 2.81000, c = 4.84000

	ND	XRD
phase fraction:	7.2859	-1.0994
microstrain:	*1000.0	-7404532.4

γ-NiOOH

*Space group: R -3 m
*Unit cell: a = 2.77000, c = 20.83100

	ND	XRD
phase fraction:	3.293	1.016
*microstrain:	1000.0	1000.0

C

*Space group: P 63/m m c
*Unit cell: a = 2.45600, c = 6.70020

	ND	XRD
phase fraction:	47.2514	44.656
microstrain:	*1000.0	-42378.8

NICKEL AT 43% OF SOC

ND

Background

*Background function: chebyschev
*Number of coeff.: 6
Background coefficients: 3.1899 -0.9974 0.4493 0.8101 -0.1383 -0.9635

Instrument parameters

U = 4739.709
V = -8542.053
W = 5687.149

Sample parameters

Sample X displ. (µm) = 653.295
Sample Y displ. (µm) = 3467.417

XRD

Background

*Background function: chebyschev
*Number of coeff.: 6

Background coefficients: 513.6503 -188.0419 -615.0876 261.0862 874.475 -645.2496

Instrument parameters

U = -7387.653
V = 5758.937
W = 3003.946

Sample parameters

Sample X displ. (µm) = 183.76
Sample Y displ. (µm) = 77.587

Phases

β-Ni(OH)$_2$

*Space group: P -3 m 1
*Unit cell: a = 3.12680, c = 4.60600

	ND	XRD
phase fraction:	3.0075	6.2259
microstrain:	*1000.0	4103.9

β-NiOOH

*Space group: P 3 m 1
*Unit cell: a = 2.81000, c =4.84000

	ND	XRD
phase fraction:	5.8598	1.1282
microstrain:	164200.2	2984.5

γ-NiOOH

*Space group: R -3 m
*Unit cell: a = 2.77000, c = 20.83100

	ND	XRD
phase fraction:	0.7134	0.9953
*microstrain:	1000.0	1000.0

C

*Space group: P 63/m m c
*Unit cell: a = 2.45600, c = 6.70020

	ND	XRD
phase fraction:	6.9908	19.8228
microstrain:	-4955.4	-40744.0

NICKEL AT 58% OF SOC

ND

Background

*Background function: chebyschev
*Number of coeff.: 6
Background coefficients: 2.8766 -1.2384 0.425 1.6507 -0.2775 -1.22

Instrument parameters
U = 4167.07
V = -8589.245
W = 5320.366

Sample parameters
Sample X displ. (μm) = 860.956
Sample Y displ. (μm) = 3428.094

XRD

Background
*Background function: chebyschev
*Number of coeff.: 6
Background coefficients: 419.5113 -231.3618 -412.85 263.8857 881.0476 -637.2758

Instrument parameters
U = 1155.761
V = -2404.934
W = 392.419

Sample parameters
Sample X displ. (μm) = -846.311
Sample Y displ. (μm) = 326.188

Phases

β-$Ni(OH)_2$
*Space group: P -3 m 1
*Unit cell: a = 3.12680, c = 4.60600

	ND	XRD
phase fraction:	1.236	22.346
microstrain:	11258.1	49633.9

β-NiOOH
*Space group: P 3 m 1
*Unit cell: a = 2.81000, c = 4.84000

	ND	XRD
phase fraction:	6.5939	1.2674
microstrain:	348937.3	-28557.4

γ-NiOOH
*Space group: R -3 m
*Unit cell: a = 2.77000, c = 20.83100

	ND	XRD
phase fraction:	0.6851	0.6042
*microstrain:	1000.0	1000.0

C
*Space group: P 63/m m c
*Unit cell: a = 2.45600, c = 6.70020

	ND	XRD

phase fraction:	5.0903	180.7425
microstrain:	2661.2	9874.3

NICKEL AT 78% OF SOC

ND

Background

*Background function: chebyschev
*Number of coeff.: 6
Background coefficients: 2.5996 -0.5626 -0.0646 0.7026 0.3927 -1.0088

Instrument parameters

U = 6587.223
V = -13188.716
W = 8061.245

Sample parameters

Sample X displ. (μm) = 887.696
Sample Y displ. (μm) = 3733.624

XRD

Background

*Background function: chebyschev
*Number of coeff.: 6
Background coefficients: 480.3816 -137.3902 -475.3036 -16.012 883.8481 -370.4257

Instrument parameters

U = 113968.223
V = -65872.197
W = 9622.597

Sample parameters

Sample X displ. (μm) = -582.293
Sample Y displ. (μm) = 1.287

Phases

β-Ni(OH)$_2$

*Space group: P -3 m 1
*Unit cell: a = 3.12680, c = 4.60600

	ND	XRD
phase fraction:	1.0378	8.508
microstrain:	6009.4	4886.9

β-NiOOH

*Space group: P 3 m 1
*Unit cell: a = 2.81000, c = 4.84000

	ND	XRD
phase fraction:	0.5713	2.944
microstrain:	8724.5	-2930.8

γ-NiOOH

*Space group: R -3 m
Unit cell: a = 3.49585, c = 20.77969

	ND	XRD
phase fraction:	0.583	1.9956
microstrain:	31945.1	-156232.1

C

*Space group: P 63/m m c
*Unit cell: a = 2.45600, c = 6.70020

	ND	XRD
phase fraction:	2.9299	83.0946
microstrain:	1028.3	2079.5

NICKEL AT 102% OF SOC

ND

Background

*Background function: chebyschev
*Number of coeff.: 6
Background coefficients: 2.187 -0.2772 0.1163 0.3873 0.1522 -0.7755

Instrument parameters

U = 5979.692
V = -13188.716
W = 7740.442

Sample parameters

Sample X displ. (μm) = 533.634
Sample Y displ. (μm) = 3608.377

XRD

Background

*Background function: chebyschev
*Number of coeff.: 6
Background coefficients: 480.3816 -137.9787 -461.5238 203.2055 888.244 -647.3035

Instrument parameters

U = 69658.139
V = -40568.362
W = 5915.684

Sample parameters

Sample X displ. (μm) = -1003.878
Sample Y displ. (μm) = 467.532

Phases

β-$Ni(OH)_2$

*Space group: P -3 m 1

*Unit cell: a = 3.12680, c = 4.60600

	ND	XRD
phase fraction:	0.8611	5.5207
*microstrain:	1000.0	1000.0

β-NiOOH

*Space group: P 3 m 1
*Unit cell: a = 2.81000, c = 4.84000

	ND	XRD
phase fraction:	0.5315	2.2761
*microstrain:	1000.0	1000.0

γ-NiOOH

*Space group: R -3 m
*Unit cell: a = 2.77000, c = 20.83100

	ND	XRD
phase fraction:	0.5597	2.0017
*microstrain:	1000.0	1000.0

C

Space group: P 63/m m c
Unit cell: a = 2.45600, c = 6.70020

	ND	XRD
phase fraction:	3.0757	106.322
*microstrain:	1000.0	1000.0

A4 REFINEMENT PARAMETERS OF IRON SAMPLES AT VARIED STATES OF CHARGE

The Rietveld refinement is performed in GSAS II and for every sample the parameters which are refined are displayed below, with the corresponding final result. The same two instrument parameter files are used for all the samples for ND and XRD respectively. Starred parameters are defined in advance. If a value is left out, predefined parameters are used.

IRON AT 0% OF SOC

ND

Background
*Background function: chebyschev
*Number of coeff.: 6
Background coefficients: 3.329 -1.0606 0.2466 1.1512 -0.1264 -0.811

Instrument parameters
U = 875.43
V = -2089.874
W = 2296.97

Sample parameters
Sample X displ. (µm) = 1541.78
Sample Y displ. (µm) = 2202.836

XRD

Background
*Background function: chebyschev
*Number of coeff.: 6
Background coefficients: 4594.8705 533.2673 2978.3859 -5803.2297 -237.5071 3535.8252

Instrument parameters
U = 1022.994
V = -1281.642
W = 613.206

Sample parameters
Sample X displ. (µm) = 890.69
Sample Y displ. (µm) = -219.158

Phases

Fe
*Space group: I m -3 m
Unit cell: a = 2.86586

	ND	XRD
phase fraction:	34.8219	37.2305
*microstrain:	1000.0	1000.0

Fe_3O_4
*Space group: F d -3 m
Unit cell: a = 8.39323

	ND	XRD

phase fraction:	0.9105	1.2494
*microstrain:	1000.0	1000.0

FeOOH

*Space group: P b n m
*Unit cell: a = 4.61450, b = 9.95530, c= 3.01770

	ND	XRD
phase fraction:	5.9328	11.1679
*microstrain:	1000.0	1000.0

$Fe(OH)_2$

*Space group: P -3 m 1
*Unit cell: a = 3.25800, c = 4.60500

	ND	XRD
phase fraction:	1.5737	8.8165
*microstrain:	1000.0	1000.0

IRON AT 20% OF SOC

ND

Background

*Background function: chebyschev
*Number of coeff.: 6
Background coefficients: 2.5488 -0.5812 0.1057 0.4916 -0.084 -0.3349

Instrument parameters

U = 656.132
V = -1492.902
W = 2113.605

Sample parameters

Sample X displ. (µm) = 2279.891
Sample Y displ. (µm) = 2042.633

XRD

Background

*Background function: chebyschev
*Number of coeff.: 6
Background coefficients: 3921.6517 238.9516 3771.4371 -4735.6205 -1687.1849 3650.9167

Instrument parameters

U = 773.743
V = -928.389
W = 544.689

Sample parameters

Sample X displ. (µm) = 222.165
Sample Y displ. (µm) = -1132.271

Phases

Fe

*Space group: I m -3 m
Unit cell: a = 2.86716

	ND	XRD
phase fraction:	13.8799	19.3869
*microstrain:	1000.0	1000.0

Fe_3O_4

*Space group: F d -3 m
*Unit cell: a = 8.39670

	ND	XRD
phase fraction:	1.1127	1.4679
*microstrain:	1000.0	1000.0

FeOOH

*Space group: P b n m
*Unit cell: a = 4.61450, b = 9.95530, c= 3.01770

	ND	XRD
phase fraction:	3.2365	8.4857
*microstrain:	1000.0	1000.0

$Fe(OH)_2$

*Space group: P -3 m 1
*Unit cell: a = 3.25800, c = 4.60500

	ND	XRD
phase fraction:	1.5206	7.4994
*microstrain:	1000.0	1000.0

IRON AT 39% OF SOC

ND

Background

*Background function: chebyschev
*Number of coeff.: 6
Background coefficients: 2.2926 -0.8389 0.3072 1.1673 -0.3727 -0.8476

Instrument parameters

U = 1123.041
V = -2633.843
W = 2524.192

Sample parameters

Sample X displ. (µm) = 1787.357
Sample Y displ. (µm) = 2082.988

XRD

Background

*Background function: chebyschev
*Number of coeff.: 6
Background coefficients: 3999.7775 429.8027 3814.7921 -6541.2827 -522.971 4222.5518

Instrument parameters

U = 920.701
V = 920.701
W = 920.701

Sample parameters

Sample X displ. (μm) = 878.234
Sample Y displ. (μm) = -723.125

Phases

Fe

*Space group: I m -3 m
Unit cell: a = 2.86690

	ND	XRD
phase fraction:	122.1843	253.7005
*microstrain:	1000.0	1000.0

Fe_3O_4

*Space group: Fd – 3 m
*Unit cell: a = 8.39670

	ND	XRD
phase fraction:	1.0112	2.3539
*microstrain:	1000.0	1000.0

FeOOH

*Space group:P b n m
*Unit cell: a = 4.61450, b = 9.95530, c= 3.01770

	ND	XRD
phase fraction:	16.1305	51.2778
*microstrain:	1000.0	1000.0

$Fe(OH)_2$

*Space group: P -3 m 1
*Unit cell: a = 3.25800, c = 4.60500

	ND	XRD
phase fraction:	4.5291	39.7274
*microstrain:	1000.0	1000.0

IRON AT 60% OF SOC

ND

Background

*Background function: chebyschev

*Number of coeff.: 6
Background coefficients: 2.5961 -0.6281 0.8398 0.0066 -0.7571 0.1043

Instrument parameters
U = 800.457
V = -2124.905
W = 2321.138

Sample parameters
Sample X displ. (μm) = 1135.386
Sample Y displ. (μm) = 2628.932

XRD

Background
*Background function: chebyschev
*Number of coeff.: 6
Background coefficients: 3663.8427 724.1895 3083.9007 -5661.9318 1321.927 1994.9243

Instrument parameters
U = 934.937
V = -1411.75
W = 791.686

Sample parameters
Sample X displ. (μm) = 377.286
Sample Y displ. (μm) = -997.021

Phases

Fe
*Space group: I m -3 m
Unit cell: a = 2.86548

	ND	XRD
phase fraction:	128.3016	121.6893
*microstrain:	1000.0	1000.0

Fe_3O_4
*Space group: F d -3 m
*Unit cell: a = 8.39670

	ND	XRD
phase fraction:	0.5429	1.0353
*microstrain:	1000.0	1000.0

FeOOH
*Space group: P b n m
*Unit cell: a = 4.61450, b = 9.95530, c= 3.01770

	ND	XRD
phase fraction:	11.9442	26.4271
*microstrain:	1000.0	1000.0

$Fe(OH)_2$

*Space group: P -3 m 1
*Unit cell: a = 3.25800, c = 4.60500

	ND	XRD
phase fraction:	3.1617	22.3293
*microstrain:	1000.0	1000.0

IRON AT 90% OF SOC

ND

Background

*Background function: chebyschev
*Number of coeff.: 6
Background coefficients: 0.9453 0.0637 0.2776 -0.6086 -0.2812 0.5987

Instrument parameters

U = 876.851
V = -2261.258
W = 2371.16

Sample parameters

Sample X displ. (μm) = 1735.267
Sample Y displ. (μm) = 2124.613

XRD

Background

*Background function: chebyschev
*Number of coeff.: 6
Background coefficients: 3733.3274 204.4703 3750.0174 -5132.451 -443.3246 2775.0219

Instrument parameters

U = 770.615
V = -934.909
W = 463.803

Sample parameters

Sample X displ. (μm) = 612.429
Sample Y displ. (μm) = -1049.462

Phases

Fe

*Space group: I m -3 m
Unit cell: a = 2.86668

	ND	XRD
phase fraction:	86.8089	152.8953
*microstrain:	1000.0	1000.0

Fe_3O_4

*Space group: F d -3 m

*Unit cell: a = 8.39670

	ND	XRD
phase fraction:	0.5555	1.0286
*microstrain:	1000.0	1000.0

FeOOH

*Space group: P b n m
*Unit cell: a = 4.61450, b = 9.95530, c= 3.01770

	ND	XRD
phase fraction:	2.174	17.7553
*microstrain:	1000.0	1000.0

$Fe(OH)_2$

*Space group: P -3 m 1
*Unit cell: a = 3.25800, c = 4.60500

	ND	XRD
phase fraction:	2.9653	21.9332
*microstrain:	1000.0	1000.0